Alma Mater Studiorum · Università di Bologna

Department of Physics and Astronomy
MSc in Astrophysics and Cosmology

First direct measurement of dust temperature in quasars at Cosmic Dawn

MSc Thesis

Candidate:
Michele Costa

Supervisor:
Prof. Francesca Pozzi

Co-supervisor:
Dr. Roberto Decarli

Academic year 2023/2024
Session III

Into this wild Abyss
The womb of Nature, and perhaps her grave
Of neither sea, nor shore, nor air, nor fire,
But all these in their pregnant causes mixed
Confusedly, and which thus must ever fight,
Unless the Almighty Maker them ordain
His dark materials to create more worlds,
Into this wild Abyss the wary Fiend
Stood on the brink of Hell and looked a while,
Pondering his voyage; for no narrow frith
He had to cross.

John Milton — Paradise Lost

To our happy years

Abstract

Quasars at the dawn of cosmic time (redshift $z > 6$, age of the universe < 1 Gyr) are the most active and luminous non-transient sources in the early universe, and are believed to be the progenitors of today's most massive elliptical galaxies. In these systems, large amounts of gas ($M_{H_2} > 10^{10}$ $M_\odot$) fuel the fast growth of the central supermassive black hole (SMBH, with masses $M_{BH} > 10^8$ $M_\odot$) as well as intense bursts of star formation (SF, with star formation rates $SFR > 100$ $M_\odot$/yr). The interplay of these processes is regulated via AGN feedback mechanisms that are able to quench both SF activity and nuclear accretion, setting the black hole-galaxy scaling relations observed in the local universe.
These early quasars provide therefore unique laboratories to investigate the physical properties of the interstellar medium (ISM) under extreme conditions, offering fundamental insights about the coevolution of supermassive black holes and their host galaxies.
The advent of new generation mm/submm telescopes, such as the *Atacama Large Millimeter Array* (ALMA) or the *Northern Extended Millimeter Array* (NOEMA) revolutionized the study of high-z quasar host galaxies. The outstanding capabilities of these instruments have allowed us to exploit multiple ISM tracers to probe the conditions of the different gas phases of the star-forming medium. At the same time, they have broadened our ability to investigate interstellar dust physical properties', such as dust temperature (T_d), dust mass (M_d) and emissivity index (β) via continuum observations of its graybody emission. At $z > 6$, however, these properties remain largely unconstrained due to the still limited data tracing the far infrared spectral range, where dust emits.

In this thesis project, we aim to enlarge the sample of very high-z quasars ($z > 6$) where the host galaxy ISM properties have been characterized. To achieve this, we reduced and analyzed new ALMA ACA Band 8 observations (~ 400 GHz), and combined them with archival and literature data in order to pin down the dust spectral energy distribution (SED) in 11 type 1 radio quiet quasar host galaxies located at redshift between 6 and 7. These observations at $\nu \simeq 400$ GHz are fundamental to give a constraint on dust physical properties (especially on T_d), as they are thought to probe the peak of the graybody emission at these redshifts. Moreover, this allowed for precise estimates of their infrared luminosities (L_{IR}) and of the associated $SFRs$.

This analysis yielded mean values for the dust mass, emissivity index and temperature of $\log(M_d/M_\odot) = 7.9 \pm 0.1$, $\beta = 2.3 \pm 0.2$ and $T_d = 56 \pm 6$ K respectively. We then compared our findings with the specific literature and found a good match with the results obtained by other works that involved similar objects. We also discuss how the widespread assumption of optically thin dust emission has to be handled with care, especially in the case of very compact sources.
Regarding infrared luminosity and star formation rate, the large average values derived in this work ($L_{IR} = 9 \pm 2 \cdot 10^{12}$ $L_\odot$, $SFR = 1340 \pm 292$ $M_\odot$/yr) seem to confirm that quasar host galaxies are systems experiencing a rapid evolution which, coupled to the intense accretion onto the central supermassive black hole, can possibly set the scaling

relation observed in the local universe.

We also exploit the result obtained on T_d to confirm the dust temperature evolution scenario, linking it to the increased star formation efficiency (SFE) that simulations predict for galaxies populating the early universe, due to their higher gas cosmological accretion rate. In this sense, the higher T_d derived in this work may be considered an observational proxy to validate simulations' outputs.

Finally, we tested our observations in order to investigate the potential influence of the AGN on the derived dust properties, finding no evidence of the quasar significantly contributing to dust heating on a galaxy-wide scale.

Contents

Chapter 1

Introduction

1.1 The universe at the dawn of cosmic time

In this section, we provide a brief overview on the physics of the universe at the **Cosmic Dawn**. This term refers to a period in cosmic history that marks the conclusion of the Epoch of Reionization. It is during this phase of cosmic evolution that the first galaxies were shaped, and the large-scale structure of the universe began to emerge. We illustrate here also the key observational techniques used to search for luminous systems at such early epochs.

1.1.1 Chronology of the early universe

The first observable light in the universe is the **Cosmic Microwave Background** (CMB), an almost isotropic radiation that fills the entire sky. It originates from the last scattering surface, the set of points in spacetime where baryons and radiation decoupled: due to the adiabatic expansion of the universe, around $z \simeq 1100$ (when the universe was approximately 380000 years old), it cooled to a temperature of about 3000 K, allowing primordial protons and electrons to recombine and form the first hydrogen atoms. This marked a phase transition in the universe, making it transparent to radiation.

The following period is usually referred to as the **Dark Ages** as, even if light was now able to propagate in space, there were no sources of radiation yet, except for the CMB itself. It was only at $z \simeq 30$ (*Barkana & Loeb, 2001 [4]*) that the first luminous objects began to form, and with their radiation started to reionize most of the neutral hydrogen. This first generation of stars, known as **Pop III** stars, are expected to be exceptionally massive ($10\ \mathrm{M}_\odot < M_* < 1000\ \mathrm{M}_\odot$) due to the inefficient fragmentation of primordial gas clouds, almost metal-free as they form in an environment that has not been chemically enriched yet, and to originate at the centre of small ($\sim 10^6\ \mathrm{M}_\odot$) dark matter (DM) halos (see, e.g., *Gao et al., 2007 [44]*). Given the large masses predicted for these objects, they will evolve quickly, leading to the collapse into the first black holes (BH) within a few million years, potentially seeding the growth of SMBHs and giving rise to the luminous quasars (QSOs) observed in the early universe.

The onset of Pop III stars marked the beginning of the **Epoch of Reionization**, which ended around $z \simeq 6$, and is thought to be also the period during which the first protogalaxies started to emerge (*Bromm & Yoshida, 2011 [11]*). According to the standard Λ

cold dark matter (ΛCDM) cosmology, during this evolutionary stage DM halos undergo hierarchical merging, gradually creating increasingly larger structures and ultimately contributing to the formation of the galaxies we observe today.
In figure 1.1 its reported a sketch of the evolution of the universe from the Big Bang to the present day.

Studying galaxies and quasars at the **Cosmic Dawn** ($z > 6$), when the universe was less than 1 Gyr old, provides a crucial opportunity to test cosmological models and understand how these objects evolved into those observed in the present day universe. In recent years, the advent of next-generation facilities such as the *Atacama Large Millimeter/Submillimeter Array* (ALMA), the *Northern Extended Millimeter Array* (NOEMA), and the *James Webb Space Telescope* (JWST) has revolutionized observations of the high-z universe, enabling the study of these complex objects at epochs previously unfathomable.

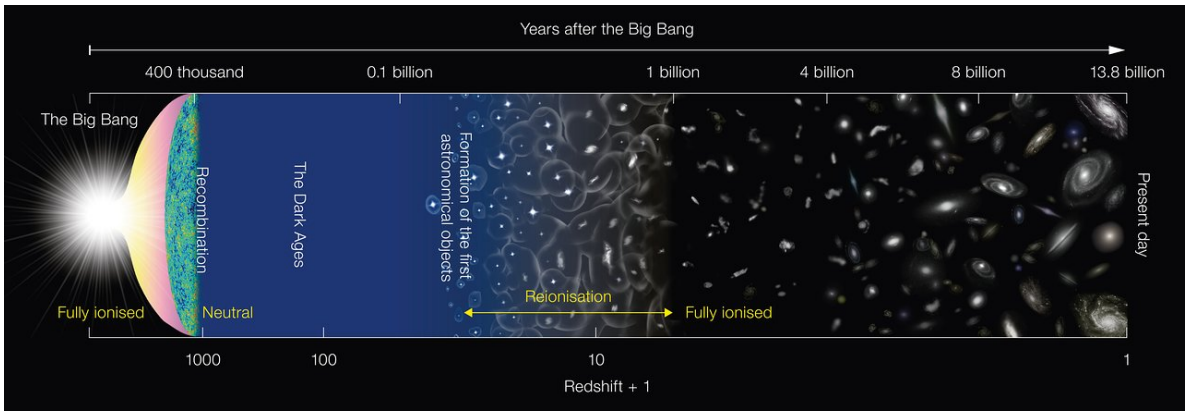

Figure 1.1: *Schematic diagram of the history of the universe, from the Big Bang to the present day, not to scale. Image credits:* NAOJ.

1.1.2 Observing the initial cosmic ages

Nowadays, the quest for quasars and galaxies from these primordial epochs has reached an impressive milestone. To date, the highest redshift quasar detected is $UHZ1$ (*Bogdán et al., 2024 [8]*) at $z = 10.3$, while for galaxies the record is held by *JADES-GS-z14-0* (*Carniani et al., 2024 [14]*), located at $z = 14.3$. These discoveries had been possible only thanks to advanced techniques that, starting from astronomical surveys, are able to identify potential high-z candidates. The most powerful of them is probably the **dropout** technique.
The dropout method exploits the absorption of radiation by neutral intergalactic medium (IGM) clouds situated along the line of sight of distant astronomical sources. It intervenes in two different ways in shaping their observed spectrum:

- via continuum absorption at wavelengths shorter than 912 Å (in the IGM cloud rest-frame).
- via Lyα line absorption at the wavelength of 1216 Å (in the IGM cloud rest-frame).

Cosmological redshift, however, makes so that the farther an IGM cloud is from the source, the longer the wavelength of the emitted radiation that impacts its surface will be. These effects create a discontinuity in the observed flux called **Lyman Break**: all

radiation with $\lambda < 912$ Å will be completely absorbed, while radiation with $1216 > \lambda > 912$ Å will be progressively diminished by the Lyα absorption lines, which emerge at different wavelengths from various IGM clouds located at varying distances from the emitting source.
As a result, the Lyman Break will mark the rest frame wavelength of 1216 Å, and can be exploited to select high-z astronomical sources. In fact, if we tune our observations so that this spectral feature falls between the frequency ranges of two different filters for a specific expected redshift, we can identify sources at that redshift as the ones that are detected in the filter covering the lower frequencies but not in the one covering the higher ones. This is the reason why these sources are also called dropouts, and an example is reported in figure 1.2.
The dropout method enables therefore the selection of high-redshift objects using observations from just two broadband filters.

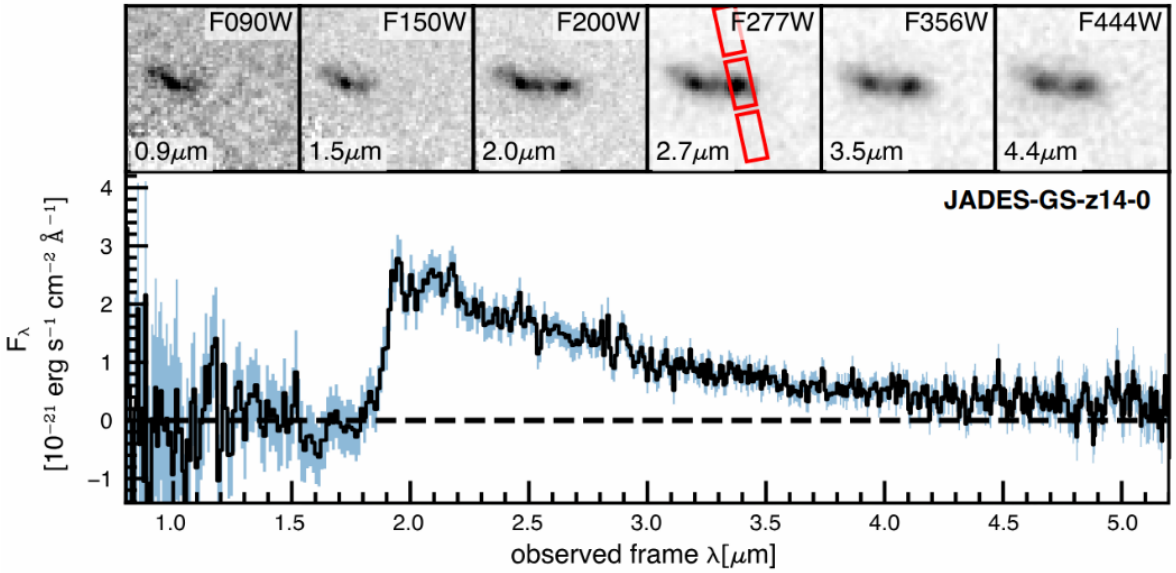

Figure 1.2: *JWST NIRSpec spectrum for JADES-GS-z14-0 and the associated* 1σ *uncertainty (light blue). Inset stamps in the top panels are cutouts of some of the NIRCam JADES survey images. The NIRSpec 3-shutter slitlets are shown in red in each F277W image. Adapted from* Carniani et al., 2024 [14].

The selection of $z > 6$ sources can be affected by numerous contaminants, the most important of which being:

- Brown dwarfs: M, L and T class stars in our galaxy can be mistaken for high-z sources given their point-like appearance and their red color index in the infrared filters.
- Red galaxies at $z \sim 1$: these objects have a very strong rest-frame 4000 Å break, which originates from ultraviolet (UV) radiation blanketing caused by absorption lines from metals in the atmospheres of old, evolved stars. At $z \sim 1$, this break falls in the same wavelength range as the Lyman break does for sources at redshift just above 6, and can thus result in the same dropout effect.

Another widespread technique to identify high-redshift objects is the search for strong **Lyman-α emitters** (LAEs). This method exploits exposures through a narrow-band

filter centered on the redshifted wavelength of the Lyα emission line. Objects at that redshift will therefore stand out as particularly bright in the narrow-band filter.
This technique is particularly effective at identifying sources in the early stages of their evolution (*Hu & McMahon, 1996 [51]*). In more evolved systems, the optical continuum is dominated by aged massive stars, which can enrich their surroundings with metals and dust, leading to absorption features that diminish Lyα emission, making this line weak or undetectable. In contrast, younger systems, having had less time to form and evolve these stars, are fainter in their continuum emission but shine brighter in Lyα due to their less polluted environment and younger stellar populations, which are able to radiatively excite the hydrogen atom. As a result, while these objects may be difficult to detect using the dropout technique, they can be relatively easier to identify through Lyα searches. An example of the spectrum of such sources is provided in figure 1.3.
LAEs can also be associated to QSOs, which may serve as the excitation source for this line emission.

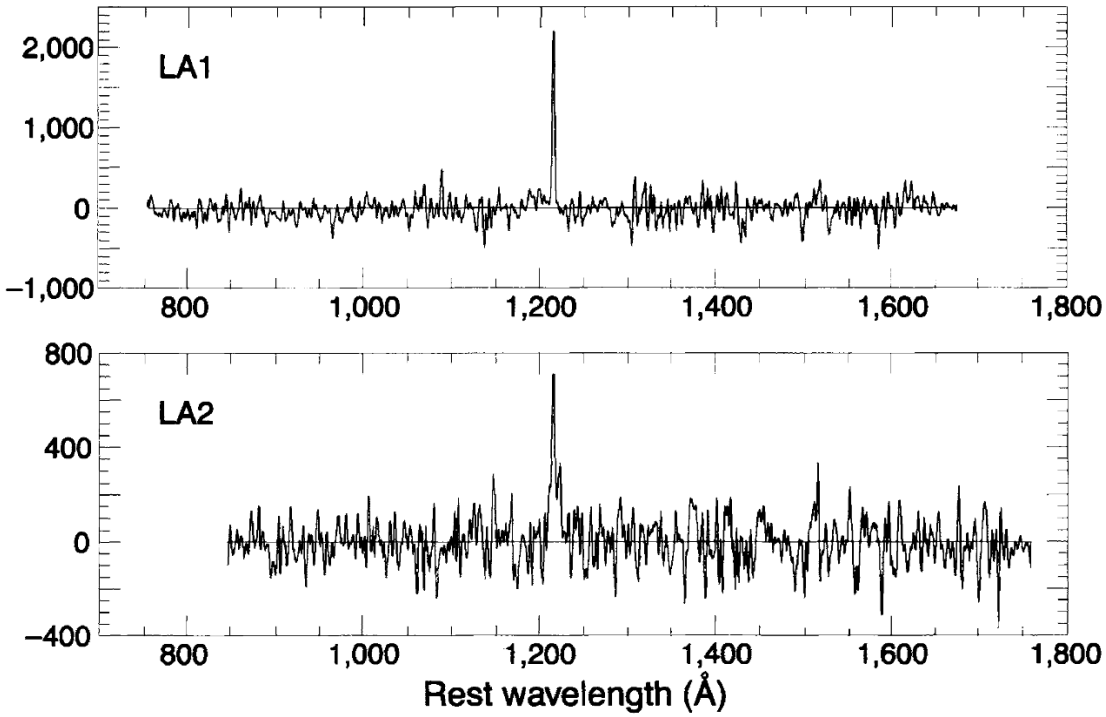

Figure 1.3: *Keck Telescope LRIS spectra for two $z = 4.55$ LAEs plotted in the rest-frame wavelength. From* Hu & McMahon, 1996 [51].

1.2 High-redshift quasars and their host galaxies

In this section we present a brief overview of quasars and their host galaxies, which are the primary focus of this work. We introduce the unified model for active galactic nuclei (AGNs) and discuss the distinctive characteristics of quasars and their relative hosts observed at Cosmic Dawn. Additionally, we explore the main observational methods and tracers used to investigate the physical properties of these objects.

1.2.1 An unified model for AGNs

An **Active Galactic Nucleus** is a powerful phenomenon driven by the accretion of matter onto a supermassive black hole ($M_{BH} > 10^6$ $M_\odot$) located in the central region of a galaxy.
One fundamental quantity that defines a luminous object powered by accretion is the **Eddington Luminosity**:

$$L_{Edd} = \frac{4\pi G c m_p}{\sigma_T} \cdot M_{BH} \tag{1.1}$$

where σ_T is the Thomson cross section, and m_p and M_{BH} the mass of the proton and of the accreting BH respectively. This quantity physically represent the maximum bolometric luminosity that can be substained by a steady process of accretion in spherical symmetry: for luminosities above this limit the radiation pressure will exceed the gravitational force and quench accretion.

The emission from AGNs can span a broad range of the electromagnetic spectrum, from radio waves to γ rays. However, their spectral energy distributions (SEDs) can vary significantly from one object to another, leading to a complex and sometimes redundant taxonomy of AGNs based on their distinct observational characteristics. Historically, the first observed bright ($\mathcal{M}_B < -23$, *Schmidt & Green, 1983 [80]*) AGNs were identified as powerful radio sources with an almost starlike appearance in the optical band (*Schmidt, 1963 [79]*). Because of this reason they were dubbed as quasi-stellar radio sources, or **quasars**.

Nowadays, the main classification of these objects is based on the appearance of their optical spectrum:

- **Type 1** QSOs show allowed transition lines, such as Hα 6563 Å or Hβ 4861 Å, with both a broad (1000-10000 km/s) and narrow (100-1000 km/s) component, as well as forbidden transition lines, such as [NII] 6583 Å and [OIII] 5007 Å, but only with a narrow component. They usually exhibit also a strong continuum emission, especially in the UV part of the spectrum.
- **Type 2** QSOs are instead characterized by the presence of the narrow line component of both allowed and forbidden transitions, but the absence of any broad line component. Their continuum emission is generally weaker in the UV, if compared to Type 1 QSOs

Another important distinction relies on the ratio between the radio flux and the optical flux of these objects R (e.g., $R = S_{6cm}/S_{4400\text{Å}}$):

- **Radio loud** QSOs are identified by large value of this parameter, and are usually defined as having $R > 10$
- **Radio quiet** QSOs show much lower values for this ratio and typically $R < 10$

A complete overview on all AGN classifications is beyond the scope of this work, however it is possible to explain most of the difference in the observed emission of these objects with an **AGN unified model**, where the accretion mode and the viewing angle act as primary interpretative keys.
The accretion mechanism can be either be radiatively efficient (radiative-mode AGNs, *Shakura & Sunyaev, 1973 [82]*) or inefficient (jet-mode AGNs, *Narayan & Yi, 1994 [67]*), with the infall timescale being respectively much longer or shorter than the radiative cooling time.

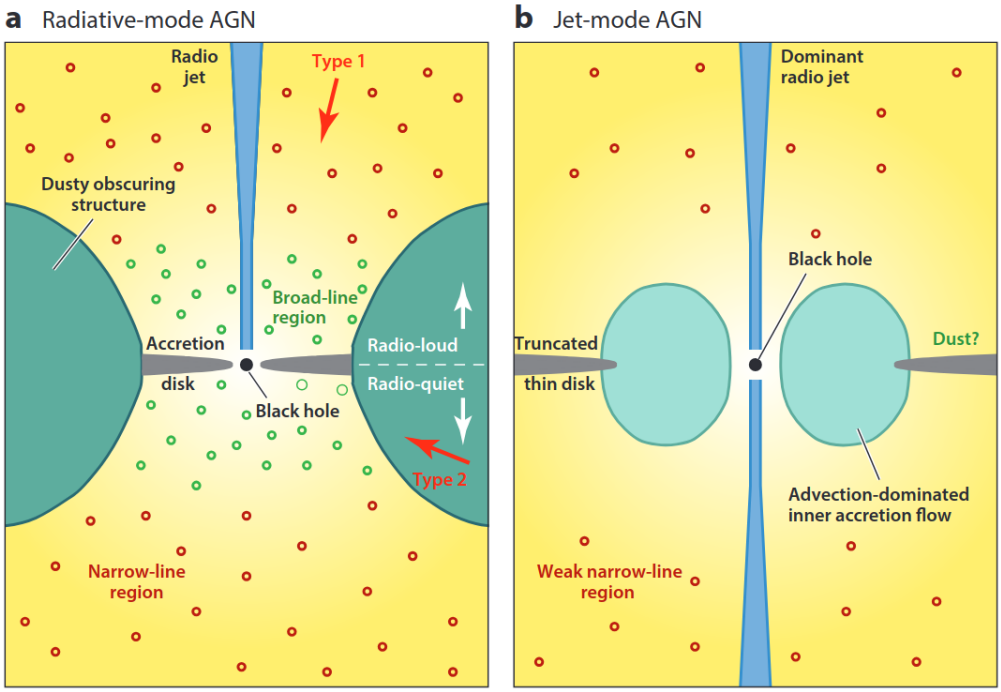

Figure 1.4: *Schematic illustration of an AGN (not to scale).* **Left panel***: a radiative-mode AGN, where a thin disk of material surrounds the SMBH at the core. This accretion disk emits ionizing radiation, which energizes the dense gas clouds in the nearby BLR. A toroidal structure of dust and gas encircles the system, obscuring the inner regions from view in Type 2 AGNs. At greater distances the NLR is exposed to the radiation escaping through the polar directions. In radio loud AGNs, two jets may be launched along the poles.* **Right panel***: a jet-mode AGN, where accretion is linked to a geometrically thick structure, possibly accompanied with a truncated disk. Here, even if the majority of the energy is realised via radio jets, radiative emission from accretion produces a weak NLR region over larger scale. From* Heckman & Best, 2014 [47].

According to this theory, all AGNs feature the following sub-structures, which can differ depending on the accretion mode (see figure 1.4):

- An **Accretion Disk**, which emits as a multi-color blackbody peaking in the optical-UV bands.

In Jet-mode AGNs models predict instead the presence of a geometrically thick structure in the inner region of the AGN, possibly accompanied with a truncated disk.

- A **Hot Corona**, a region of very hot, ionized gas surrounding the inner parts of the accretion disk. This component is responsible of the power-law continuum observed in the X-ray, produced by accretion disk photons up-scattered by the hot electrons ($\sim 10^9$ K) in the corona through Inverse Compton.

- A **Broad Line Region** (BLR), an ensemble of gas clouds with densities between 10^9 and 10^{11} cm^{-3}, and temperature of about 10^4 K. From this region originate the broad allowed transition lines visible in the spectra of type 1 QSOs, while the high densities cause forbidden transitions to be mostly collisionally de-excited. The lines arising from the BLR are broad because of the high rotational velocities (between 10^3 and 10^4 km/s) of the gas clouds set by the proximity to the BH.
  In Jet-mode AGNs, the radiation coming from this region is almost negligible given the much weaker radiation field provided by the accreting system.

- A **Narrow Line Region** (NLR), located farther from the BH, where gas clouds have much lower densities ($\sim 10^4$ cm^{-3}) and velocities (smaller than 10^3 km/s). This is the region where the narrow component of both allowed and forbidden transitions is originated.
  Analogously to the BLR, this region is much weaker in Jet-mode AGNs.

- A **Dusty Torus**, a geometrically thick clumpy structure surrounding the accretion disk and hot corona made of gas and dust. Its emission can be roughly approximated by a superposition of graybody curves (see subsection 2.1.3) peaking in the mid infrared.

In addition to these regions, the AGN may also show **Relativistic Magnetized Jets**, collimated plasma outflows emitting in the radio band via Synchrotron emission.

The AGN unified model explains the differences in the optical spectra and UV continuum observed in type 1 and type 2 QSOs by attributing them to the extinction (see subsection 2.1.1) caused by the dusty torus. In this framework, these two categories are considered intrinsically the same object but viewed from different lines of sight. In type 1 QSOs we observe the AGN almost face-on, which allows us to detect radiation from both the accretion disk and the BLR. In contrast, for type 2 QSOs, the emission from these regions is blocked by the dusty torus, suppressing both the UV continuum and the allowed broad transition lines from the BLR.
The distinction between radio loud and radio quiet QSOs, on the other hand, is linked to the presence (or absence) of relativistic jets. In this classification, jet-mode AGNs are commonly associated with radio loud QSOs, as these jets become the primary mechanism for the source to dissipate energy when radiative processes become inefficient.
In figure 1.5, we present the typical SED of a type 1 QSO and compare it to the SED of a starburst galaxy, highlighting also the difference between radio loud and quiet QSOs.

Recent studies (see, e.g., *Mazzucchelli et al., 2023 [65]*) have revealed that high-redshift AGNs host massive black holes, often with masses exceeding $10^9\,M_\odot$. Their extreme luminosities are driven by significant accretion rates (10-100 $M_\odot$/yr), which fuel the

rapid growth of these black holes in the early universe. Such findings suggest that supermassive black holes formed and evolved quickly, playing a key role in shaping their host galaxies.

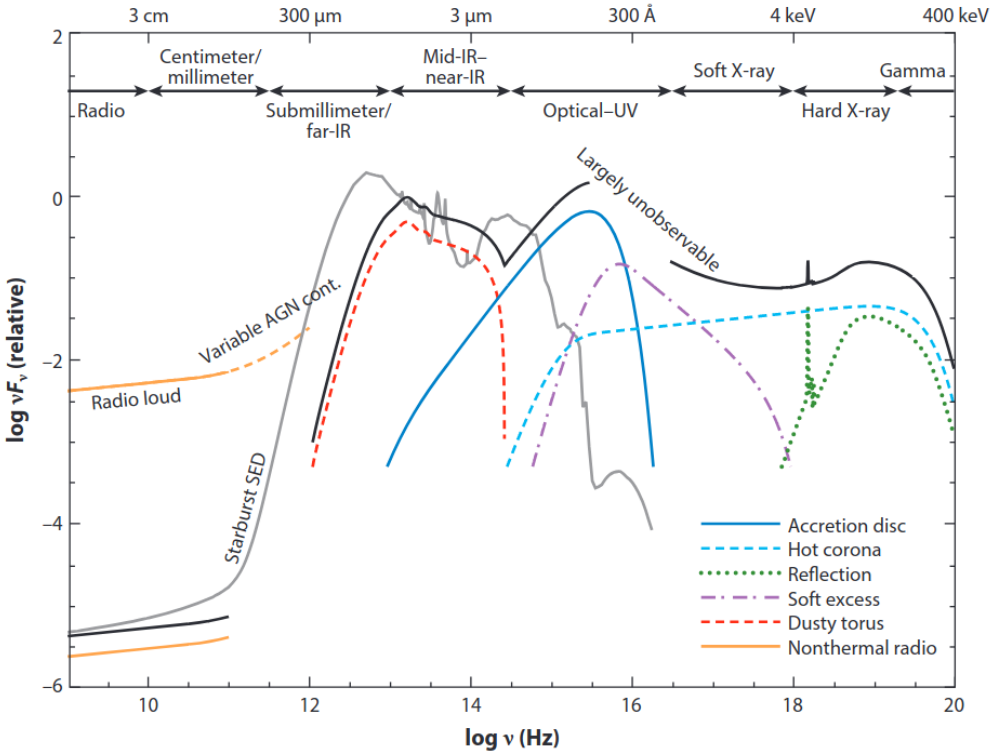

Figure 1.5: *Schematic representation of the SED of an unobscured AGN (black line), separated into the main physical components (colored lines) and compared to the SED of a star-forming galaxy (gray line). The SED of an AGN in the far infrared regime is uncertain; however, it is widely believed to have a minimal contribution (to the overall AGN + host galaxy SED) if compared to star formation. From* Hickox & Alexander, 2018 [48].

1.2.2 Probing AGNs and SMBHs at high-redshift

One of the significant challenges in studying high-redshift QSOs is obtaining accurate information about the properties of their central SMBH. In the Milky Way, we have been able to estimate the mass of the central SMBH by conducting detailed kinematic studies of resolved stellar orbits in its proximity, where the gravitational potential has a dominant influence (see, e.g., *Eckart & Genzel, 1996 [34]*).
In bright QSOs, however, this method is impractical due to the large distances involved, which make it impossible to resolve individual stellar orbits near the SMBH. Furthermore, the stellar emission in the central region is obscured by the intense radiation from the AGN, which dominates the luminosity and masks any contributions from stars. This makes direct kinematic measurements infeasible in these distant objects.

One of the most powerful methods we have to probe SMBH masses in QSOs is the **Reverberation Mapping** (*Blandford & McKee, 1982 [7]*). This method leverages the intrinsic variability in the emission of AGNs to estimate the distance of the BLR from the SMBH. Assuming that BLR clouds are in virial equilibrium with the SMBH's

gravitational potential, this distance can then be used to estimate the SMBH mass. The first step of this technique requires measuring the time lag t_{lag} between variations in the optical continuum of the QSO and corresponding changes in the intensity of the BLR lines (see figure 1.6). Since these lines are excited by the optical-UV emission from the AGN, this delay reflects the light travel time from the black hole to the BLR, allowing us to compute its distance R as:

$$R = c \cdot t_{lag} \tag{1.2}$$

Assuming then that the gas clouds are virialized (i.e. that twice their kinetic energy is equal to the modulus of their potential energy), we can write:

$$M_{BH} = \frac{R \cdot \sigma_v^2}{G} = f\frac{R \cdot FWHM_{line}^2}{G} \tag{1.3}$$

where M_{BH} is the black hole mass, σ_v^2 the virial velocity dispersion, $FWHM_{line}$ the full width half maximum of the observed line, and f a parameter that accounts for the unknown BLR structure, kinematics and viewing angle necessary to link σ_v and $FWHM_{line}$.

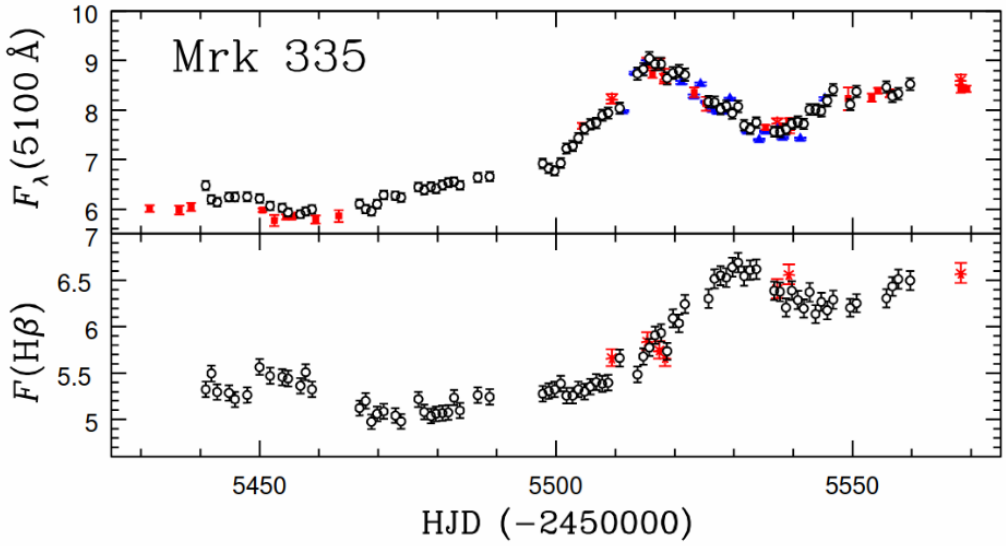

Figure 1.6: *Light curves and time lag for the low luminosity local QSO Mkr 335. The top panel shows the 5100 Å flux in units of 10^{-15} erg s^{-1} cm^{-2} Å^{-1} and the bottom panel shows the integrated Hβ flux in units of 10^{-13} erg s^{-1} cm^{-2}. From* Grier et al., 2012 [45].

This method has been applied to quasar in the local universe, revealing a tight correlation between the continuum power emitted at a given rest-frame reference wavelength λL_λ and the size of the BLR region R obtained via reverberation mapping (see, e.g., *Kaspi et al., 2000 [57]*):

$$R = m \cdot \left(\lambda L_\lambda\right)^n \tag{1.4}$$

where m and n are fitting parameters.
Despite being one of the most reliable techniques to measure BH masses, reverberation mapping is extremely time consuming due to the need for long term monitoring of the

source. Moreover, at high-redshift, this method becomes almost infeasible because of cosmological time dilation and the low variability exhibited by these QSOs.

From reverberation mapping we can however derive scaling relations that can allow us to infer BH masses exploiting **Single Epoch** observations (*Dibai, 1977 [28]*).
This method leverages on the proportionality expressed by equation 1.4 to use the power emitted by the AGN at a given frequency as a proxy of the size of the BLR. Combining equations 1.3 and 1.4, we get an expression for the BH mass that takes the form:

$$\log\left(M_{BH}\right) = a + b \cdot \log\left(\lambda L_{\lambda}\right) + c \cdot \log\left(FWHM_{line}\right) \tag{1.5}$$

where a, b, and c are again fitting parameters determined in the calibration of the relation. Many lines of the BLR can be used as estimators of the mass with this method, the most popular of which being the Hβ line at 4861 Å and, for high-z QSO, the MgII line at 2800 Å.
This technique is however strongly dependant on reverberation mapping calibrations, so the high luminosity regime occupied by QSOs observed at high-z remains poorly sampled.

Finally, another way to estimate the mass of these objects is through the assumption of a given **Eddington ratio** $\gamma = L_{bol}/L_{Edd}$, where L_{bol} is the bolometric AGN luminosity and is derived from continuum observations at a given frequency and the assumption of a bolometric correction (see, e.g., *Runnoe et al., 2012 [77]*). Values of $\gamma \simeq 1$ are consistent with the nature of high-redshift QSOs, as they radiate close to their Eddington limit (*De Rosa et al., 2014 [20]*, *Mazzucchelli et al., 2017 [64]*). M_{BH} estimates obtained with such assumption, however, may be lower limits to the actual BH mass.

Another key quantity that characterizes an AGN is the **mass accretion rate** onto the SMBH. It can be computed directly from the bolometric luminosity (which for instance is derived from observations in the optical continuum or in the X-ray regime). The bolometric luminosity is related to the accretion rate $\dot{M}$ by the equation:

$$\dot{M} = \frac{L_{\mathrm{bol}}}{\eta c^2} \tag{1.6}$$

where η is the radiative efficiency, typically ranging from 0.1 to 0.3 for standard thin accretion disks. This parameter quantifies the efficiency of the accretion process in turning the material that is captured in the accretion disk in to radiation. Given the bolometric luminosity of the AGN and assuming a value for η, this formula allows to estimate the rate at which mass is accreting onto the black hole. Higher luminosities or lower radiative efficiencies result in higher mass accretion rates.

1.2.3 Quasars host galaxies

The study of (type 1) QSO host galaxies in the optical band can be extremely challenging due to the intense emission from the central AGN, which often outshines the stellar continuum of the host galaxy (see figure 1.7). As a result, obtaining measurements of key stellar population-related properties, such as stellar mass or age, becomes difficult unless we achieve the high angular resolutions necessary to separate the host galaxy's emission from the AGN contribution.

At high-redshift, this task remains tough even with the *Hubble Space Telescope* (HST), which has been highly effective for studies at $z < 2$, due to the small angular sizes of distant objects and the effects of cosmological redshift (see, e.g., *Thomas et al., 2023 [92]*). The *James Webb Space Telescope* (JWST) opens up a new opportunity to extend the study of quasar hosts at high-z. The infrared coverage at $\lambda > 2$ μm provides the ability to probe the stellar continuum beyond redshift ~ 3.5, and its unprecedented sensitivity and resolution are key to separate the unresolved quasar component from the extended emission of the host galaxy (see, e.g., *Ding et al., 2022 [29]*).

Figure 1.7: *HST WFPC2 image of a bright $z \simeq 1.5$ QSO (in the centre). The emission from the AGN completely overwhelms the host galaxy's, giving to the object a star-like appearance. The other bright source in the field is a nearby star, while other local galaxies are also visible. Image credits:* Charles Steidel (Caltech) and NASA/ESA.

For even larger cosmological distances, instead, the best method to investigate QSO host galaxies today is through observations in the **submillimeter and millimeter wavelengths**, particularly using facilities like the *Atacama Large Millimeter/submillimeter Array* (ALMA) or the *Northern Extended Millimeter Array* (NOEMA). These observations probe the gas line emission and cool dust continuum in the rest-frame far infrared band, where the contribution of the AGN is not dominant (see figure 1.5), and can even result in spatially resolved emission maps of the host galaxy.

For this reason, these objects are predominantly studied in their **interstellar medium** (ISM) component. While the ISM typically makes up only a small fraction of the galaxy's total mass ($\sim 1\%$ in the local universe), it plays a crucial role in fueling AGN accretion and star formation processes. It is composed of different phases coexisting in the galactic environment:

- The **Hot Ionized Medium** (HIM) is a diffuse phase characterized by high temperatures ($T \simeq 10^6$ K) and low densities ($n \simeq 5 \cdot 10^{-3}$ cm^{-3}). It is primarily produced through shock heating from supernovae explosions (SNe) and predominantly cools via bremsstrahlung emission in the X-ray or synchrotron radiation in the radio band.

- **HII regions** are characterized by high densities (from 5 to 10 cm^{-3}) and temperatures of the order of $T \simeq 8000$ K. They form around massive, young O and B type stars, whose intense UV radiation photoionizes the surrounding gas. As we move further from the star, we encounter the transition from the ionized to the neutral medium, marking the start of the photodissociation region (PDR). In this zone hydrogen atoms are predominantly neutral, as photons with energies above the Lyman limit are absorbed within the HII regions. HII regions emit via bremsstrahlung in the radio band and also show graybody emission in the far infrared, driven by the presence of interstellar dust (see next chapter). As for line emission, they mainly feature Hα and Hβ lines from recombined hydrogen. In Photodissociation Regions (PDRs), key emissions come from atomic lines like [CII] 158 μm, [CI] 985 μm or [OI] 63 μm, with also contribution from molecular CO rotational transition lines arising from the outermost parts.

- The **Warm Ionized Medium** (WIM) is another pervasive phase of the ISM. Compared to the HIM, the WIM has higher densities (ranging from 0.1 to 0.5 cm^{-3}) and lower temperatures ($T \simeq 8000$ K). Its origin is often associated with UV radiation that escapes HII regions, or B type stars that lack the power to create such regions. Other possible sources include X-ray binaries or the extragalactic UV background. The WIM primarily cools via UV and optical allowed line emission, such as Hα and Hβ, as well as bremsstrahlung radiation in the radio band. Given the low density environments, high-excitation forbidden lines may also be observed.

- The **neutral medium** can be classified into two components: the **Warm Neutral Medium** (WNM), characterized by a temperature of $T \simeq 8000$ K and a density n ranging from 0.1 to 0.5 cm^{-3}, and the **Cold Neutral Medium** (CNM), with a temperature of $T \simeq 100$ K and a density n between 10 and 100 cm^{-3}. Theoretically, the high sensitivity of heating and cooling processes in the ISM to ambient temperature suggests that gas in the intermediate temperature range should rapidly transition into one of these two stable phases. However, recent sensitive observations of the ISM in our galaxy indicate that a significant amount of gas may reside in this intermediate, theoretically unstable phase (see *Begum et al., 2010 [5]*). The primary tracer for the neutral medium is the [HI] 21 cm line, which can be detected despite the long timescale of $\sim 10^7$ years of the associated transition, due to the high abundance of neutral hydrogen in the ISM.

- The **Giant Molecular Clouds** (GMCs) represent the coldest and densest phase of the ISM, with densities reaching up to 10^5 cm^{-3} and temperatures as low as 10 K. These objects are gravitationally bound and, owing to their physical properties, serve as ideal sites for star formation. Consequently, they often enshroud HII and PDR regions. The primary constituent is the H_2 molecule. However, due to its homonuclear nature which precludes dipole transitions, the excitation

temperature of its first (quadrupole) allowed transition is very close to its photodissociation temperature. This characteristic makes it particularly challenging to observe. For this reason GMCs are typically traced by molecular emission lines such as CO 2600 μm or HCN 3000 μm. Being these regions associated to SF processes, dust graybody continuum emission is also observable, peaking around 100 μm.

In the last few years, the ISM has proven to be a fundamental probe of high-z QSO host galaxies properties, especially via dust continuum and [CII] 158 μm line emission observations (see, e.g., *Decarli et al., 2018 [25]* or *Venemans et al., 2017 [95]*). Its study has revealed that these objects are characterized by high infrared luminosities (L_{IR}) and star formation rates (SFR), with values of $10^{12} - 10^{13}$ $L_\odot$ and $100 - 1000$ $M_\odot$/yr respectively. These extreme figures are probably justified by the large amount of gaseous reservoir that are able to power SF processes.

1.2.4 Investigating QSO host galaxies at early epochs

As anticipated, the study of the ISM in QSO host galaxies often relies on the observation of key emission lines that provide insights of its physical conditions. In particular, for both local galaxies and QSOs, **CO rotational transitions**, especially the CO(J=1 $\rightarrow$ J=0) 2600 μm line, have proven to be reliable tracers for estimating the molecular gas content of the ISM. This is because CO is closely associated with GMCs, which are predominantly composed of molecular hydrogen.
To estimate the H_2 mass M_{H_2} from the observed CO line luminosity $L'_{\rm CO}$, the relationship depends on a conversion factor, $\alpha_{\rm CO}$, as follows (see *Bolatto et al., 2013 [9]* for a review):

$$M_{H_2} = \alpha_{\rm CO}\, L'_{\rm CO}. \tag{1.7}$$

where $L'_{\rm CO}$ is the luminosity of the CO line and the apex reminds that in this case it is usually expressed in K·pc^2·km/s . The conversion factor $\alpha_{\rm CO}$ varies depending on the CO transition taken into consideration and on the galaxy's environmental properties, thus requires careful calibration across different types of galaxies.
The CO molecule line emission can also be used to probe the properties of the radiation field that excites the ISM. The CO **spectral line energy distribution** (SLED) has been extensively used to study how the environment affects the ratio between the observed line luminosities: a more intense and harder radiation field can excite higher energy levels of the CO molecule, and thus, a CO SLED skewed towards high-energy transitions serves as a proxy for intense SF processes or even the presence of an AGN. At large cosmological distances, low-energy CO transitions are redshifted into the radio band, making their study more challenging due to their low intrinsic luminosity (especially in QSO host galaxies, where the CO SLED is dominated by higher-energy CO transitions). For instance, the highest redshift detection to date ($z \simeq 6.9$) of the CO(2-1) 1300 μm line in a QSO host galaxy was obtained in *Kaasinen et al., 2024 [56]* using the *Jansky Very Large Array* (JVLA) radio interferometer, with a total time on the source of $\sim$ 15 h. For this reason, the molecular gas content of distant objects is often studied through high-energy CO line observations, as these transitions appear intrinsically brighter in these sources compared to the lower-energy ones.

At high-redshift, however, the most used tool to investigate ISM properties is the **[CII] $^2P_{3/2} \rightarrow {}^2P_{1/2}$ 158 μm fine structure line**. As one of the brightest far infrared cooling lines, it traces the gas in photodissociation regions and partially ionized atomic gas, making it a reliable proxy for star formation activity. At high-redshifts ($z > 6$), the [CII] line is redshifted into the submillimeter and millimeter bands, allowing observations with facilities like ALMA.
In order to exploit it to compute SFR, empirical relationships between [CII] luminosity and SFR have been calibrated via observation of low-redshift galaxies, enabling an estimate of the star formation activity in QSO host galaxies at high-z. They appear in the form:

$$\log SFR = a + b \cdot \log L_{[CII]} \tag{1.8}$$

where a and b are calibration parameters, SFR is the star formation rate and $L_{[CII]}$ the [CII] line luminosity (see, e.g., *De Looze et al., 2014 [19]*).
The [CII] line is often used also to trace the velocity structure of the gas, in order to estimate the dynamical mass of QSO host galaxies (see figure 1.8). The basic idea behind this approach exploits the assumption that the gas is at the virial equilibrium (the same assumption of equation 1.3), thus the mass $M_{\rm dyn}(R)$ enclosed inside a radius R can be approximated through the following formula:

$$M_{\rm dyn}(R) = f\frac{R \cdot FWHM^2_{[CII]}}{G} \tag{1.9}$$

where $FWHM_{[CII]}$ is the full width half maximum of the [CII] line, and f is again a parameter that accounts for unknown geometry, kinematics and viewing angle of the system. This method allows estimates of the total mass, including contributions from stars, gas, and the central supermassive black hole (see, e.g., *Neelman et al., 2021 [68]*). This kind of study requires however exceptional spatial resolution, which at the moment can be achieved only by pushing the capabilities of ALMA to their limit, to resolutions of the order of 0.1 arcsec.

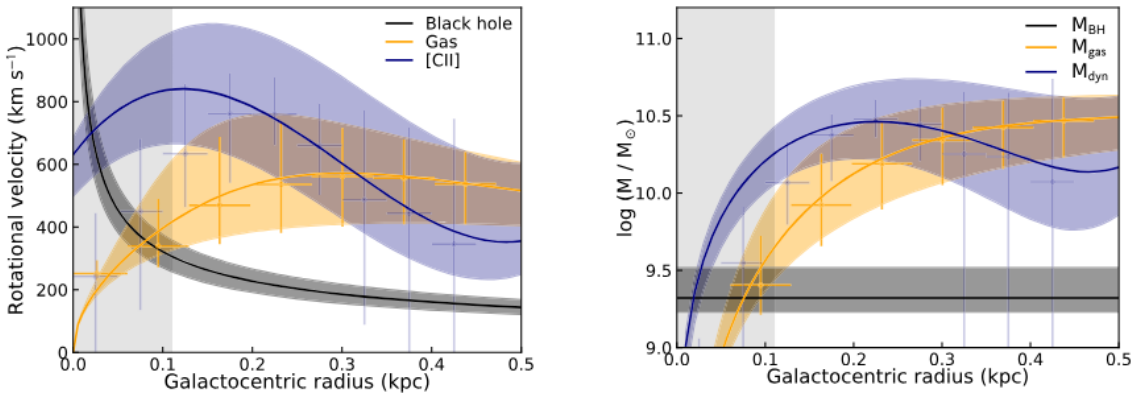

Figure 1.8: ***Left panel:*** *rotation curve of the $z \simeq 6.9$ QSO J2348–3054. The measurements in violet show the rotation curve as derived from the velocity field of the [CII] line, while orange measurement is the velocity contribution from the molecular gas (obtained from the dust mass and the assumption of a gas-to-dust mass ratio). The black measurment show the Keplerian curve set by the central SMBH. Finally, the gray shaded area represents the beamsize of the observations.* ***Right panel:*** *the mass contributions of the different components as a function of galactocentric radius. We remind that the orange line traces the total dynamical mass. From Walter et al. 2022 [98].*

One last probe of the ISM in these objects is the **dust continuum emission**, whose restframe graybody curve peaks in the far infrared band. This emission is used to estimate the total dust mass, temperature, and other physical properties by fitting the observed dust SED with models. Since dust is closely associated with molecular gas, as explained in the previous section, it can serve as a tracer of the molecular content through the gas-to-dust mass ratio, as well as the SF activity. For a more detailed discussion on this topic, we refer to the next chapter.

1.3 The black hole - galaxy coevolution

As previously mentioned, numerous studies have been finding evidence of SMBH exceeding 10^8 $M_\odot$ in quasars populating the universe at ages lower than 1 Gyr. These findings are not fully explained by cosmological models yet, which fail to justify the presence of these massive objects at such high-redshift. In order to experience this rapid growth, Pop III stars remnants (10-100 $M_\odot$) must have been accreting matter at Eddington rates close or ever larger than unity for their whole lifespan (*Lupi et al., 2016 [62]*), as shown in figure 1.9.
Alternative explanations for these observational detections involve the presence of more massive BH seeds generate either via massive star collapse in very dense environments, or by direct collapse of DM halos, as well as lower values of the radiative efficiency η. Nevertheless, the timescale of the growth of these peculiar objects is still an open problem.

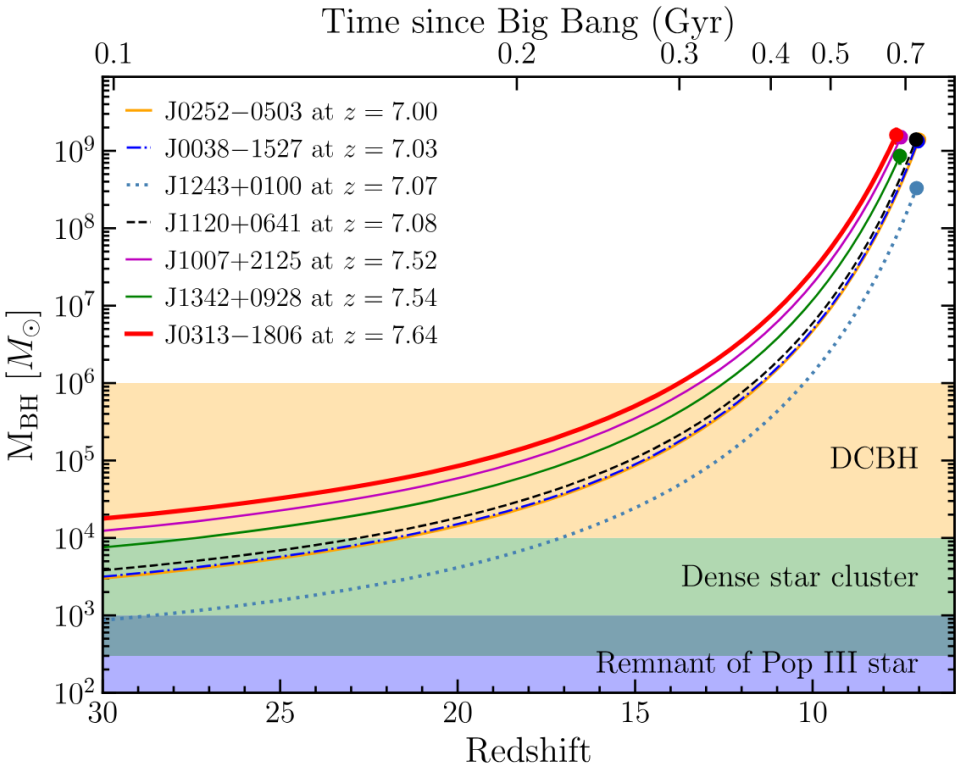

Figure 1.9: *Black hole growth tracks of $z > 7$ quasars, with the assumption of Eddington accretion and a radiative efficiency of 0.1 at all times. The blue, green, and yellow shaded regions define the mass ranges of the seed black hole produced by Population III stars, dense star clusters, and direct-collapse black holes (DCBHs), respectively. From* Wang et al., 2021 [99].

At the same time, the finding of massive galaxies in the early universe has paved the way to the evolutionary picture of the **downsizing scenario**. According to this theory, galaxies do not show the hierarchical behaviour predicted by the ΛCDM model for DM halos, but instead more massive system seem to have formed earlier over much shorter timescales (see, e.g., *Cimatti et al., 2006 [15]*), as shown in figure 1.10.
Another fundamental discrepancy emerged in the study of baryonic matter and DM is the different shape of their **mass functions**: since galaxies form at the centers of

DM halos, largely due to the capacity of baryonic matter to cool through radiative processes, we expect the mass distribution of galaxies to closely resemble that of the DM halos. In reality, however, the low and high-mass ends of the galaxy mass function show a deficit with respect to the DM mass function predicted by simulations (see, e.g., *Read & Trentham, 2005 [72]*). This has been attributed to feedback effects provided by SF processes (for the low-mass end) and AGN accretion (for the high-mass end) via radiative pressure or winds.
This picture therefore suggests that the central SMBH plays a key role in regulating the evolution of its host galaxy. In particular, a mechanism able to rapidly quench SF in the most massive galaxies is often invoked to explain both the downsizing scenario and the discrepancy between galaxy and DM mass functions (see, e.g., *Wu, 2024 [103]*). One possible evolutionary hypothesis (*Hopkins et al., 2008 [50]*) suggests that the growth of quasars and their hosts is tightly linked to the environment in which they reside: QSOs located in low-mass DM halos experience isolated, secular growth, while those nested in higher-mass halos may undergo numerous mergers from high-z to the present. It is during these events that (initially normal, proto-disks) galaxies experience an inflow of gas to the central region, which triggers SF and BH accretion episodes (*Springel et al., 2005 [89]*). These processes are believed to persist until the AGN reaches sufficient power to induce negative radiative or kinetic feedback, thereby quenching AGN (which switches from radiative-mode to jet-mode) and SF activities. In this way, most massive quasars and quasars host galaxies accumulate their mass in shorter times, in a so-called top-down scenario.

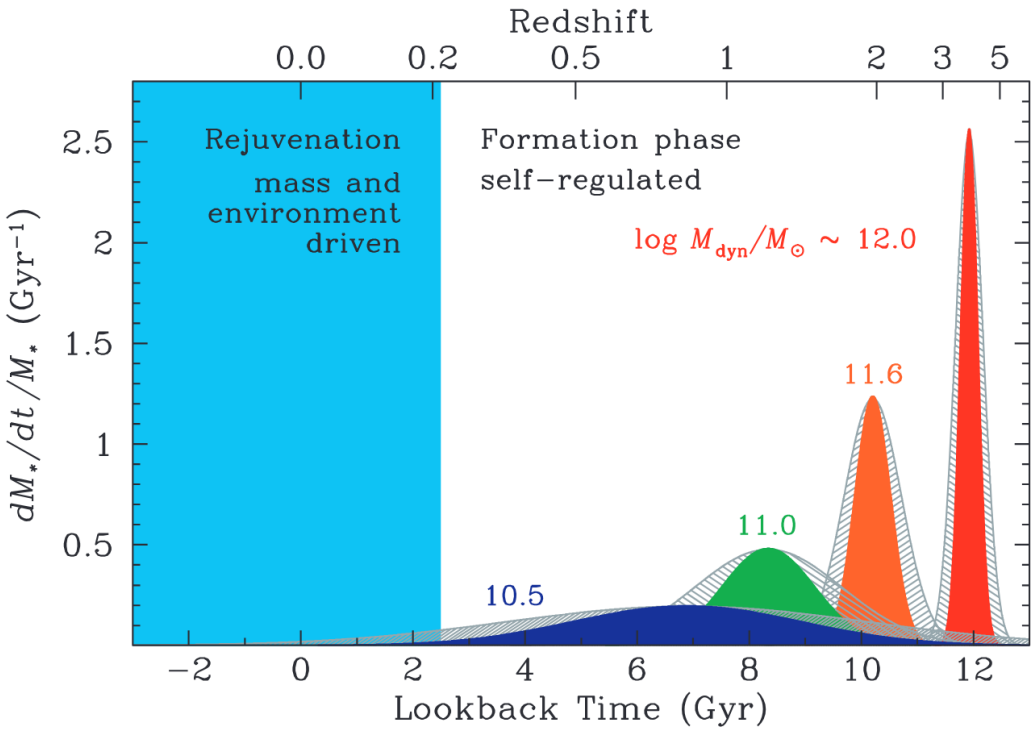

Figure 1.10: *Specific SFR as function of look-back time for ellptical galaxies of various masses (as indicated by the labels). From* Thomas et al., 2010 [91].

Other observational evidences of the SMBH being a key component in shaping the evolutionary path of its host are the numerous **scaling relations** (see *Kormendy & Ho, 2013 [58]* for a review) found in the local universe, that link its mass to the properties

of the galactic environment it resides in, such as the tight black hole mass-stellar mass correlation M_{BH}-M_* or the black hole mass-stellar velocity dispersion correlation M_{BH}-σ_* (see figure 1.11). Those findings can not be explained as result of gravitational interactions only, as the radius of the so-called sphere of influence of the BH R_{inf} is much smaller than the distance the stellar component extends to.

$$R_{inf} = \frac{GM_{BH}}{\sigma_*^2} \tag{1.10}$$

The existence of these relation therefore is the proof that there must be a way for the central SMBH to communicate its presence to the large-scale environment of its host galaxy.
To probe this influence across different cosmic times, numerous attempt have tried to study the evolution of these scaling relations with redshift. However, as already mentioned, the deblending of star emission from the AGN radiation at $z > 4$ is almost impossible, except for very few cases. Recent results revealed that in the early universe the central SMBH is overmassive with respect to its host galaxy if compared to local scaling relations, suggesting that the growth of this object preceded the one of the host (see, e.g., *Decarli et al., 2010 [21]*). However, up to date, the study of these relations at Cosmic Dawn relies on the measurement of the galaxy's dynamical mass and the assumption that it can be a valid proxy for the stellar component, as it is observed in lower-redshift galaxies.

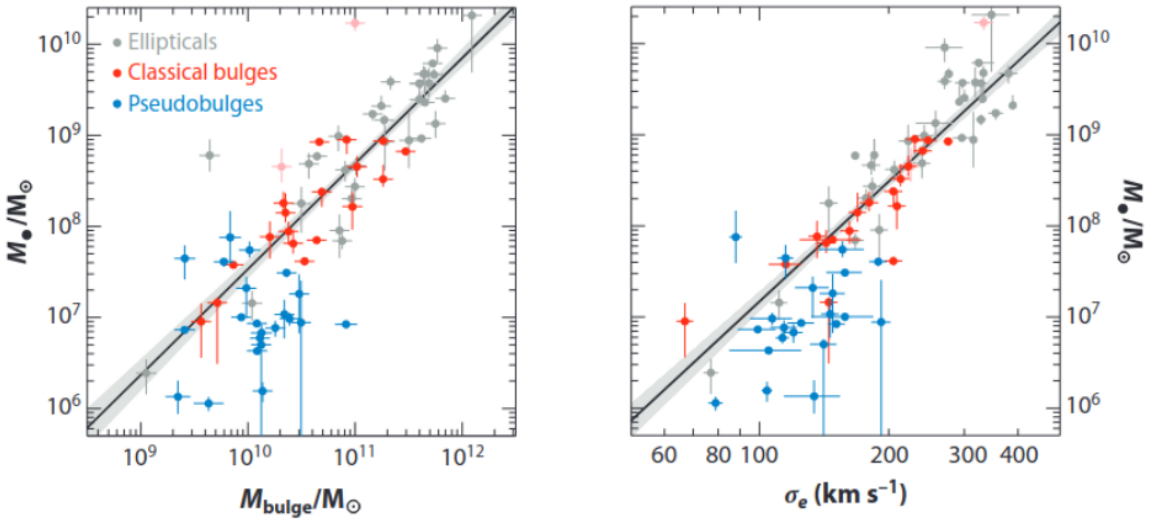

Figure 1.11: *Scaling relation between SMBH and host galaxy observed for different kinds of galaxies in the local universe.* **Left panel:** *M_{BH}-M_* correlation, with the associated best-fit line.* **Right panel:** *M_{BH}-σ_* correlation, with the associated best-fit line. From* Kormendy & Ho, 2013 [58].

1.4 Motivation and aim of the present work

In the introduction, we widely discussed the importance of observations in the mm and sub-mm regimes to dissect the emission of QSO host galaxies at large cosmological distances.

The aim of this work is to leverage the exceptional capabilities of ALMA to explore the dust continuum emission and determine the far infrared properties of 11 type 1 radio quiet QSOs located at $z > 6$. With new ALMA band 8 ($\sim$ 400 GHz) observations, we will directly measure the galaxy-wide physical properties and conditions associated with this component of the ISM, and link them to the extreme environment that characterizes high-z QSO hosts.

Among these properties, the **dust temperature** (T_d) plays a crucial role in determining the total power emitted by interstellar dust, which is closely linked to ongoing star formation processes. However, most studies involving these sources rely on the assumption of templates (which do not account for the intrinsic differences between galaxies) or on scaling relations calibrated on local objects (see, e.g., *Decarli et al., 2018 [25]* or *Sommovigo et al., 2022a [88]*). This work will provide direct measurements of T_d at the dawn of cosmic time and its evolution with redshift, which we use to investigate the view that QSO host galaxies are exceptionally efficient in forming new stars, likely due to the higher cosmological accretion rates in the early universe.

Finally, we will explore the potential influence of their luminous AGN on the derived dust properties. We will assess whether our conclusions reflect the presence of the AGN and if they can be generalized to other galaxies at high-redshift.

Summarizing, this work aims to provide:

- A direct measurement of dust-related physical properties in 11 quasar host galaxies at Cosmic Dawn.
- A coherent picture of the evolutionary properties of these sources, and insights on their relation with the bright AGN at their centre.
- A validation of the dust temperature evolution scenario suggested by previous works (*Schreiber et al., 2018 [81]*, *Bouwens et al., 2020 [10]* or *Faisst et al., 2020 [36]*), and a link between this observational trend and the properties of galaxies in the early universe.
- A brief discussion on the effects that bright AGNs may have in influencing both the intrinsic and derived physical properties of the dust.

Chapter 2

The interstellar dust

2.1 Dust interactions with radiation

In this section we introduce and explain how interstellar dust interacts with electromagnetic radiation. Understanding the physics behind these processes is the key to build reliable models that can reproduce the observed spectral energy distribution (SED) of astronomical sources, such as the ones analyzed in this work.

2.1.1 Dust extinction

When light passes through a medium composed of dust grains, it experiences the phenomenon of **extinction** (see figure 2.1). It consist of the reduction of the intensity of the incident radiation due to two physical processes, **absorption** and **scattering**. This attenuation can be quantified according to:

$$I(\lambda) = I_0(\lambda)e^{-\tau(\lambda)} \tag{2.1}$$

where $I_0(\lambda)$ is the intensity of the incident radiation, $I(\lambda)$ is the intensity of the observed radiation, and $\tau(\lambda)$ is an adimensional parameter called **optical depth**.
The optical depth is defined as:

$$\tau(\lambda) = \int_l n_d \cdot \sigma_{ext}(\lambda) dl \tag{2.2}$$

where n_d is the dust grain number density, $\sigma_{ext}(\lambda)$ the **photon-dust cross section**, and l is the length of the path crossed by the light. If we define the **mass attenuation coefficient** as $k_{ext}(\lambda) = \sigma_{ext(\lambda)}/m$, with m being the mass of the single grain, we can rewrite equation 2.2 as:

$$\tau(\lambda) = \int_l \rho \cdot k_{ext}(\lambda) dl \tag{2.3}$$

where ρ is the mass density of the dusty medium.
The product $\sigma_{ext}(\lambda) \cdot n_d$ (and thus $\rho \cdot k_{ext}(\lambda)$) has the physical meaning of the inverse of the mean free path of a photon that crosses the dusty medium. In fact, if we imagine a photon moving in a cloud of point-like dust grains, after a time t it has swept a volume of:

$$V = \sigma_{ext}(\lambda) ct \tag{2.4}$$

then, the number of interaction N_{int} this photon had with dust grains is equal to the number of grains contained inside this volume, and is given by:

$$N_{int} = n_d V = n_d \sigma_{ext}(\lambda) ct \tag{2.5}$$

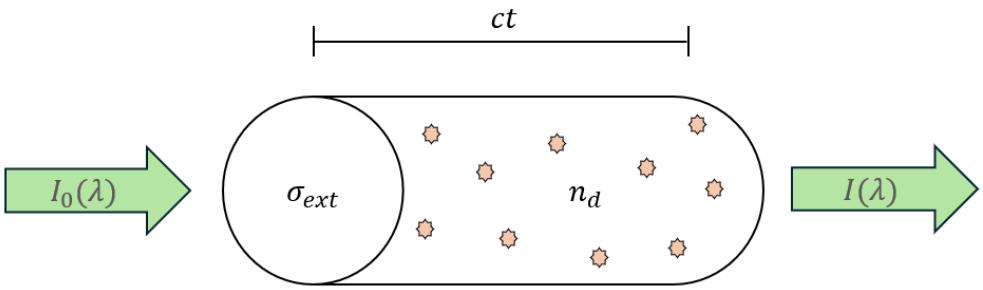

Figure 2.1: *Simple sketch of the model of dust extinction: incident radiation is either absorbed or scattered by a cloud of dust grains, and the emerging radiation results attenuated.*

The mean free path ℓ is, by definition, given by the length travelled by the photon divided by the number of the interaction it has experienced. Therefore, using equation 2.5, we can write:

$$\ell = \frac{ct}{n_d \sigma_{ext}(\lambda) ct} = \frac{1}{n_d \sigma_{ext}(\lambda)} \tag{2.6}$$

The dust cross section is therefore a fundamental parameter that rules the interaction between grains and photons.
If we define the **geometrical cross section** σ_g as the area of the projection of a spherical grain of radius a onto a plane perpendicular to the direction of the incoming photon:

$$\sigma_g = \pi a^2 \tag{2.7}$$

we can link it to the photon-dust cross section through the extinction efficiency factor $Q_{ext}(\lambda)$:

$$\sigma_{ext}(\lambda) = Q_{ext}(\lambda) \sigma_g \tag{2.8}$$

Given that radiation is either scattered or absorbed, we have that $\sigma_{ext}(\lambda)$ is the sum of the cross sections of these two processes, $\sigma_{sca}(\lambda)$ and $\sigma_{abs}(\lambda)$ respectively:

$$\sigma_{ext}(\lambda) = \sigma_{abs}(\lambda) + \sigma_{abs}(\lambda) \tag{2.9}$$

and this is true also for the associated efficiency factors:

$$Q_{ext}(\lambda) = Q_{sca}(\lambda) + Q_{abs}(\lambda) \tag{2.10}$$

where, analogously to 2.8:

$$\sigma_{sca}(\lambda) = Q_{sca}(\lambda) \sigma_g \qquad \sigma_{abs}(\lambda) = Q_{abs}(\lambda) \sigma_g \tag{2.11}$$

This implies that to fully model the interactions between dust grains and photons, it is necessary to have a theory that describes the behaviour of the efficiency factors as a

function of the wavelength (at of least two out of the three, as they are linked by 2.10).

The answer to this problem comes from **Mie theory** (*Mie, 1908 [66]*). This theory provides analytical solutions for Maxwell's equations when light is incident upon a spherical particle in the void, and is therefore an approximation of the real case scenario. Its complete derivation is quite elaborate and goes beyond the scope of this work, however we will discuss the main concepts and the results that can be extrapolated from it.
Mie theory states that, when an electromagnetic wave interacts with a spherical dust grain causes it to radiate electromagnetic radiation itself, according to the wavelength of the incident light λ and to the **complex refractive index** m. This last parameter depends on the composition of the dust grain and can be written as:

$$m(\lambda) = n(\lambda) - i\tilde{n}(\lambda) \tag{2.12}$$

the real part of it n is related to the scattering process, while the imaginary coefficient $\tilde{n}$ rules the absorption mechanism. Its value can be measured in laboratory for different materials.
The main idea behind this model is to expand both the incident light and the light radiated from the dust grain as a sum of a **vectorial spherical harmonics**. We will call c_j, d_j the expansion coefficient of the incoming wave, and a_j, b_j the expansion coefficients of the outgoing wave. In order to find an expression for a_j and b_j we impose continuity conditions at the surface of the spherical dust grain. The result is:

$$a_j = \frac{m\psi_j(mx)\cdot\psi_j'(x) - \psi_j(x)\cdot\psi_j'(mx)}{m\psi_j(mx)\cdot\xi_j'(x) - \xi_j(x)\cdot\psi_j'(mx)} \tag{2.13}$$

$$b_j = \frac{\psi_j(mx)\cdot\psi_j'(x) - m\psi_j(x)\cdot\psi_j'(mx)}{\psi_j(mx)\cdot\xi_j'(x) - m\xi_j(x)\cdot\psi_j'(mx)} \tag{2.14}$$

where ψ_j and ξ_j are the **Riccati-Bessel functions** of first and second kind respectively, and $x = 2\pi a/\lambda$ is the **size parameter**.
It is then possible to show:

$$\sigma_{ext}(\lambda, m) = \frac{\lambda^2}{2\pi}\sum_{j=1}^{\infty}(2j+1)\cdot(|a_j|^2 + |b_j|^2) \tag{2.15}$$

$$\sigma_{sca}(\lambda, m) = \frac{\lambda^2}{2\pi}\sum_{j=1}^{\infty}(2j+1)\cdot\big(\mathrm{Re}(a_j + b_j)\big) \tag{2.16}$$

from which we can calculate also the absorption cross section with equation 2.9, as well as the extinction, scattering and absorption efficiency coefficients via equations 2.8 and 2.11. In figure 2.2 we report the behaviour of these coefficients for different values of the refractive index.

If we consider the limit case of $x << 1$ (i.e. the grain size is much smaller than the wavelength of the incident radiation) we enter in the well-known case of **Rayleigh scattering**. In this scenario the values of the cross sections can be computed with the

classical treatment of Rayleigh scattering, holding:

$$\sigma_{sca,Ray}(\lambda, m) = \frac{2}{3}\pi^5 \frac{(2a)^6}{\lambda^4}\left|\frac{m^2-1}{m^2+2}\right|^2 \tag{2.17}$$

$$\sigma_{abs,Ray}(\lambda, m) = \pi\frac{(2a)^3}{\lambda}\mathrm{Im}\left(\frac{m^2-1}{m^2+2}\right) \tag{2.18}$$

from which we can again retrieve the values of the extinction cross section and of the efficiency coefficients in the Rayleigh regime.
Notice that (neglecting the wavelength dependency of the refractive index) $\sigma_{sca,Ray} \propto \lambda^{-4}$, while $\sigma_{abs,Ray} \propto \lambda^{-1}$: this mean that for long wavelengths absorption is the main source of extinction. This behaviour is also evident in figure 2.2, where we see that in the Rayleigh regime ($x << 1$) the growth of Q_{abs} is much less steep with respect the growth of Q_{sca} and is the one that shapes the behaviour of Q_{ext}.
For very high values of x (i.e. the grain size is much larger than the wavelength of the incident radiation) we have instead the **extinction paradox**:

$$\lim_{x\to\infty} Q_{ext} = 2 \qquad \Longrightarrow \qquad \lim_{x\to\infty} \sigma_{ext} = 2\sigma_g \tag{2.19}$$

This result seems to be counter intuitive, as it states that in this case the incident wave is influenced beyond the physical boundaries of the dust grain.

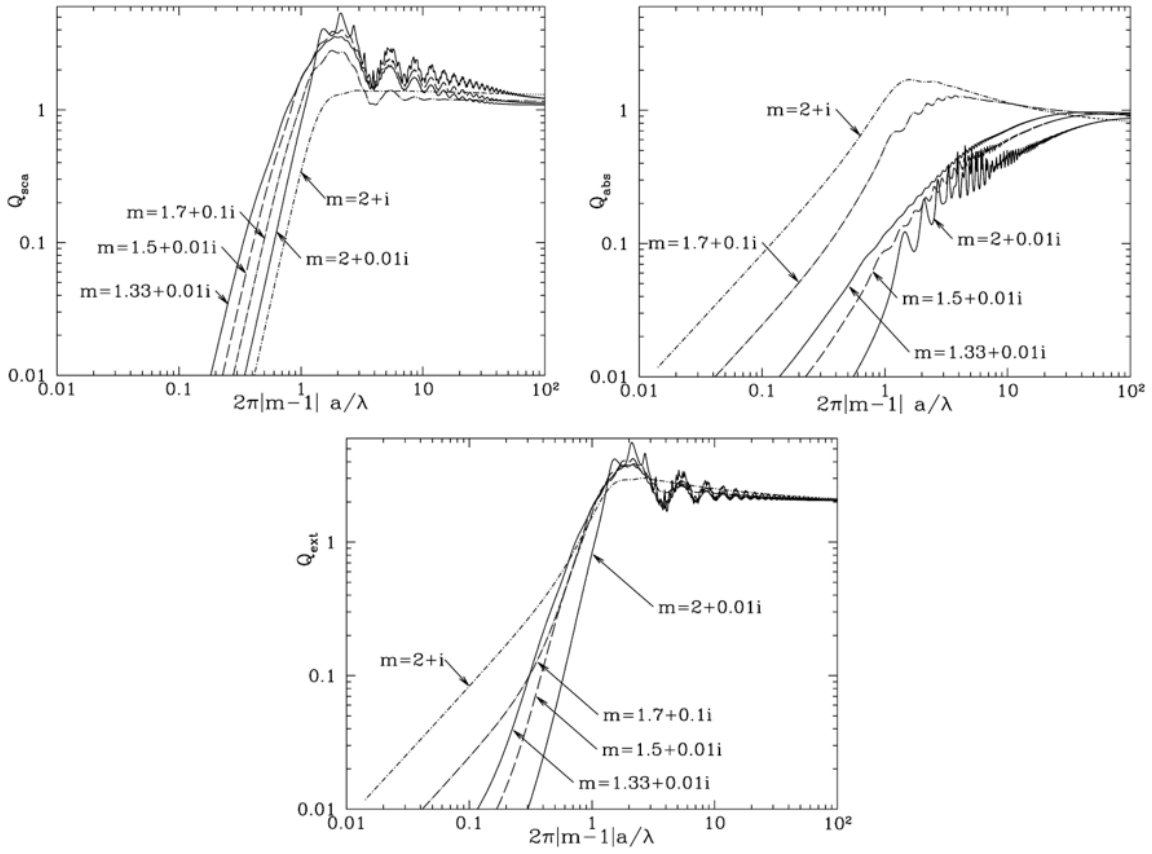

Figure 2.2: *Efficiency factors for spherical dust grains with various refractive indices. From* Bruce T. Draine, 2010 [32] .

2.1.2 Dust grains heating and cooling

Up until now we have considered only the effects that dust grains may have on incident radiation. However, Kirchhoff's Law states that a body which absorbs radiation efficiently will also emit radiation efficiently.
Specifically, for a body in thermal equilibrium at temperature T, the **absorptivity** $\alpha(\lambda, T)$ defines the fraction of incident radiation that this body absorbs at a given wavelength λ, and is expressed as:

$$A(\lambda, T) = \alpha(\lambda, T) \cdot I(\lambda) \tag{2.20}$$

where $A(\lambda, T)$ is the absorbed intensity and $I(\lambda)$ is the incident intensity. Conversely, the **emittance** $\epsilon(\lambda, T)$ represents the fraction of radiation emitted by the body compared to the radiation emitted by a blackbody having the same temperature, and is given by:

$$E(\lambda, T) = \epsilon(\lambda, T) \cdot B(\lambda, T) \tag{2.21}$$

where $E(\lambda, T)$ is the emitted intensity and $B(\lambda, T)$ is the blackbody intensity.
Kirchhoff's Law for radiation states that, for a body in thermal equilibrium, the absorptivity equals the emittance:

$$\alpha(\lambda, T) = \epsilon(\lambda, T) \tag{2.22}$$

By definition a blackbody absorbs all incident electromagnetic radiation and re-emits it according to Planck's law. This implies that $\alpha(\lambda, T) = \epsilon(\lambda, T) = 1$. However, as explained in the previous subsection, dust is not a blackbody, given that it is not able to absorb all the incident light. In this case the body is called **graybody** and $\alpha(\lambda, T) = \epsilon(\lambda, T) < 1$.

Upon photon absorption, the dust grain transitions to an excited state, with a spontaneous re-emission probability of $\sim 10^{-7}\,\mathrm{s}^{-1}$. However, dust grains consist of complex molecules with multiple excited states, allowing the absorbed photon's energy to be redistributed into internal vibrational modes, heating the grain within $\sim 10^{-12}\,\mathrm{s}$. Since the timescale of energy redistribution is much shorter with respect to spontaneous emission's timescale, most of the absorbed photons effectively contribute to heating the dust grains to a certain equilibrium temperature T. After being heated, grains will cool via thermal radiation emission.
For a spherical dust grain the power absorbed can be expressed as the integration over all the frequencies of the rate of the photon-grain absorption interactions $f(\nu)$, times the energy acquired by the grain in that interaction $q(\nu)$:

$$\left(\frac{d\varepsilon}{dt}\right)_{abs} = \int_0^\infty f(\nu) \cdot q(\nu) d\nu \tag{2.23}$$

and given that $f(\nu) = n_\gamma(\nu)\sigma_{abs}(\nu)c$, with $n_\gamma(\nu)$ being the photon number density of the incident radiation, and $q = h\nu$, we can substitute to obtain:

$$\left(\frac{d\varepsilon}{dt}\right)_{abs} = \int_0^\infty n_\gamma(\nu)\sigma_{abs}(\nu)c \cdot h\nu d\nu \tag{2.24}$$

knowing that $n_\gamma(\nu) = u(\nu)/h\nu$, where $u(\nu)$ in the energy density per unit frequency of the incident radiation field, we can substitute again to get:

$$\left(\frac{d\varepsilon}{dt}\right)_{abs} = \int_0^\infty u(\nu)\sigma_{abs}(\nu)cd\nu = \pi a^2 c \int_0^\infty u(\nu) Q_{abs}(\nu) d\nu \tag{2.25}$$

Then, since $u(\nu) = 4\pi I(\nu)/c$, where again $I(\nu)$ is the intensity of the incident radiation, we can write:

$$\left(\frac{d\varepsilon}{dt}\right)_{abs} = 4\pi a^2 \int_0^\infty \pi I(\nu) Q_{abs}(\nu) d\nu \tag{2.26}$$

As explained in the previous subsection, the absorption efficiency factor is very hard to parameterize, as it is linked to the refractive index, which depends on the material. Moreover, dust grains in a cloud may have different compositions, thus making the real case scenario more complicate. It is useful then to define the **spectrum averaged efficiency factor** $\langle Q_{abs} \rangle_I$ as:

$$\langle Q_{abs} \rangle_I = \frac{\int_0^\infty \pi I(\nu) Q_{abs}(\nu) d\nu}{S_{bol}} \qquad S_{bol} = \int_0^\infty \pi I(\nu) d\nu \tag{2.27}$$

where S_{bol} is the bolometric flux of the incident radiation field. $\langle Q_{abs} \rangle_I$ represents the mean value of $Q_{abs}(\nu)$ over all the frequencies, weighted on the intensity of the incident radiation field. Combining the definitions of equation 2.27 with equation 2.26 leads to:

$$\left(\frac{d\varepsilon}{dt}\right)_{abs} = \langle Q_{abs} \rangle_I 4\pi a^2 S_{bol} \tag{2.28}$$

A similar approach can be applied to the power emitted by the dust grain: if we imagine that it radiates as a blackbody over the spherical surface associated to its cross section, we can write the emitted power as

$$\left(\frac{d\varepsilon}{dt}\right)_{em} = 4\pi a^2 \int_0^\infty \pi B(\nu, T) Q_{abs}(\nu) d\nu \tag{2.29}$$

In analogy to what we did for the absorbed power, we can again define a weighted average of $Q_{abs}(\nu)$, this time using as weight the blackbody intensity;

$$\langle Q_{abs} \rangle_{B(T)} = \frac{\int_0^\infty \pi B(\nu, T) Q_{abs}(\nu) d\nu}{S_{bol,bb}} \qquad S_{bol,bb} = \int_0^\infty \pi B(\nu, T) d\nu \tag{2.30}$$

where $S_{bol,bb}$ is the bolometric flux measured on the surface of a blackbody. We call $\langle Q_{abs} \rangle_{B(T)}$ **Planck averaged efficiency factor**. It is then immediate to show that, combining the definitions of equation 2.30 with equation 2.29, and then substituting $S_{bol,bb} = \sigma_b T^4$ (according to Stefan-Boltzmann Law, with σ_b being the Stefan-Boltzmann constant):

$$\left(\frac{d\varepsilon}{dt}\right)_{em} = \langle Q_{abs} \rangle_{B(T)} 4\pi a^2 S_{bol,bb} = \langle Q_{abs} \rangle_{B(T)} 4\pi a^2 \sigma_b T^4 \tag{2.31}$$

Now we can compare dust absorption and emission. We can see from equation 2.26 that the bulk of energy absorption happens in the infrared, optical and ultraviolet bands, given the fact that the major contribution to the incident intensity $I(\nu)$ comes from stellar emission, peaking at those frequencies. On the other side, from equation 2.29 it is possible to notice that most of the dust emission occurs in the far infrared band, as dust temperatures are usually in the range of 10-100K.

To date, a complete and rigorous model to describe $\sigma_{abs}(\nu)$ is still missing: the chemical composition and shapes of dust grains are not yet fully unveiled, and at the same time these parameter may be highly variable, depending to the astronomical source taken

into consideration. The prevailing theory, however, describes dust grains as primarily consisting of carbonaceous or silicon based compounds, with the possibility of purely metallic grains also being considered (see e.g. *Draine, 2003 [31]*). In this case $Q_{abs}(\nu)$ is usually approximated as a power law in frequency:

$$Q_{abs}(\nu) = Q_0 \left(\frac{\nu}{\nu_0} \right)^{\beta} \tag{2.32}$$

with β being called **emissivity index**. If this formulation is assumed, it is then possible to compute analytically the Planck averaged efficiency factor using equation 2.30. We obtain:

$$\langle Q_{abs} \rangle_{B(T)} = \frac{15}{\pi^4} \Gamma(4+\beta) \zeta(4+\beta) Q_0 \left(\frac{kT}{h\nu_0} \right)^{\beta} \tag{2.33}$$

where Γ and ζ are the Euler gamma function and the Riemann zeta function respectively, k the Boltzmann constant, and h the Planck constant. Plugging this expression in equation 2.31 shows finally a fundamental result:

$$\left(\frac{d\varepsilon}{dt} \right)_{em} \propto T^{4+\beta} \tag{2.34}$$

In other words, the power emitted by the single dust grain is highly sensitive to its temperature. Consequently, accurate estimates of the dust grain's temperature are essential to reliably constrain its total emission.

2.1.3 Dust emission

As we previously mentioned, dusty astronomical objects emit as a graybody, peaking in the far infrared band. Solving the radiative transfer equation, we get that the intensity of radiation of such graybody can be expressed as:

$$I(\nu) = B(\nu, T)(1 - e^{-\tau(\nu)}) \tag{2.35}$$

Notice here how the term $(1 - e^{-\tau(\nu)})$ can be seen, if we compare equations 2.21 and 2.35, as the emittance of the astronomical source taken into consideration, and is by definition smaller than unity.
However, the physical quantity that is estimated via astronomical observations is the **flux**, which is defined as the power per unit area per unit frequency coming from a source in the sky covering a solid angle Ω. In this case, the flux of a graybody at redshift z and observed at a frequency $\nu_{obs} = \nu/(1+z)$, can be expressed as (see, e.g., *Decarli et al., 2023 [22]*, *Tripodi et al., 2024 [93]*):

$$S(\nu_{obs}) = \frac{\Omega}{(1+z)^3} [B(T_d(z), \nu) - B(T_{CMB}(z), \nu)](1 - e^{-\tau(\nu)}) \tag{2.36}$$

this formula is derived from equation 2.35 taking into account that:

- The astronomical source appears very small in the sky, so that the flux can be computed as the product between the intensity and the effective angle over which it emits.

- The observed angle covered by the source Ω is linked to the surface area A_g and the luminosity distance D_L as $\Omega = A_g(1+z)^4/D_L^2$, while the intrinsic angle over which the source emits is of a factor $(1+z)^4$ smaller.
- The observed flux is enhanced of a factor $(1+z)$, as the quantity $\nu S(\nu)$ has to be conserved.
- The measured flux is not directly linked to the intensity emitted from the graybody, but to the intensity contrast between the source and the cosmic microwave background (CMB), with $T_{CMB}(z) = 2.73(1+z)$K.

At the same time we can the link optical depth τ_{ext} to some physical parameters of the source: assuming that $k_{ext}(\nu)$ is constant all over the emitting region it is possible to rewrite 2.3 as a function of A_g and of the total dust mass M_d

$$\tau_{ext}(\nu) = k_{ext}(\nu)\frac{M_d}{A_g} \tag{2.37}$$

Finally, given that we assumed a power law distribution for Q_{ext} (see previous subsection), it is possible to model also $\tau_{ext}(\nu)$ using the same law. This follows from the fact that $n_d \cdot \sigma_{ext}(\nu) = \rho \cdot k_{ext}(\nu)$.

$$k_{ext}(\nu) = k_0\left(\frac{\nu}{\nu_0}\right)^{\beta} \tag{2.38}$$

In the optically thin limit (i.e. when $\tau << 1$) equation 2.36 can be simplified thanks to a Taylor series expansion of the exponential term:

$$S(\nu_{obs}) \simeq \frac{(1+z)}{D_L^2}[B(T_d(z),\nu) - B(T_{CMB}(z),\nu)]k(\nu)M_d \tag{2.39}$$

This last expression is of quite simpler usage in the process of fitting a model to the observed data, as it gets rid of the dependence on the solid angle Ω, which can be difficult to accurately measure. Furthermore, we can easily integrate it to obtain the infrared-emitted luminosity L_{IR}:

$$L_{IR} = 4\pi D_L^2 \int_0^{\infty} S(\nu)d\nu$$

$$L_{IR} = 4\pi M_d k_0 \nu_0^{-\beta}\Gamma(\beta+4)\zeta(\beta+4)\frac{2h}{c}\left[\left(\frac{k_B T_d(z)}{h}\right)^{4+\beta} - \left(\frac{k_B T_{CMB}(z)}{h}\right)^{4+\beta}\right] \tag{2.40}$$

where we remind that $\nu = (1+z)\nu_{obs}$ and $S(\nu) = S(\nu_{obs})/(1+z)$. This final expression for luminosity retains the same temperature dependence observed in the single grain case. This result is reasonable, as in the optically thin limit we neglect the effects of radiative transfer, an aspect that is intrinsically implied in the single grain scenario as well. However, the optically thin limit may not be always a safe assumption, especially at higher frequencies. This issue will be discussed more in depth in subsection 4.1.1, in view also of the results obtained in this work.
In the end, the set of equations 2.36 (or 2.39), 2.37 and 2.38 results in a full model for a source that emits as a graybody at a single temperature.

The emission from dust in galaxies or quasars, however, may not always be accurately

approximated by such assumption. For a more precise analysis, it would be beneficial to model the emission using multiple graybody components with different dust temperatures. Some works (see, e.g. *Galametz et al., 2012 [43]*) suggest that in normal galaxies the heating of a **cold dust component**($T_d \simeq 20$K) may be due to the global starlight radiation field, including evolved stars, while a **warm dust component**($T_d \simeq 60$K) is associated to the emission from star-forming regions. These two components are shown in figure 2.3.
In high-redshift QSOs, such as the ones analyzed in this work, the picture may be similar. For instance, in *Tsukui et al., 2023 [94]*, the heating of the warm dust component is attributed mainly to the central AGN, which is able to set a strong gradient in temperature across the source. In this work, the Authors explain the emission at higher frequencies with a second graybody component with $T_d \simeq 95$K emerging from the innermost element of resolution.
The issue of the presence of multiple dust components at different temperatures, and how it may affect the results presented in this work, will be discussed in section 4.3.

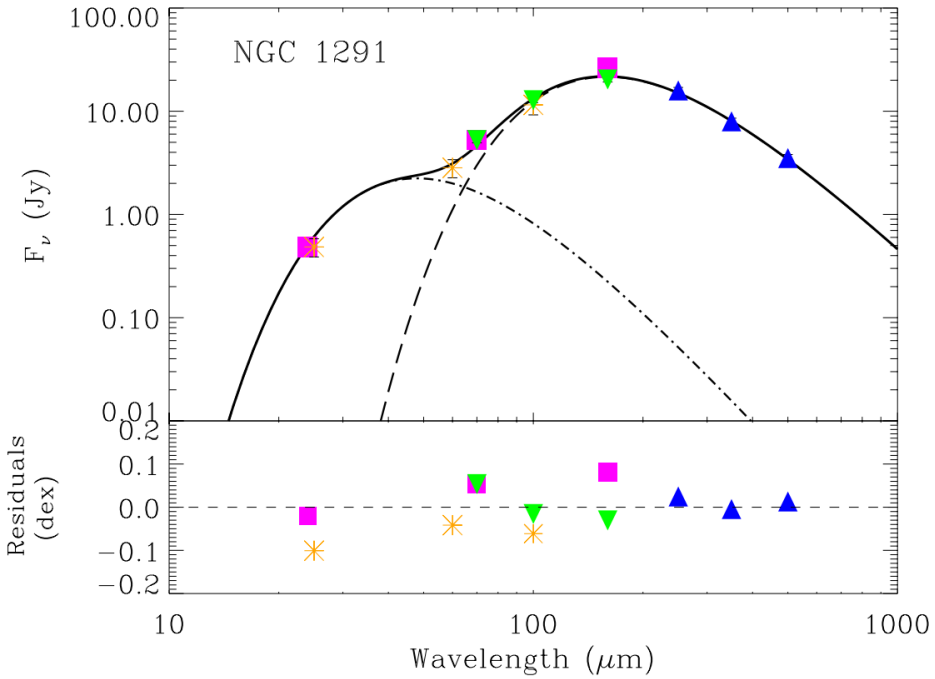

Figure 2.3: *Spectral energy distribution of the local galaxy NGC 1291 fitted with a two component model for the emission of dust. From* Galametz et al., 2012 [43].

2.2 Dust physical properties and life cycle

In this section, we provide an overview of the physical properties of interstellar dust. Our main focuses will be its composition and the processes ruling its formation and destruction.

2.2.1 Dust grain composition and shape

As briefly mentioned in the previous section, dust grains (figure 2.4) are believed to be composed of refractory materials like carbon or silicon compounds, often coated with volatile ices of molecules such as water or carbon dioxide. The existence of purely metallic grains has also been proposed.

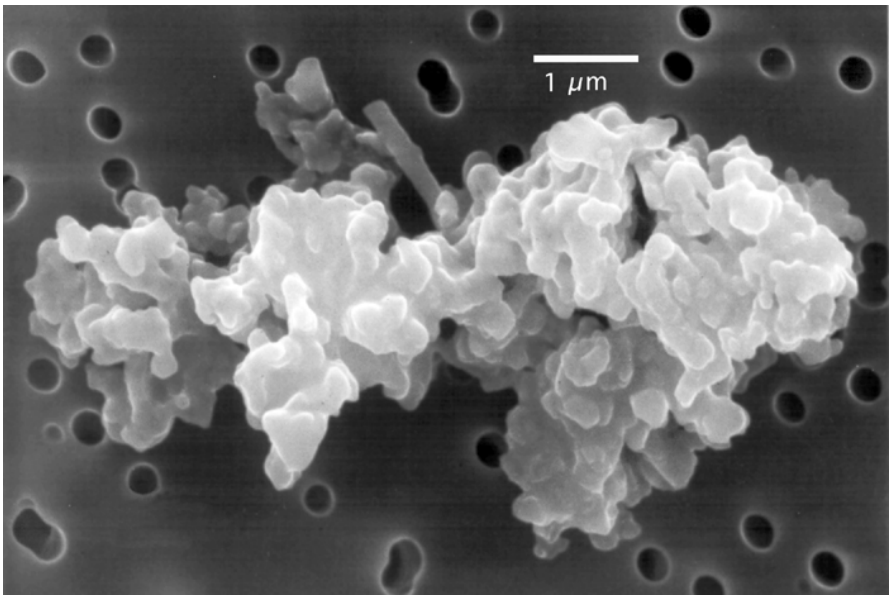

Figure 2.4: *Electron microscope image of an interplanetary dust particle aggregate. From* Eberhard Grün, Bo Å. S. Gustafson, Stan Dermott, Hugo Fechtig, 2001 [46].

The composition of dust grains can be determined either by directly studying cometary and meteoritic dust, or by modelling the observed extinction considering mixtures of different grains, each one with a specific refractive index. In general, **silicates** are expected to contribute significantly to the total dust mass in the interstellar medium, with **carbonaceous compounds** following as the next major component. In particular, current extinction models are computed accounting for the presence of graphite, enstatite, olivine, silicon carbide, iron, and magnetite.

Despite the widespread assumption of spherical geometry, which allows for simple analytic solutions, there is still debate on the actual grain shape. Dust grains in reality can not be simple spheres, as this assumption would be unable to explain the polarization observed both in dust-emitted light and in dust-attenuated background radiation (see, e.g. *Draine, 2024 [33]*).
Regarding grain size, the observed behaviour of extinction can be reproduced very well if both grain components (carbonaceous and silicates) had **power-law size distribution** (*Mathis et al., 1977 [63]*):

$$N(a) \propto a^{-\delta} \tag{2.41}$$

truncated at a minimum size $a_{min} = 0.005$ μm and at a maximum size of $a_{max} = 0.25$ μm, with $\delta = -3.5$.

2.2.2 Life cycle of dust grains

Interstellar dust is thought to form mainly in the surroundings of evolved Asymptotic Giant Branch (AGB) stars and, in a negligible amount (at least for the local universe), in the ejecta of supernova explosions (SNe).
Around AGB stars we observe the formation of dense and cold shells made of both matter that was already present when the star was born, and elements that were synthesized during its lifetime. These places can be considered nurseries of dust grains, as it is here that the first step of their formation, the **nucleation**, occurs. During this phase, elements that are present in gaseous form condensate to form stable nuclei, the chemical composition of which depends on the abundances of heavy elements in the outermost layers of the star. Once formed, dust will be accelerated by the radiation pressure provided by the star itself, and will end up feeding the diffuse interstellar medium (ISM).
The nucleation phase is followed by the **accretion** step, during which the ambient gas, atoms or molecules, condense on the surface of newborn nuclei, making them experience a rapid growth in the cold ISM. This step is a crucial point in the grains' life cycle (see figure 2.5), as dust produced only by AGB stars fails to explain the observed dust masses in sub-millimeter galaxies, giving origin to the well known **dust-budget crisis**. Even after accounting for the mass released in the ISM by SNe we are left with a substantial deficit, which has been considered proof of substantial grain growth in the interstellar medium, especially in high-redshift galaxies (*Rowlands et al., 2013 [76]*).

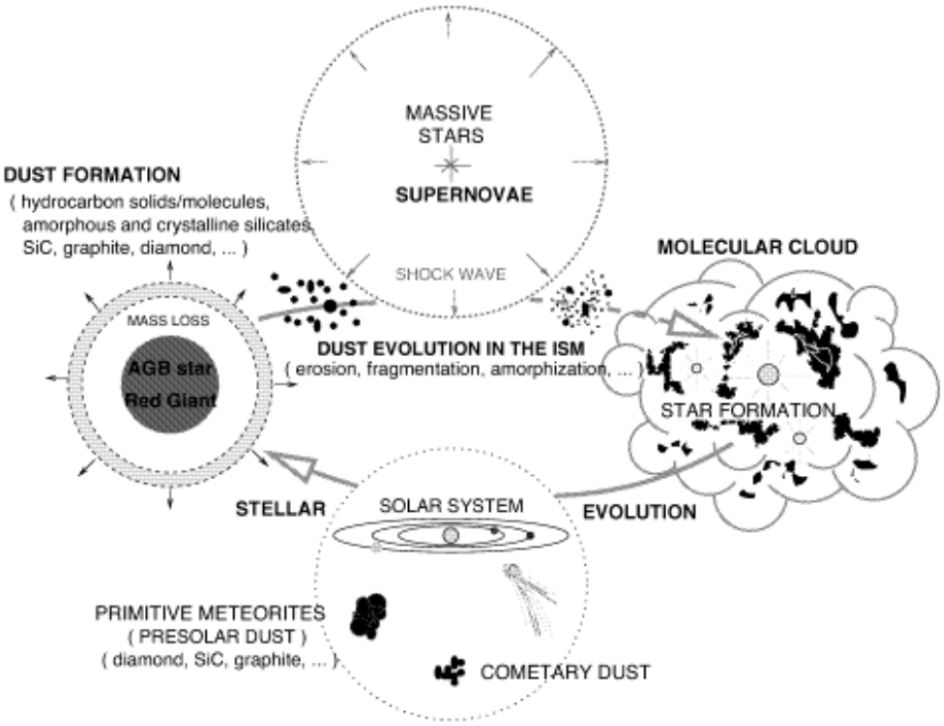

Figure 2.5: *Schematic representation of dust life cycle in the ISM. From* Jones, 2004 [55].

As discussed, being produced in the final stages of the stellar evolution of massive stars, cosmic dust is associated to regions of intense star formation and therefore its luminosity can be used to reliably estimate SFRs. The peculiar physical conditions of these places shape the evolution of grains, and in particular SNe play a key role in their destruction.
The dominant means of destruction for grains is in fact via fast shock waves, mostly generated in the ISM by these energetic events. Grains are destroyed in shocks by a variety of processes such as sputtering or shattering caused by grain–grain collisions. Dust evolution models estimate the destruction timescale of grains in the ISM to be $6 \cdot 10^8$ and $4 \cdot 10^8$ years for graphite and silicates, respectively. This result would imply that most of the interstellar dust volume has to be condensed in the ISM and not in the proximity of AGB stars (see, e.g., *Draine, 1990 [30]*).

Chapter 3

Methods and data analysis

3.1 Introduction to ALMA and to interferometric observations

In this section we introduce the basics of the theory behind interferometric observations and we illustrate the main properties of the *Atacama Large Millimeter/Submillimeter Array* (ALMA), from which the data used in this work are taken.

3.1.1 Basics of single dish observations

Observations in the mm/submm bands are based on the interferometric technique. It consists in the simultaneous observations of an astronomical source with multiple antennas, and is the key to achieve measurements that have at the same time high angular resolution and good sensitivity. To explain the functioning of interferometers we have therefore to start with the presentation of their constituting elements, the antennas. The purpose of an antenna is to convert the light coming from an astronomical source in an electric signal that can be measured by the instrumentation.
We start by defining the **effective area** A_e as the ratio between the available power at the terminals of a receiving antenna and the power flux density of a plane wave incident on the antenna. This quantity depends on the direction of the incident wave and describes the sensitivity of the antenna to light incident upon it. The **beam solid angle** Ω_A (which physically represent the angle underneath which all the radiation would be confined if the effective area were constant and equal to it's maximum A_0) depends on how the effective area changes as function of the inclination angle. Calling θ the offset angle of the source with respect the normal to the telescope aperture and D the antenna's diameter, it can be shown that for a uniformly illuminated aperture:

$$A_e \propto sinc^2\left(\frac{\theta D}{\lambda}\right) \tag{3.1}$$

$$\Omega_A = \int_{4\pi} \frac{A_e(\theta)}{A_0} d\Omega \simeq 1.133 \cdot \theta^2_{HPBW} \tag{3.2}$$

where θ_{HPBW} is the angle defined by the amplitude of the main lobe of the A_e function measured at $A_e = A_0/2$. It has not to be confused with θ_{BWFN} which is the angle defined by the amplitude of main lobe of the A_e function measured at $A_e = 0$. It can

be proved that:

$$\theta_{HPBW} \simeq 0.89\frac{\lambda}{D} \qquad \theta_{BWFN} = \frac{2\lambda}{D}$$

In figure 3.1 we report the physical representation of the quantities that we introduced.

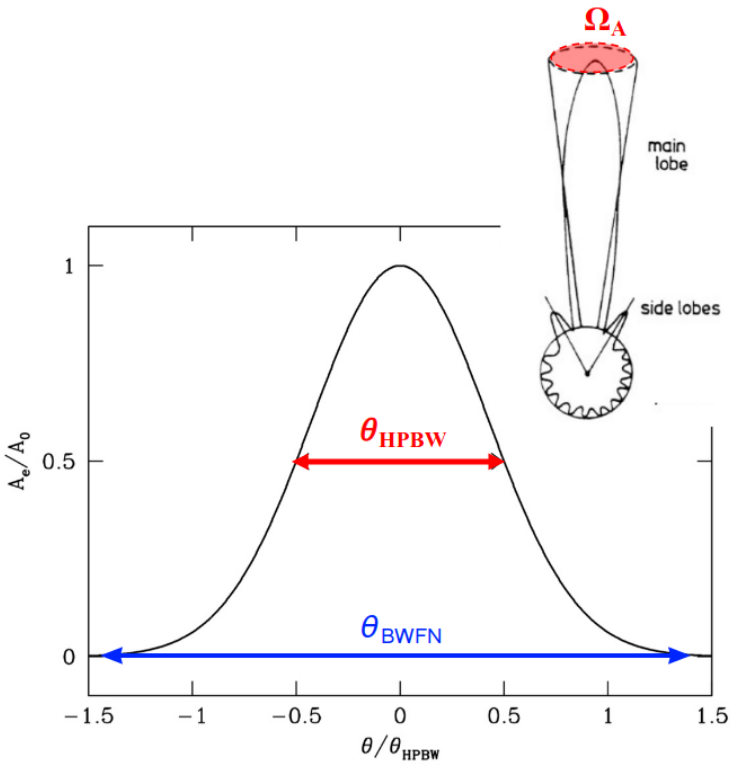

Figure 3.1: *Effective area as function of the inclination angle. Adapted from* James J. Condon, Scott M. Ransom, 2016 [54].

We can now introduce two fundamental quantities: the **angular resolution**, and the **field of view**. The angular resolution corresponds to θ_{HPBW} because two equal point sources separated by this angle are just resolved by the Rayleigh criterion that the total response has a minimum midway between the point sources. On the other hand the field of view corresponds to θ_{BWFN} because it tells us the amplitude of the angle inside of which we are able to effectively gather radiation.
In the case of single dish we can notice that increasing the diameter of our aperture will lead to an improved resolution but will affect negatively the field of view.

3.1.2 Basics of interferometry

Interferometers allow to combine signals from multiple antennas, thus improving the performance of the telescope. They consist of an array of multiple antennas whose output voltages are correlated, meaning that they are first multiplied and then time-averaged (taking into account the phase-shift given by the different optical paths, see figure 3.2). The result of this correlation will be:

$$R = \langle V_1 V_2 \rangle = \left(\frac{V_1 V_2}{2}\right) cos(\omega \tau_g) = \left(\frac{V_1 V_2}{2}\right) cos(\varphi) \tag{3.3}$$

$$\tau_g = \frac{b \cdot sin\theta}{c} \qquad \varphi = 2\pi \frac{b}{\lambda} sin\theta$$

where $\omega = 2\pi\nu$, with ν being the frequency of the wave, V_1 and V_2 are the output voltages of the two antennas, and b is the separation between the two antennas (also called **baseline**). The parameters τ_g and φ are called **geometric delay** and **phase difference** respectively.
However, it is convenient to express the response of the interferometer with respect to a reference position on the sky, usually the nominal position of the source under observation θ_0. This is commonly referred to as the **phase reference position**. Because of this reason, an instrumental delay τ_i is introduced and is constantly adjusted to equal the geometric delay τ_g for radiation coming from the phase reference position. This allows us to write:

$$\tau_g = \frac{b \cdot sin(\theta_0 - \Delta\theta)}{c} \qquad \tau_i = \frac{b \cdot sin\theta_0}{c} \tag{3.4}$$

where $\Delta\theta$ is the angle with respect the phase reference position. Introducing the correction given by the instrumental delay in equation 3.3 we get:

$$\begin{aligned} R &= \left(\frac{V_1 V_2}{2}\right) cos\Big(\omega(\tau_g - \tau_i)\Big) \\ &= \left(\frac{V_1 V_2}{2}\right) cos\left(2\pi\nu\left(\frac{b \cdot sin(\theta_0 - \Delta\theta)}{c} - \tau_i\right)\right) \end{aligned} \tag{3.5}$$

therefore, assuming small angle approximation for $\Delta\theta$ ($cos\Delta\theta \simeq 1$), we finally have:

$$R \simeq \left(\frac{V_1 V_2}{2}\right) cos\Big(2\pi \frac{b}{\lambda} sin\Delta\theta \cdot cos\theta_0\Big) \tag{3.6}$$

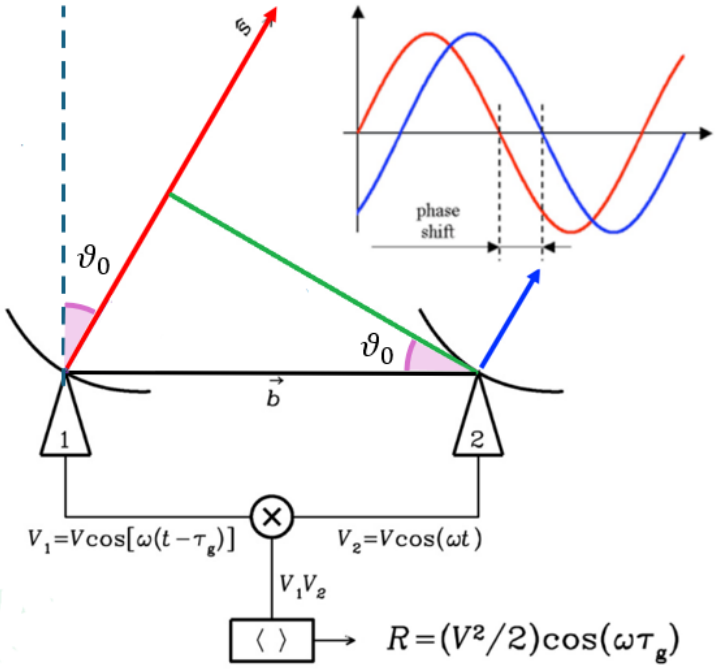

Figure 3.2: *Sketch of a two-antennas array, θ_0 is the phase reference position and in green is depicted the projected baseline. Adapted from* James J. Condon, Scott M. Ransom, 2016 [54].

The voltages are proportional to the brightness distribution of the source I multiplied by the effective area of the two antennas. If we assume that both antennas are pointed towards the phase reference position, recalling equation 3.1 and substituting in equation 3.6, it is possible to write:

$$\begin{aligned} R &\propto I \cdot (A_1 A_2)^{1/2} \cdot cos\left(2\pi \frac{b}{\lambda} sin\Delta\theta \cdot cos\theta_0\right) \\ R &\propto sinc^2\left(\frac{D}{\lambda}\Delta\theta\right) \cdot cos\left(2\pi \frac{b}{\lambda} sin\Delta\theta \cdot cos\theta_0\right) \end{aligned} \tag{3.7}$$

The first factor goes as a cardinal sine squared, and represents the response of the single dish. The second one goes as the cosine of a sine, and will lead the response to assume a shape characterized by interferometric fringes, with the first maximum in $\Delta\theta = 0$. The result will therefore be a oscillating function modulated by a cardinal sine squared function, as illustrated in figure 3.3. This kind of response of an interferometer to a point source is called **dirty beam**.
It is therefore possible to apply a new definition of angular resolution and field of view. Two point sources will be resolved if their distance is bigger than the spacing between two maxima of the fringing pattern. Assuming again small angle approximation ($sin\Delta\theta \simeq \Delta\theta$), the positions of the maxima of the cosine factor are given by:

$$\begin{aligned} 2\pi \frac{b}{\lambda}\Delta\theta \cdot cos\theta_0 &= 2k\pi \\ \Delta\theta &= k\frac{\lambda}{b \cdot cos\theta_0} \end{aligned} \tag{3.8}$$

where k is an integer. We see that they have an angular separation, which is by definition the angular resolution of the interferometer, equal to:

$$ang.res. = \frac{\lambda}{b \cdot cos\theta_0} \tag{3.9}$$

As for the field of view, it is again defined by the first null of the cardinal sine (that in this case is also called **primary beam**), and keeps the proportionality with λ/D that is observed also in the single dish case:

$$f.o.v = \frac{2\lambda}{D} \tag{3.10}$$

Our observation can be further improved using multiple-antennas arrays: the number of responses will be now $N(N-1)/2$, with N being the number of antennas. We call **synthesized beam** the arithmetic mean of all these responses, and because of the central limit theorem the main lobe of the synthesized beam will rapidly approach a Gaussian shape.
The maximum and the minimum baseline play here a fundamental role. In fact, if a source is smaller than the fringe distance given by the maximum baseline, it means that it is smaller than our angular resolution and we will observe its emission smeared over the synthesized beam. At the same time if a source has angular size bigger than the fringe distance given by our minimum baseline, its emission will be spread over positive and negative interferometric fringes, which will start to cancel it out.
This means that an interferometer is sensitive only to a range of angular sizes smaller than $\lambda/(b_{min} \cdot cos\theta_0)$, with resolution $\lambda/(b_{max} \cdot cos\theta_0)$, over a field of view $2\lambda/D$.

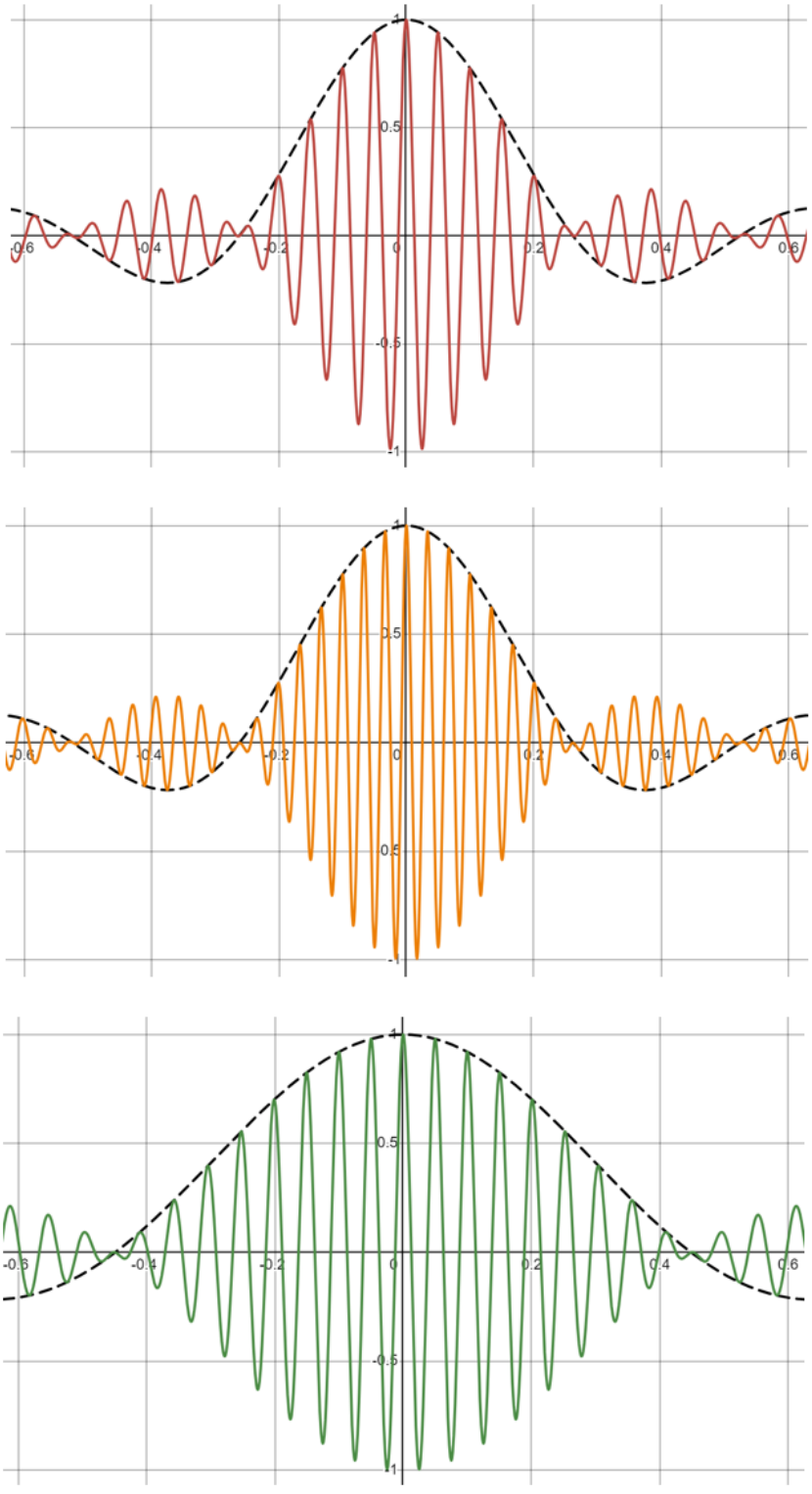

Figure 3.3: *Normalized response of a two antenna interferometer operating at the zenith and at λ=1m, as function of $\Delta\theta$. The black dashed line represents the single-dish response. First panel: response of an interferometer with baseline separation b=20m and antennas diameter D=12m. Second panel: response of an interferometer with baseline separation b=30m and antennas diameter D=12m. Third panel: response of an interferometer with baseline separation b=20m and antennas diameter D=7m. The adopted wavelength is much higher with respect of typical observational wavelengths of interferometers just for visualization purposes.*

3.1.3 Extended sources and visibilities

If a source with surface brightness distribution $I(\hat{s})$ is slightly extended we can treat it as a sum of independent point sources. In this case the response is:

$$R_c = \int_{4\pi} I(\hat{s}) A_e(\hat{s}) \cdot cos\left(2\pi \frac{\vec{b}}{\lambda} sin\Delta\theta \cdot \hat{s}\right) d\Omega \tag{3.11}$$

where $\vec{s} = \vec{s_0}$ is the vector pointing towards the phase center position (see figure 3.4), and the effective area A_e takes into account for the $sinc^2$ factor in equation 3.7.
The cosine function is sensitive only to the even part of an arbitrary source brightness distribution I, which can be written as the sum of even and odd parts $I = I_E + I_O$. Therefore, in order to detect the odd part I_O, we need a correlator whose output is odd, a sine correlator. This can be implemented introducing a second correlator that follows a $\pi/2$ phase delay inserted into the output of one antenna, since $sin(\omega\tau_g) = cos(\omega\tau_g - \pi/2)$:

$$R_s = \int_{4\pi} I(\hat{s}) A_e(\hat{s}) \cdot sin\left(2\pi \frac{\vec{b}}{\lambda} sin\Delta\theta \cdot \hat{s}\right) d\Omega \tag{3.12}$$

The combination of these two responses is given by what we call a complex correlator. It is called this way because it is mathematically convenient to treat cosines and sines as complex exponentials:

$$e^{i\alpha} = cos\alpha + i \cdot sin\alpha \tag{3.13}$$

The response of a complex correlator will be the algebraic sum of the two responses R_c and R_s and it is called **complex visibility**:

$$\mathcal{V} = R_c - i \cdot R_s = A \cdot e^{-i\phi} \tag{3.14}$$

$$A = \sqrt{R_c^2 + R_s^2} \qquad \phi = arctan\left(\frac{R_s}{R_c}\right)$$

This means that:

$$\mathcal{V} = \int_{4\pi} I(\hat{s}) A_e(\hat{s}) \cdot e^{\left(-2\pi i \frac{\vec{b}}{\lambda}\hat{s}\right)} d\Omega \tag{3.15}$$

In other words our data (complex visibilities) are complex numbers defined by an **amplitude** A and a **phase** ϕ.

3.1.4 Interferometric imaging

In order to get the surface brightness distribution if the observed source we need to reverse equation 3.15.
We hence introduce the reference system called (u, v) plane. It can be imagined as a virtual plane perpendicular to the vector $\vec{s_0}$ and represents the spatial distribution of the baselines, in unit of λ, as seen from a source at very large distances (see figure 3.4). To complete the description of our system we introduce also the (l, m) plane, which is the projection of the celestial sphere onto a plane with tangent point defined by $\vec{s_0}$. Using these coordinate systems we can notice that the complex visibility $\mathcal{V}(u, v)$ is the antenna-weighted bidimensional Fourier transform of the surface brightness distribution

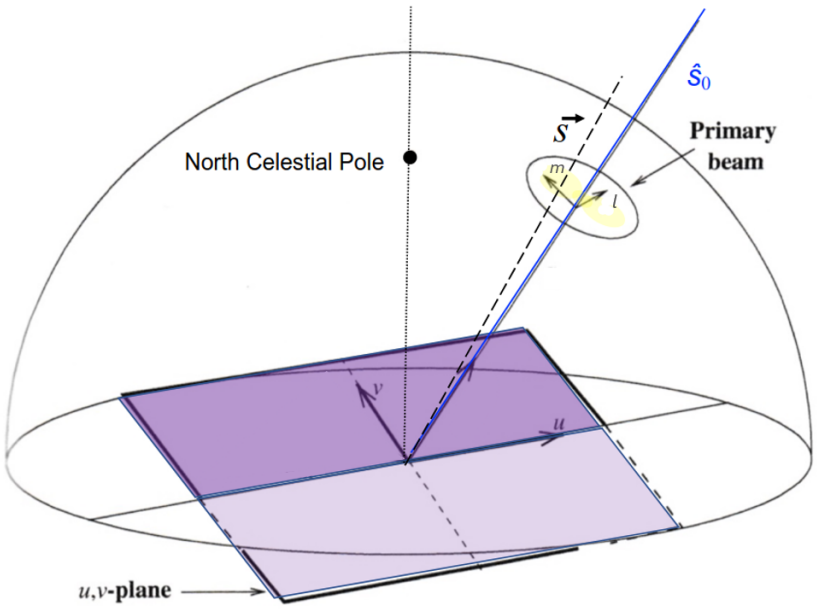

Figure 3.4: *Representation of the (u,v) plane and the (l,m) plane. From* James J. Condon, Scott M. Ransom, 2016 [54].

$I(l,m)$. Vice versa $I(l,m)A_e(l,m)$ is the inverse Fourier transform of $\mathcal{V}(u,v)$:

$$\mathcal{V}(u,v) \simeq \int_m \int_l I(l,m)A_e(l,m) \cdot e^{-2\pi i(ul+vm)} dldm \tag{3.16}$$

$$A_e(l,m)I(l,m) \simeq \int_v \int_u \mathcal{V}(u,v) \cdot e^{2\pi i(ul+vm)} dudv \tag{3.17}$$

The projection of each baseline corresponds to a point (and its complex conjugate) in the (u,v) plane, and the ensemble of these points it's called ***u,v* coverage**, or **sampling function**. The sampling function can be proven to be the Fourier transform of the synthesized beam. While an ideal telescope has a complete coverage of the (u,v) plane, in reality this is impossible given that we would need a uniform distribution of infinite antennas.
The result of the inverse Fourier transform of the visibility will therefore be the antenna-weighted source brightness distribution convolved with the synthesized beam. We will refer to this as the **dirty map**. This is because the quantity we measure through our instrument is not the intrinsic visibility of the source, but the product of the visibility and the sampling function (remember that a product in the Fourier space is transformed in a convolution in the coordinate space). We will refer to this as the **sampled visibility**. To reconstruct the true brightness distribution we thus need to face a deconvolution process.

3.1.5 The Atacama Large Millimeter/Submillimeter Array

Located approximately 23° south latitude and 67° longitude, the Atacama Large Millimeter/Submillimetetr Array (ALMA, figure 3.5) stands on top of the Cerro Chajnantor in the Atacama desert, at 5044 m altitude from the sea level. This desert is known to be one of the most arid area of the world and thus is a very suitable place for astronomic observations.

ALMA has 66 antennas: fifty-four 12-meter diameter antennas and twelve 7-meter diameter antennas. Fifty of the 12-meter antennas can be hauled around on the backs of transporters in order to form arrays that are either very tightly packed configurations only 150 meters across or spread out to 16 kilometers across, and they form the so called **12-m array**. More extended arrays give ALMA a zoom lens for finer details, while more compact arrays give better sensitivity for larger objects. In addition to this movable array of 12-m antennas there is the **Atacama Compact Array** (ACA), made of twelve 7-m antennas and four 12-m antennas that images large-scale structures, which mostly stay in a fixed configuration.
ALMA is able to observe the sky in a range of frequencies that goes from 31 GHz to 950 GHz in 10 different operational bands, with an angular resolution that can reach up to 0.004 arcsec in its most extended configuration.

Figure 3.5: *The Atacama Large Millimeter/Submillimeter Array. Photo credits:* L. Calçada (ESO).

Despite being located in one of the most suited sites for mm/submm interferometry, ALMA observations are still affected by the physics of the troposphere, and are thus weather dependent. Most of the corruption effects acting on our data are due to precipitable water vapors (PWV), which introduce in our observations both **absorption** and **phase fluctuations**. PWV is an index defined as the depth of liquid water that would result if all the water vapor in the atmospheric column is condensed and precipitated, and has therefore the dimensionality of a length.
Tropospheric absorption depends on the observed frequency and on altitude: located at 5000 meters above sea level, the ALMA observatory experiences significantly lower absorption due to PWV than an observatory located at lower altitudes. In figure 3.6 is reported the atmospheric transmission at the ALMA site as a function of frequency and PWV.
The phenomenon of phase fluctuations is introduced by the atmospheric turbulence (*Coulman, 1985 [17]*), which can cause local variation in the PWV. The phase change experienced by an electromagnetic wave can be related to PWV through the relation:

$$\phi_e \simeq \frac{12.6\pi}{\lambda} \cdot \mathrm{PWV} \tag{3.18}$$

and, according to Kolmogorov turbulence theory, the atmospheric turbulence generates a phase rms (root mean squared) given by:

$$\phi_{rms} = \frac{Kb^{\alpha}}{\lambda} \tag{3.19}$$

where K is a constant that depends on the telescope site, b is the baseline length and α goes from 1/3 up to 5/3. At the same wavelength, then, the more distant two antennas are, the higher will be the phase noise in their measured signal. Phase shifts are corrected using water vapors radiometers, one in each antenna: these instruments observe in four channels flanking the peak of the 183 GHz water line, acquiring data every second. The observed PWV is then compared to models and the correction on phase is computed using equation 3.18.

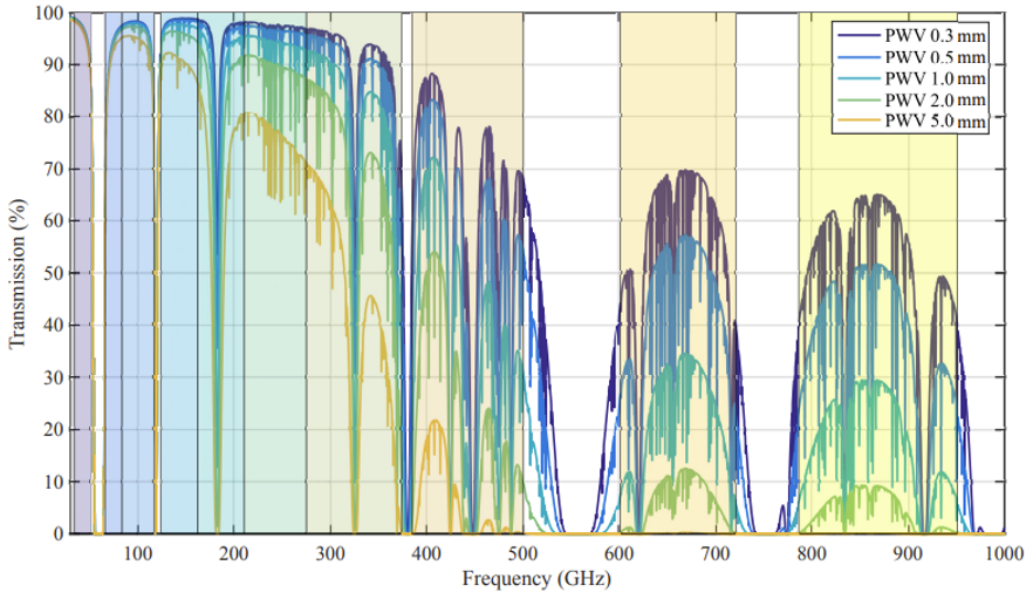

Figure 3.6: *Atmospheric transmission percentage with respect to the frequency. The different color bands show the different operational bands, while the color curves represent different PWV values. From* R. Warmels et al., 2018 [101].

Another effect that we have to take into consideration is the **system noise temperature**. It is a theoretical value defined as the equivalent temperature of the power per unit bandwidth measured by an amplitude calibration device (ACD) mounted on the antenna. For an interferometer, the system noise temperature can be written as:

$$T_{sys} \simeq T_A + T_{atm}(1 - e^{-\tau}) + T_{rx} \tag{3.20}$$

where T_A is called antenna temperature and is associated to the component of the power resulting from the observed cosmic source, T_{atm} is associated to the power coming from atmospheric emission, and T_{rx} to the power generated by the electronics itself. What we are interested in is T_A, this means that the ACD has to correct the T_{sys} accounting for the noise power introduced by atmospheric and electronic emission.

3.2 The sample

The data analyzed in this work are part of the ALMA observational projects 2019.2.00053.S and 2021.2.00064.S (PI: Roberto Decarli). They consist of the observations of **11 very bright type 1 radio quiet QSOs**, carried out in **ALMA band 8** at **redshift between 6 and 7** with ACA. Within the frequency span of band 8, observations have been tuned to $\sim 400\ GHz$, where the atmospheric transparency is most favorable.
The sample was selected so that all the QSOs:

- have been already observed in [CII] and underlying 158 μm continuum.
- have $S_\lambda(158\ \mu m, \text{rest}) > 1.5\ mJy$.
- have not already been detected in ALMA band 8 nor in *Herschel*/SPIRE bands before.
- are visible from the ALMA site.

The complete list of the sources, as well as their coordinates and spectroscopic redshifts is reported in table 3.1.

ID	*RA*	*Dec*	$z_{[CII]}$	*Ref.*
AJ025-33	01:42:43.727	-33:27:45.470	6.3373	[96]
J0305-3150	03:05:16.916	-31:50:55.900	6.6139	[96]
J0439+1634	04:39:47.110	+16:34:15.820	6.5188	[104]
J2318-3029	23:18:33.100	-30:29:33.370	6.1456	[96]
J2348–3054	23:48:33.334	-30:54:10.240	6.9007	[96]
P007+04	00:28:06.560	+04:57:25.680	6.0015	[96]
P009–10	00:38:56.522	-10:25:53.900	6.0040	[96]
PJ036+03	02:26:01.876	+03:02:59.390	6.5405	[96]
PJ083+11	05:35:20.900	+11:50:53.600	6.3401	[2]
PJ158-14	10:34:46.509	-14:25:15.855	6.0681	[35]
PJ231–20	15:26:37.841	-20:50:00.660	6.5865	[70]

Table 3.1: *List of the ID, right ascension, declination, redshift and redshift references for all the QSOs analyzed in this work. Ref.:* Andika et al., 2020 [2], Eilers et al., 2020 [35], Pensabene et al., 2021 [70], Venemans et al., 2020 [96], Yang et al., 2019 [104].

At these redshifts, observations at $\sim 400\ GHz$ sample the rest-frame wavelength < 100 μm, hence they provide solid constraints on the peak wavelength of the dust thermal emission. This translates in reliable estimates of the dust temperature, and thus allows us to precisely pin down the energetic of its emission (as $L_{IR} \propto T_d^{4+\beta}$ in the optically thin limit, see subsection 2.1.2) and the associated star formation rates.

3.3 Data reduction

In this section we explain how the dataset has been treated. The data analysis has been executed via the Common Astronomy Software Application (CASA, v. 6.2.1-7).

3.3.1 Calibration

Data calibration is needed because visibilities measured by the interferometer are corrupted by a sequence of multiplicative factors due the atmosphere, antennas, electronics, correlator, and downstream signal processing effects. This can all be contained in the equation:

$$\mathcal{V}^{ij}_{obs} = G^{ij}(\nu, t) \cdot \mathcal{V}^{ij}_{true}, \tag{3.21}$$

where $\mathcal{V}^{ij}_{obs}$ represents the observed visibility as sampled by a pair of antenna i and j, $\mathcal{V}^{ij}_{true}$ is the intrinsic visibility, and every corrupting factor is contained in the complex gains' matrix G^{ij}.
The calibration process consists in determining the G^{ij} matrix: this is made up of many factors, one of which - the tropospheric distortion explained in subsection 3.1.5 - can be corrected a priori thanks to the instruments mounted on the antennas. The other effects require the observation of special calibrators in order to be corrected.

To calibrate the raw visibilities, we exploited ALMA Science Pipeline (*ALMA Pipeline Team, 2021 [90]*). The pipeline operates on a completed dataset, called **Member Observing Unit Set** (MOUS), that result from completing a **Scheduling Block** (SB). Each SB can be composed of multiple **Execution Blocks** (EB), self-consistent sets of observations that also include all of the observations on calibrators. The outputs of the pipeline are the calibrated sampled visibilities, or **Measurement Sets** (MS, one for each EB), and the imaging products (*FITS* images). However, to better investigate the data, the imaging is performed again by hand using the CASA task *tclean*, and the procedure is explained in the following subsection.

3.3.2 Imaging

To image the calibrated datasets we have to deconvolve the source brightness distribution from the synthesized beam. We can start from the inverse Fourier transform of the calibrated sampled visibilities, (i.e. the dirty map, which is in fact the convolution of the two aforementioned quantities). From there we can reconstruct the brightness distribution, knowing the synthesized beam (which is the inverse Fourier Transform of the sampling function).
The *tclean* task in CASA converts the calibrated MS in an output image file that contains the true brightness distribution of the source and can therefore be used for scientific purposes. Its functioning is based on the Högbom deconvolution algorithm (*Högbom, 1974 [49]*), which proceeds as follows:

1. Computes the dirty map as the anti Fourier transform of the calibrated sampled visibilities, and the synthesized beam as the the anti Fourier transform of the sampling function

2. Searches in the dirty map for the position and intensity of the peak I_0, then it subtracts from the whole image a synthesized beam pattern centered in this

position and normalized so that its maximum value is equal to γI_0, where γ is called loop gain factor. We will refer to the resulting image as the **residual image**

3. Adds the subtracted quantity to a new image (initially empty) that is called **model image**

4. Iteratively repeats steps 2 and 3 starting from the residual image, each time adding the subtracted value to the model image. It will stop the iterations when the current value of I_0 reaches a given threshold (usually a few times the rms of the residual image)

5. Convolves the model image with an idealized **clean beam** (usually an elliptical Gaussian fitted to the main lobe of the synthesized beam). The resulting image is called **clean image**

6. Adds the residuals to the clean image

One thing that has to be considered when running the *tclean* task in CASA is the weighting of the visibilities. As part of the imaging process, in fact, visibilities can be weighted in different ways to produce the dirty map. There are three main weighting schemes for interferometric data: natural, uniform, and Briggs weighting.

- Natural weighting: data are gridded into (u, v) cells for imaging, with weights given by $W(u, v) = 1/\sigma^2$, where σ is the noise variance in each visibility. This results in a higher imaging weight for higher (u, v) density, so this weighting scheme typically favours shorter baselines.

- Uniform weighting: data are first gridded to a number of cells in the (u, v) plane, and afterwards the (u, v) cells are re-weighted to have uniform imaging weights, given by $W(u, v) = 1/\delta_s(u, v)$ where $\delta_s(u, v)$ is the the density of (u, v) points in a symmetric region of the (u, v) plane. This scheme favours longer baselines and produces an image with higher resolution, but with increased noise with respect to the natural weighting image.

- Briggs weighting: this scheme is a combination of uniform and natural weighting, with a *robust* parameter that allows for continuous variation between the two.

The *tclean* task allows for two modes of the imaging process:

- mfs (multi frequency synthesis): this mode takes all the visibilities in the spectral coverage of the observation and combines them to obtain a single clean image of the target.

- cube: this mode generates 3 dimensional clean images of the target, with two axis being right ascension and declination and the third axis being the frequency. In other words it creates a collection of clean images, each one realized from the visibilities coming from a subset of the spectral coverage of the observation. This frequency subset is called **channel** of the cube.

The cube mode is useful as it can help us identify the presence of spectral lines. In fact, if an emission line is present, imaging the visibilities with channel width of $\Delta v \simeq 50$ km/s can result in a cube where an excess of flux is detected in some of its channels,

if compared to the flux of adjacent ones. We can express the channel width in velocity according to:

$$\Delta v = \frac{\Delta \nu}{\nu_{cent}} c \tag{3.22}$$

where $\Delta\nu$ is the channel width in frequency and ν_{cent} the central frequency of the spectral coverage. Thus, for typical line widths of 300 km/s, the line emission would be spread over ~ 6 channels.

In this work we are interested in the continuum emission, therefore the presence of an emission line could contaminate our flux estimates. We therefore imaged the 11 sources in **cube mode** using **natural weighting**, a 3σ **cleaning threshold** per channel and imposing **channel widths of 50 km/s**. The weighting scheme was chosen in order to minimize the noise, as we are not interested in having spatially resolved observations (which are however not possible to achieve, given that the data are obtained using the ACA and the expected size of these object are lower than 1", eg. *Walter et al., 2022 [98]*). In the end, no line emission was detected in the resulting cubes.
After checking for the presence of emission lines we can image the continuum emission. This was done by running again the *tclean* task in **mfs mode**, using the same parameter used in the cube case (**natural weighting** and a 3σ **cleaning threshold**). This allowed us to obtain the continuum clean maps for all the 11 sources of the sample, centered at a frequency of $407 GHz$, as reported in figure 3.7. In table 3.2 we list the clean beam size and the rms of each continuum map.
The dust continuum emission was detected for all the sources with a **confidence level of at least** 9σ.

ID	*Clean Beam* $[arcsec]$	*rms* $[mJy/beam]$
AJ025-33	1.96 × 1.62	0.16
J0305-3150	4.44 × 2.75	0.95
J0439+1634	2.53 × 1.38	1.0
J2318-3029	3.96 × 2.62	0.65
J2348–3054	4.31 × 2.59	0.44
P007+04	1.91 × 1.51	0.19
P009–10	4.14 × 2.65	0.80
PJ036+03	1.92 × 1.46	0.24
PJ083+11	2.91 × 1.35	0.58
PJ158-14	1.80 × 1.49	0.45
PJ231–20	4.34 × 2.92	0.92

Table 3.2: *Clean beam sizes and rms obtained from the imaging of all the sources in the sample. The continuum maps are reported in figure 3.7.*

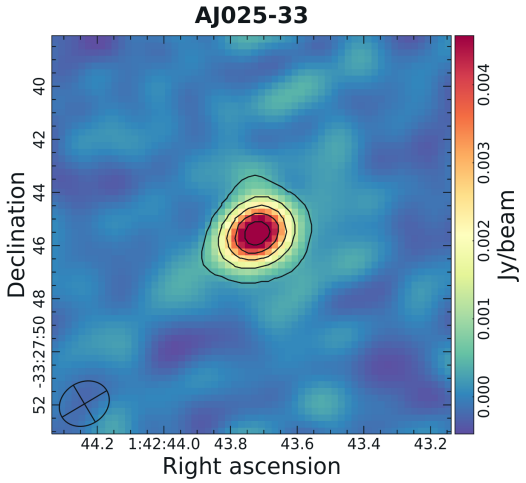

(a) *407 GHz dust continuum map of QSO AJ025-33 (contours at 3, 9, 15, 21 and 27σ).*

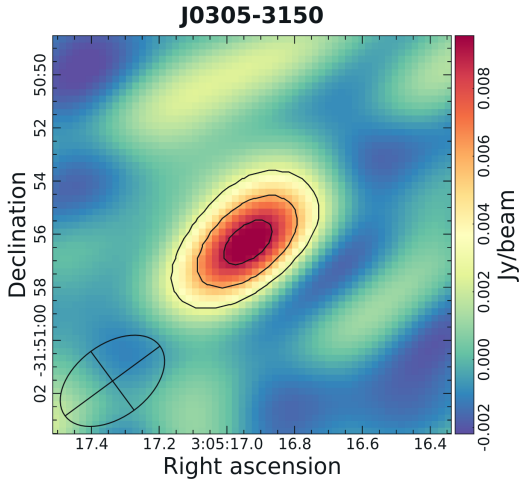

(b) *407 GHz dust continuum map of QSO J0305-3150 (contours at 3, 6 and 9σ).*

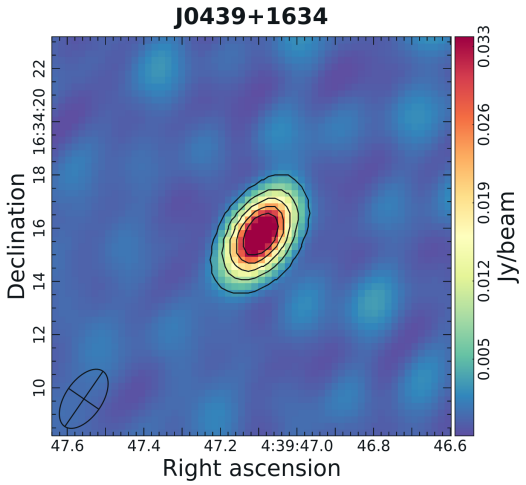

(c) *407 GHz dust continuum map of QSO J0439+1634 (contours at 3, 9, 15, 21 and 27σ).*

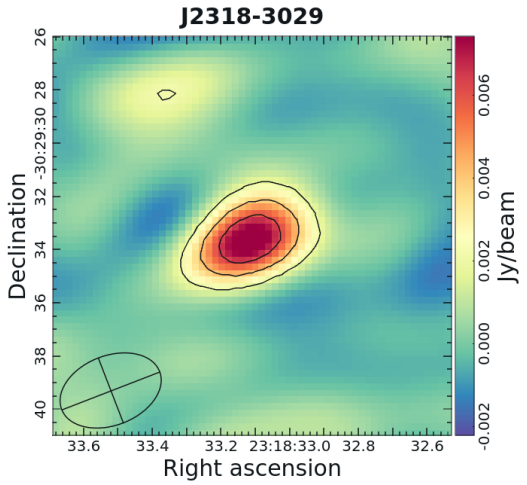

(d) *407 GHz dust continuum map of QSO J2318-3029 (contours at 3, 6 and 9σ).*

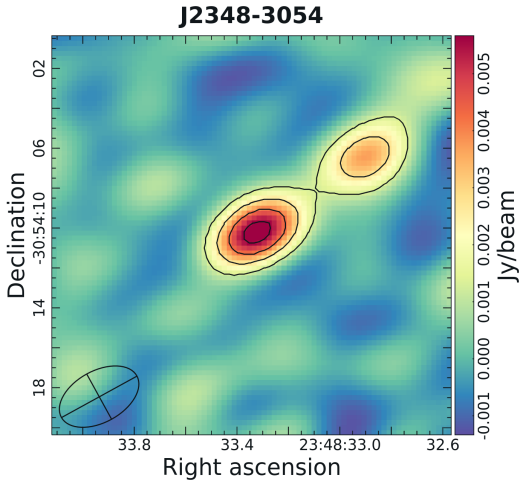

(e) *407 GHz dust continuum map of QSO J2348-3054 (contours at 3, 6, 9 and 12σ).*

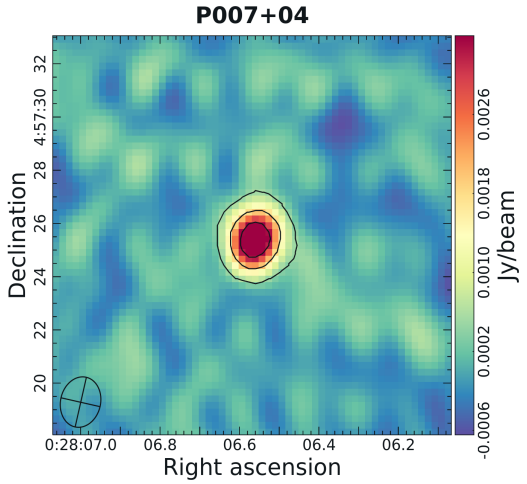

(f) *407 GHz dust continuum map of QSO P007+04 (contours at 3, 9 and 15σ).*

Figure 3.7: *Dust continuum maps for all the sources in this work. The clean beam is reported in the bottom left corner.*

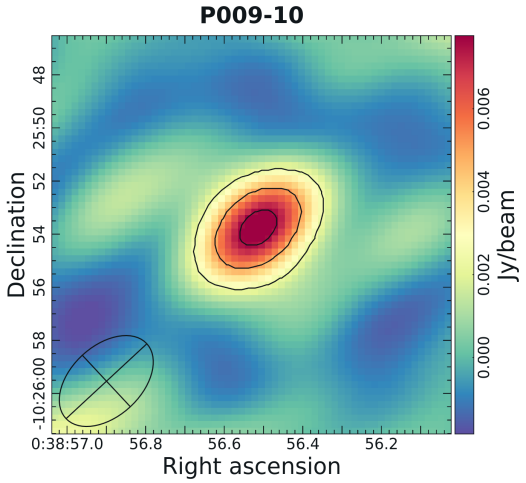

(g) *407 GHz dust continuum map of QSO P009-10 (contours at 3, 6 and 9σ).*

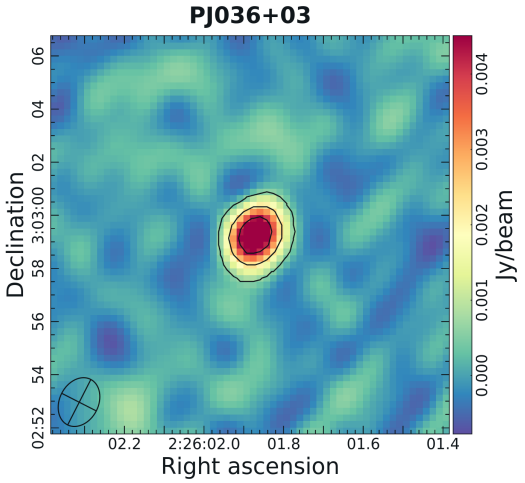

(h) *407 GHz dust continuum map of QSO PJ036+03 (contours at 3, 9 and 15σ).*

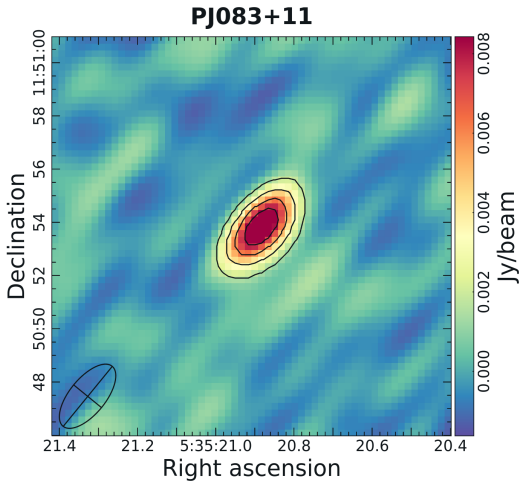

(i) *407 GHz dust continuum map of QSO PJ083+11 (contours at 3, 6, 9 and 12σ).*

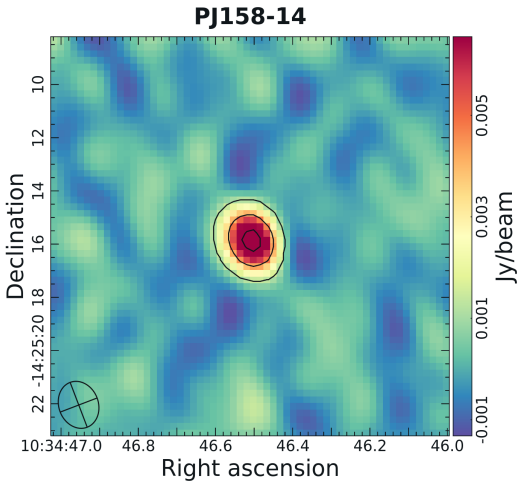

(j) *407 GHz dust continuum map of QSO PJ158-14 (contours at 3, 9 and 15σ).*

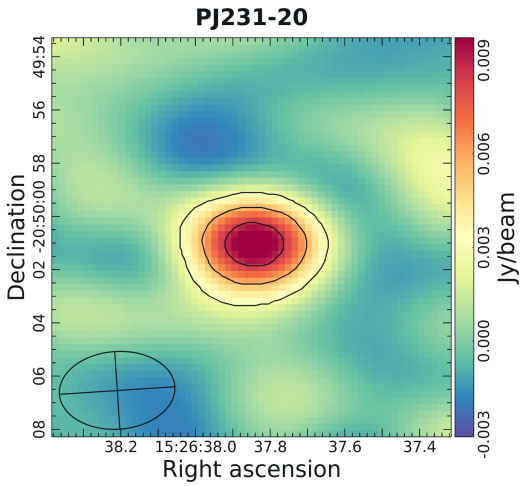

(k) *407 GHz dust continuum map of QSO PJ231-20 (contours at 3, 6 and 9σ).*

Figure 3.7: *Continued from previous page.*

3.4 Fitting the dust graybody emission

In this section we explain the methods adopted to perform the fitting of the dust emission. We explored the parameter space using a Markov chain Monte Carlo (MCMC) algorithm implemented in the EMCEE package (*Foreman-Mackey et al., 2013 [41]*) for *Python*. In this work, we adopt the ΛCDM cosmology from *Planck Collaboration, 2020 [71]*: $H_0 = 67.4$ km $\cdot$ s^{-1} $\cdot$ Mpc^{-1}, $\Omega_m = 0.315$, and $\Omega_\Lambda = 0.685$.

3.4.1 Available far infrared data

Having now the dust continuum maps of all the eleven sources, we exploit the task *imfit* in CASA to provide estimates of the fluxes: this task is used to fit a two dimensional Gaussian to the source in the image. It will give as output the image component size (i.e. the FWHM of both minor and major axis) convolved with the clean beam and, if the source is spatially resolved, also the image component size deconvolved from the clean beam. Most importantly, from this task we get also the flux integrated over the fitted Gaussian (in mJy) and the value of its peak (in mJy/beam), with the associated errors. As already explained, our observations are not spatially resolved, therefore we are not able to provide estimates of the true sizes of these objects from these data only.

We carry out a spatially unresolved analysis, assuming that the emission arises from a single dust component described by equations 2.36, 2.37 and 2.38. This assumption is an approximation, as it ignores the potential presence of gradients in dust temperature. In this set of three equations we will fit the **dust mass** M_d, the **dust emissivity index** β and the **dust temperature** T_d, which are the physical quantities that we aim to constrain.
To perform the analysis, we collected additional dust continuum flux measurements at various frequencies for the eleven sources in our sample. These data were gathered from both the specific literature and the observations available in the ALMA archive (https://almascience.eso.org/aq/), which we reduced and analyzed.
Additionally, an estimate of the angular size of the object is also necessary when fitting dust emission under optically thick assumption (i.e. $\tau \ll 1$), however this measurement can carry sensitive uncertainties as it may introduce a wavelength dependence when a gradient in dust temperature is present in the object (see, e.g., *Rivera et al., 2018 [75]*). Here we adopt as angular size of our sources the elliptic area defined by the image components size that published works retrieve from the $imfit$ task in the case of spatially resolved observations.
Table 3.3 lists all the observational data collected for the eleven sources used in fitting the graybody emission.

For **J0305-3150**, **J2348-3054** and **PJ036+03** it has been possible to find at least other two flux measurements at different wavelengths, as well as an estimate of the size of the emitting region. These data did not require additional elaboration and have been directly used to fit the far infrared SED of the QSOs.

The source **J0439+1634** shows strong lensing effects, therefore we corrected all the observed fluxes for the galaxy-averaged magnification factor $\mu = 4.9$ reported in *Yang et al., 2019 [104]*. This effect may bias the estimate of the dust temperature towards higher values, but we will discuss the details in the next chapter. As for the size, we

used as reference *Yue et al., 2021 [105]*. This work did not report the $FWHM$ of the fitted Gaussian, but only the effective radius $R_e = 0.131$ arcsec. We therefore computed the former as:

$$FWHM = 2R_e \left(\frac{ln2}{k} \right)^n \tag{3.23}$$

where $n = 1.58$ is the Sersic index and $k = 1.9992n - 0.3271$. For these value we obtain a $FWHM = 0.10$ arcsec.

For **AJ025-33** and **J2318-3029** there are no measurement published that constrain the flux of the Rayleigh-Jeans tail of the emission. However, a value has been provided by R. Decarli and A. E. Borea, who reduced and analyzed the band 3 data from the ALMA project 2019.1.00147.S (PI: Roberto Decarli).

A flux measurement at lower frequencies is lacking also for **PJ083+11**. In this case we decided to download, reduce and analyze band 4 data from the ALMA project 2021.2.00151.S (PI: Chiara Feruglio). The procedure adopted is analogous to the one described in the previous subsections. Regarding the size, the paper used as reference (*Andika et al., 2020 [2]*) only reported the physical values of the $FWHM$ of the fitted Gaussian, 2.3 × 1.7 Kpc. To convert it to an angular value we adopted the cosmology of *Planck Collaboration, 2020 [71]*, obtaining 0.40 × 0.30 arcsec.

As for the source **P231-20**, it was found to have a companion galaxy located ∼2 arcsec south to the QSO (*Decarli et al., 2017 [24]*). The issue with our band 8 observation is that, having a beam size of 4.34 × 2.92 arcsec, it lacks the resolving power to disentangle the two. Here we measure a flux of 9.6 ± 1.4 mJy, but this value is contaminated by the companion emission. In the paper we used as reference for the other flux measurements (*Pensabene et al., 2021 [70]*) however, the two sources are resolved. Luckily, we had the possibility to analyze a very high resolution band 8 image of this source (courtesy of R. Decarli), obtained from the ALMA project 2022.1.00321.S (PI: Roberto Decarli), in which is possible to disentangle the quasar and the companion galaxy. Here the ratio between the flux of the companion galaxy over the total flux of the QSO's and companion's combined has been determined to be equal to 0.78. We adopt this fraction to correct the measured flux of our band 8 unresolved observation and get a companion-corrected value of 7.5 ± 1.1 mJy for the QSO. As for the size of the emitting region, it has been estimated exploiting the band 8 high resolution image, given that its value is not reported in the article we used as reference. We obtain a size of 0.26 × 0.19 arcsec.

Finally, for the sources **P007+04**, **P009-10** and **PJ158-14**, the Rayleigh-Jeans tail of the emission remains unconstrained, and this will prevent us from reliably fitting the SED of the three sources. To tackle this problematic, we wrote a proposal for the *Northen Extended Millimeter Array* (NOEMA) asking for a total telescope time of 15h. The project is aimed at measuring the flux of the continuum emission in these three objects at the observed frequency of ∼ 150 GHz. The proposal has been accepted and observations are currently being carried on (ID: S24CH, PIs: Michele Costa, Leindert Boogaard).

3.4.2 The fitting algorithm

In order to fit the dust continuum emission we operate, for each source, the following steps:

1. From the observational data listed in table 3.3 we first compute the physical length of both minor and major axis of the fitted 2D Gaussian adopting the cosmology of *Planck Collaboration, 2020 [71]*, and then we get the area of the emitting region A_g as:
$$A_g = \pi \frac{a \cdot b}{4 \cdot ln2} \tag{3.24}$$
where a and b are the physical lengths of minor and major axis respectively.

2. We assume a power law behaviour of the opacity (see subsection 2.1.3) with $k_0 = 0.45$ cm^2/gr and $\nu_0 = 250$ GHz (*Carniani et al., 2019 [13]*).

3. We account for the effect of the interaction of dust with the CMB: at high-redshift the photons of the Wien tail of the CMB emission can interact with the dust grains and act as an additional source of heating. To correct for this effect we follow *da Cunha et al., 2013 [18]*:
$$T_d(z) = \left(T_d^{4+\beta} + T_0^{4+\beta}\left[(1+z)^{4+\beta} - 1\right]\right)^{\frac{1}{4+\beta}} \tag{3.25}$$
where $T_0 = 2.73$ K is the CMB temperature at $z = 0$, $T_d(z)$ the temperature of the dust at a given redshift, and T_d the intrinsic temperature of the dust at the net effect of the heating provided by the CMB. This step allows the comparison between dust temperature in objects at different redshifts.

4. We are therefore left with only three free parameters in the set of equations 2.36, 2.37 and 2.38: T_d, M_d and β. We explore the 3D parameter space using a Markov chain Monte Carlo (MCMC) algorithm implemented in the EMCEE package. We assume uniform priors probability distribution in the ranges $T_d \in [1, 150]$ K, $log(M_d/M_\odot) \in [6, 9]$, and $\beta \in [0.5, 3.5]$, and run the algorithm using 30 chains, 5000 steps and a burn-in phase of 1000 steps.

As previously mentioned, the fit converged to a robust result only for eight out for the eleven sources. The results will be discussed in the next chapter.

AJ025-33		
Obs. frequency $[GHz]$	*Flux* $[mJy]$	*Ref.*
407	6.8 ± 0.3	This work
259	2.49 ± 0.11	[96]
110	0.089 ± 0.016	Decarli et al., in prep.
Size $[arcsec]$	*Ref.*	
0.27 × 0.19	[96]	

J0305-3150		
Obs. frequency $[GHz]$	*Flux* $[mJy]$	*Ref.*
407	10.4 ± 1.5	This work
250	5.34 ± 0.19	[96]
99	0.23 ± 0.03	[95]
Size $[arcsec]$	*Ref.*	
0.32 × 0.28	[96]	

Table 3.3: *Flux and size measurements that were used to perform the SED fitting for all eleven the sources in our sample. For the specific details on each object see subsection 3.4.1.*
[a] *This source is strongly lensed.*
[b] *The size is computed from the reported effective radius.*
[c] *Obtained from the reduction and analysis of ALMA project 2021.2.00151.S (PI: Chiara Feruglio).*
[d] *The angular size is computed from the reported extension in Kpc.*
[e] *The flux had to be corrected for the presence of an unresolved companion.*
[f] *The size was estimated from the reduction and analysis of ALMA project 2022.1.00321.S (PI: Roberto Decarli).*
Ref: Andika et al., 2020 [2], Ansarinejad et al., 2022 [3], Butler et al., 2023 [12], Decarli et al., 2022 [23], Pensabene et al., 2022 [70], Tripodi et al., 2024 [93], Venemans et al., 2017 [95], Venemans et al., 2020 [96], Yang et al., 2019 [104], Yue et al., 2021 [105].

J0439+1634		
Obs. frequency $[GHz]$	$Flux^{(a)}$ $[mJy]$	*Ref.*
407	45.4 ± 1.4	This work
353	26.2 ± 1.7	[104]
271	16.9 ± 0.1	[104]
255	15.5 ± 0.1	[104]
245	16.0 ± 0.1	[105]
239	14.0 ± 0.1	[104]
155	3.50 ± 0.04	[104]
139	2.70 ± 0.03	[104]
109	1.60 ± 0.03	[104]
93	1.30 ± 0.03	[104]
Size $[arcsec]$	*Ref.*	
$0.10 \times 0.10^{(b)}$	[105]	
J2318-3029		
Obs. frequency $[GHz]$	*Flux* $[mJy]$	*Ref.*
407	6.9 ± 1.1	This work
266	3.11 ± 0.07	[96]
113	0.26 ± 0.03	Decarli et al., in prep.
Size $[arcsec]$	*Ref.*	
0.14×0.12	[96]	

Table 3.3: *Continued from previous page.*

J2348-3054		
Obs. frequency $[GHz]$	*Flux* $[mJy]$	*Ref.*
407	5.5 ± 0.8	This work
240	2.28 ± 0.07	[96]
95	0.118 ± 0.013	[95]
Size $[arcsec]$	*Ref.*	
0.13 × 0.07	[96]	

P007+04		
Obs. frequency $[GHz]$	*Flux* $[mJy]$	*Ref.*
407	4.8 ± 0.4	This work
271	2.33 ± 0.06	[96]
Size $[arcsec]$	*Ref.*	
0.13 × 0.11	[96]	

P009-10		
Obs. frequency $[GHz]$	*Flux* $[mJy]$	*Ref.*
407	8.6 ± 1.2	This work
271	3.7 ± 0.4	[96]
Size $[arcsec]$	*Ref.*	
0.80 × 0.35	[96]	

Table 3.3: *Continued from previous page.*

PJ036+03		
Obs. frequency $[GHz]$	*Flux* $[mJy]$	*Ref.*
671	5.6 ± 0.7	[93]
407	6.2 ± 0.4	This work
334	5.000 ± 0.002	[12]
252	2.55 ± 0.05	[96]
100	0.13 ± 0.02	[23]
Size $[arcsec]$	*Ref.*	
0.19 × 0.16	[96]	

PJ083+11		
Obs. frequency $[GHz]$	*Flux* $[mJy]$	*Ref.*
407	10.5 ± 1.0	This work
258	5.54 ± 0.16	[2]
244	5.10 ± 0.15	[2]
145	0.86 ± 0.17	This work[(c)]
Size $[arcsec]$	*Ref.*	
0.40 × 0.30[(d)]	[2]	

Table 3.3: *Continued from previous page.*

PJ158-14		
Obs. frequency $[GHz]$	*Flux* $[mJy]$	*Ref.*
407	9.6 ± 0.8	This work
261	3.21 ± 0.07	[3]
Size $[arcsec]$	*Ref.*	
0.20 × 0.14	[3]	
PJ231-20		
Obs. frequency $[GHz]$	*Flux* $[mJy]$	*Ref.*
407	7.5 ± 1.1	This work[(e)]
250	3.94 ± 0.06	[70]
242	3.46 ± 0.06	[70]
234	3.29 ± 0.05	[70]
227	2.88 ± 0.05	[70]
205	2.19 ± 0.03	[70]
193	1.91 ± 0.04	[70]
153	0.86 ± 0.03	[70]
140	0.72 ± 0.02	[70]
106	0.31 ± 0.02	[70]
94	0.22 ± 0.01	[70]
Size $[arcsec]$	*Ref.*	
0.26 × 0.19	This work[(f)]	

Table 3.3: *Continued from previous page.*

Chapter 4

Results and discussion

4.1 SED fitting results and sample analysis

In this section we will report and discuss the dust physical parameters (dust temperature T_d, dust mass M_d and emissivity index β) obtained from the SED fitting in the case of a robust convergence of the algorithm. This will also allow us to provide an estimate of the infrared luminosity L_{IR} and the associated star formation rate SFR, as well as the optical depth at the rest-frame reference frequency of 1900 GHz $\tau_{1900\,\mathrm{GHz}}$.
We then proceed with placing our results in a broader scientific context, in order to better understand the properties and the evolutionary state of the QSOs of our sample.

4.1.1 Derived infrared physical properties of the sample

As anticipated in the previous subsection, the SED of three out of the eleven sources remains poorly constrained: this is due to the fact that for P007+04, P009-10 and PJ158-14 we can provide only two flux measurements (in ALMA band 6 and in ALMA band 8, our data). Conversely, for the other 8 quasars in the sample, we are able to estimate T_d, M_d and β, as well as $\tau_{1900\,\mathrm{GHz}}$, L_{IR} and SFR. All the fitted SED (including the ones for which we have no convergence of the fit to a robust result) are reported in figure 4.5.

To determine L_{IR} we integrate the best-fit SED from 8μm to 1000μm rest-frame:

$$L_{IR} = 4\pi D_L \int_{8\ \mu m}^{1000\ \mu m} S_{BF}(\lambda) d\lambda \tag{4.1}$$

where D_L is the luminosity distance, $S_{BF}(\lambda)$ the best-fit SED, and we recall the general relation $S(\lambda) = S(\lambda_{obs})/(1+z)$. As already mentioned in the first two chapters, this quantity is a strong proxy of star formation, since it traces UV radiation emitted from young massive stars, which is absorbed by the dusty medium of star-forming regions and then re-emitted in the FIR regime. Therefore, it can be used to obtain the SFR, for which we adopt the conversion factor used in *Tripodi et al., 2024 [93]*:

$$\frac{SFR}{M_\odot \cdot yr^{-1}} = 1.496 \cdot 10^{-10} \frac{L_{IR}}{L_\odot} \tag{4.2}$$

which relies on the assumption of a Kroupa initial mass function (see *Kroupa et al., 2003 [59]*). Finally, we derive $\tau_{1900\,\mathrm{GHz}}$ from equations 2.37 and 2.38, exploiting the

values of M_d and β derived from the fit. The dust physical parameters, as well as the QSO's infrared luminosities, star formation rates and optical depths at 1900 GHz, are summarized in table 4.1.

We find a mean **temperature** of 56 ± 6 K, which is higher than the typical dust temperatures of $\sim$20 K observed in the local universe. This result supports the dust temperature evolution scenario (see, e.g., *Sommovigo et al., 2022a [88]*), which will be explored in detail in the following section. However, one important outlier is immediately noticeable: it is the QSO J0439+1634 ($T_d = 107^{+7}_{-6}$). We remind that this source is affected by strong lensing effects: the magnification factor for the central QSO derived from the *Hubble Space Telescope* (HST) imaging in *Fan et al., 2019 [38]* has shown to be much higher with respect the total magnification factor for the extended host galaxy. This means that if a second hot dust component is set by the central AGN, its weight on the total emission is enhanced and the temperature derived will be biased towards higher values. This is probably the reason for such a high value retrieved for the temperature in this source, which results in extreme L_{IR} and SFR. We will therefore not include this source in the discussion of the dust physical properties of the sample.

As for **dust masses**, we find a mean value for $log(M_d/M_\odot)$ of 7.9 ± 0.1, which is in quite good agreement with values found in *Tripodi et al., 2024 [93]* for similar sources.

Regarding dust **emissivity indexes**, we obtain a mean value of 2.3 ± 0.2. This parameter is directly linked to dust grains' physical properties (see section 2.1) and determines the behaviour of opacity as a function of the frequency. The values found in this work seem to be higher with respect the ones obtained in other studies involving similar objects (see, e.g., *Witstok et al., 2023 [102]*). For example, this last work found a mean value for β of 1.8 ± 0.3, with no significant evolution across cosmic time, suggesting that the effective dust properties do not change dramatically with redshift. Is not straightforward to assess the reason why the emissivity index of the sources analyzed in our work is on average larger with respect to these results, however we note that similar values for β are obtained also in *Bendo et al., 2023 [6]* or in *Liao et al., 2024 [61]*.

ID	T_d $[K]$	$log(M_d/M_\odot)$	β	L_{IR} $[10^{12} L_\odot]$	SFR $[M_\odot \cdot yr^{-1}]$	$\tau_{1900\,\mathrm{Ghz}}$
AJ025-33	46^{+3}_{-2}	$7.3^{+0.2}_{-0.2}$	$2.9^{+0.3}_{-0.3}$	$4.9^{+1.1}_{-0.7}$	726^{+168}_{-101}	$0.34^{+0.06}_{-0.06}$
J0305-3150	43^{+3}_{-3}	$8.1^{+0.1}_{-0.1}$	$2.6^{+0.2}_{-0.2}$	$6.9^{+2.0}_{-1.4}$	1032^{+298}_{-212}	$0.6^{+0.2}_{-0.1}$
J0439+1634	107^{+7}_{-6}	$8.11^{+0.01}_{-0.01}$	$1.37^{+0.06}_{-0.06}$	$37.2^{+9.7}_{-7.0}$	5562^{+1451}_{-1040}	$0.54^{+0.06}_{-0.06}$
J2318-3029	70^{+27}_{-12}	$8.1^{+0.1}_{-0.1}$	$1.6^{+0.4}_{-0.4}$	$11.2^{+25.0}_{-5.8}$	1683^{+3737}_{-871}	$0.6^{+0.4}_{-0.3}$
J2348-3064	77^{+7}_{-6}	$7.7^{+0.1}_{-0.1}$	$2.2^{+0.3}_{-0.2}$	$8.4^{+3.4}_{-2.4}$	1254^{+505}_{-352}	$1.2^{+0.5}_{-0.3}$
PJ036+03	53^{+1}_{-1}	$7.6^{+0.1}_{-0.1}$	$2.4^{+0.2}_{-0.2}$	$5.9^{+0.6}_{-0.5}$	880^{+84}_{-75}	$0.52^{+0.04}_{-0.04}$
PJ083+11	39^{+3}_{-2}	$8.1^{+0.3}_{-0.3}$	$2.6^{+0.4}_{-0.4}$	$5.9^{+1.4}_{-0.9}$	879^{+202}_{-130}	$0.6^{+0.1}_{-0.1}$
PJ231-20	67^{+9}_{-6}	$8.27^{+0.03}_{-0.03}$	$1.6^{+0.1}_{-0.1}$	$19.6^{+10.6}_{-5.8}$	2936^{+1582}_{-871}	$0.27^{+0.07}_{-0.06}$

Table 4.1: *Infrared physical properties derived from the SED fitting of the 8 sources for which the fitting algorithm converged.*

Concerning **infrared luminosities** and **star formation rates**, we derive a mean value of $9 \pm 2 \cdot 10^{12}$ $L_\odot$ and 1340 ± 292 $M_\odot$/yr respectively. Such high figures are justified by the construction of the sample (which selects the continuum brightest QSOs at the rest-frame frequency of 1900 GHz) and by the large values derived for the dust temperatures.

Finally, the average **optical depth** at the rest frame frequency of 1900 GHz for the sources in our sample is 0.6 ± 0.1. One important outlier is the QSO J2348-3064 ($\tau_{1900\,\mathrm{GHz}} = 1.2^{+0.5}_{-0.3}$): the exceptionally high value for this source is explained by the fact that it is extremely compact, as assessed also in *Walter et al., 2022 [98]*.
Our analysis seems to point out that the optically thin limit assumption has to be handled with care: the non negligible optical depth at 1900 GHz and the large values of the emissivity index found in our sample result in a rapid increase of the optical depth with frequency, which can often exceed unity at the frequency of our band 8 observations.

4.1.2 Sample analysis

We have now the opportunity to investigate the possible correlations that emerge from the infrared characterization of the sources in our sample.
To begin, we compare the dust masses with the star formation rates: a strong correlation between these two quantities is noticeable when we normalize them over the area of the emitting source (see figure 4.1), thus obtaining the **dust mass surface density** Σ_d and the **star formation rate surface density** Σ_{SFR}. We fit a linear relation between the logarithm of the two, obtaining:

$$\log \Sigma_{SFR} = k + m \log \Sigma_d \tag{4.3}$$

$$k = 1.0^{+0.3}_{-0.4} \qquad m = 1.1^{+0.2}_{-0.2}$$

With a Pearson coefficient $r = 0.87$ and relative p value $p = 0.01$, the trends appears to be robust and statistically significant. This relation has been interpreted (see, e.g., *Santini et al., 2014 [78], Tripodi et al., 2024 [93]*) as a consequence of the of the Kennicutt-Schmidt law, given that Σ_d can be considered proxy of the mass surface density of the neutral gas and the two quantities are linked by the gas-to-dust mass ratio.
An even stronger correlation is found when we compare again the **star formation rate surface density** Σ_{SFR} with the the **dust temperature** T_d. By fitting a linear relation between their logarithm we obtain:

$$\log \Sigma_{SFR} = s + t \log T_d \tag{4.4}$$

$$s = -4.1^{+1.0}_{-1.1} \qquad t = 4.1^{+0.7}_{-0.6}$$

with a Pearson coefficient $r = 0.99$, and relative p value $p = 1.58 \cdot 10^{-6}$. These exceptional values of the two coefficients indicate an almost perfect linear correlation, which is evident in figure 4.2. The origin of this trend can be attributed (see, e.g., *Liang et. al., 2019 [60]*) to the relation that links the temperature of the dust to the infrared luminosity, from which star formation rates are derived. Of particular interest is the slope of this relation: the value of $t = 4$ corresponds to the theoretical value we would obtain by integrating equation 2.36 in the case of $\tau(\nu) \to \infty$, and is compatible with the values we obtain in the fit. This means that the large majority of the energy emitted

by the dust is radiated at frequencies where the system is optically thick, thus making the widely assumed approximation of equation 2.40 questionable.

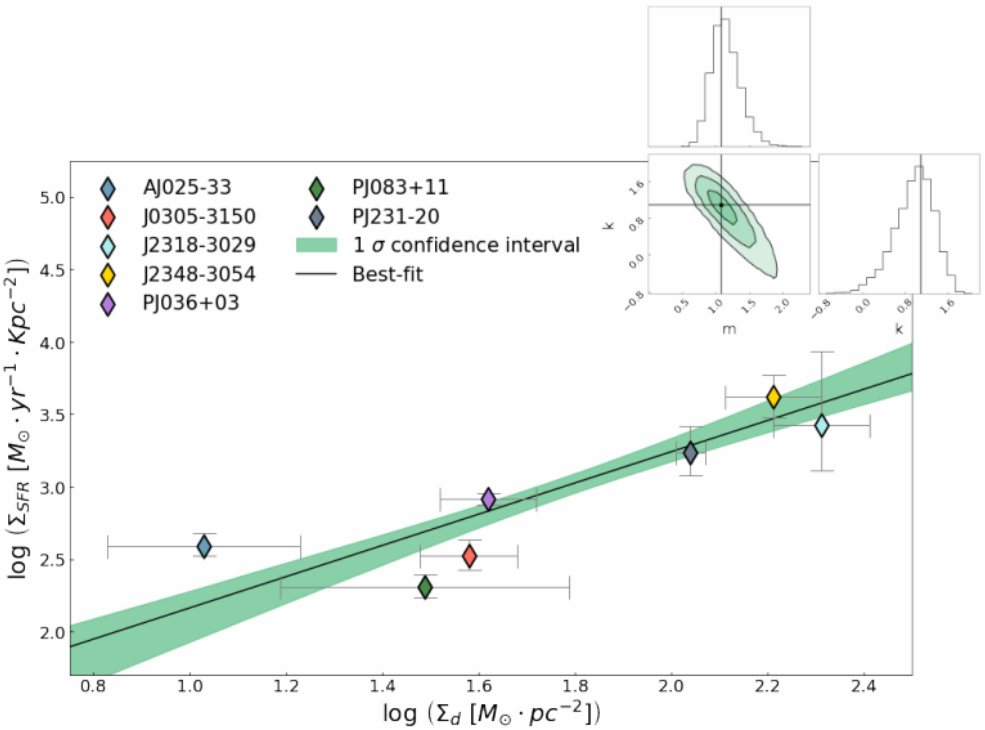

Figure 4.1: *Correlation between dust mass and SFR surface densities, with the best-fit for equation 4.3. The contour plot is reported with significance levels of 1, 2, and 3 σ.*

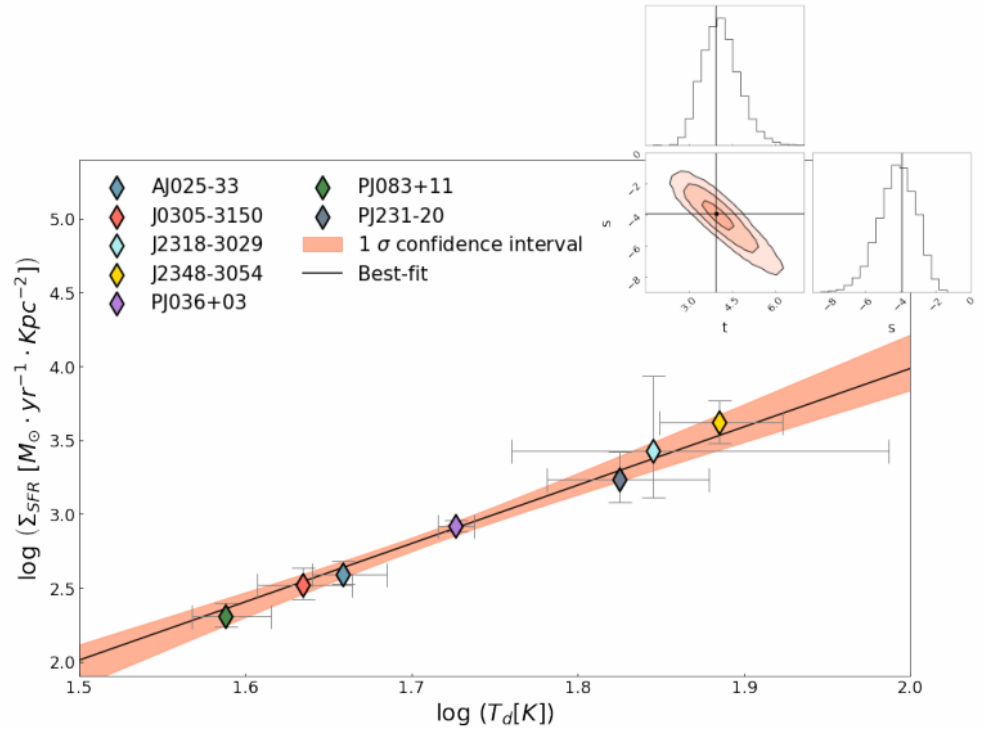

Figure 4.2: *Correlation between dust temperature and SFR surface density, with the best-fit for equation 4.4. The contour plot is reported with significance levels of 1, 2, and 3 σ.*

For these sources, we also have the possibility to investigate the nature of the **[CII] deficit** in more depth. This term refers to a decrease in the ratio between the [CII] line luminosity $L_{[\mathrm{CII}]}$ and the infrared luminosity L_{IR} as L_{IR} increases, observed in both local and high-redshift galaxies (e.g., *Diaz-Santos et al., 2017 [26]*, *Decarli et al., 2018 [25]*).
The physics behind this process is not yet fully understood, however, one possible explanation may involve a different spatial distribution of dust in star-forming regions, with dust being more concentrated near the radiation source in higher luminosity systems (*Diaz-Santos et al., 2013 [27]*). In this scenario, a greater fraction of UV photons produced by stars is absorbed by the surrounding dust, efficiently heating the dust grains while simultaneously reducing the photon flux that reaches the PDR, where the [CII] line is produced. This combination of effects can both enhance the infrared luminosity emitted by the dust and suppress the [CII] line emission.
To better investigate the role of geometry, in figure 4.3 we compare the **infrared luminosity density** (Σ_{IR}) with the **ratio between the [CII] luminosity density** (Σ_{CII}) **and $\Sigma_{\mathbf{IR}}$**. The plot reveals that the sources in our sample exhibit an anti-correlation between these two quantities, along with an increase in T_d as Σ_{IR} rises. This behaviour can be interpreted as evidence that dust geometry strongly influences T_d (see also *Liang et al., 2019 [60]*), while also contributing to the suppression of the infrared-to-[CII] luminosity ratio at high L_{IR}.

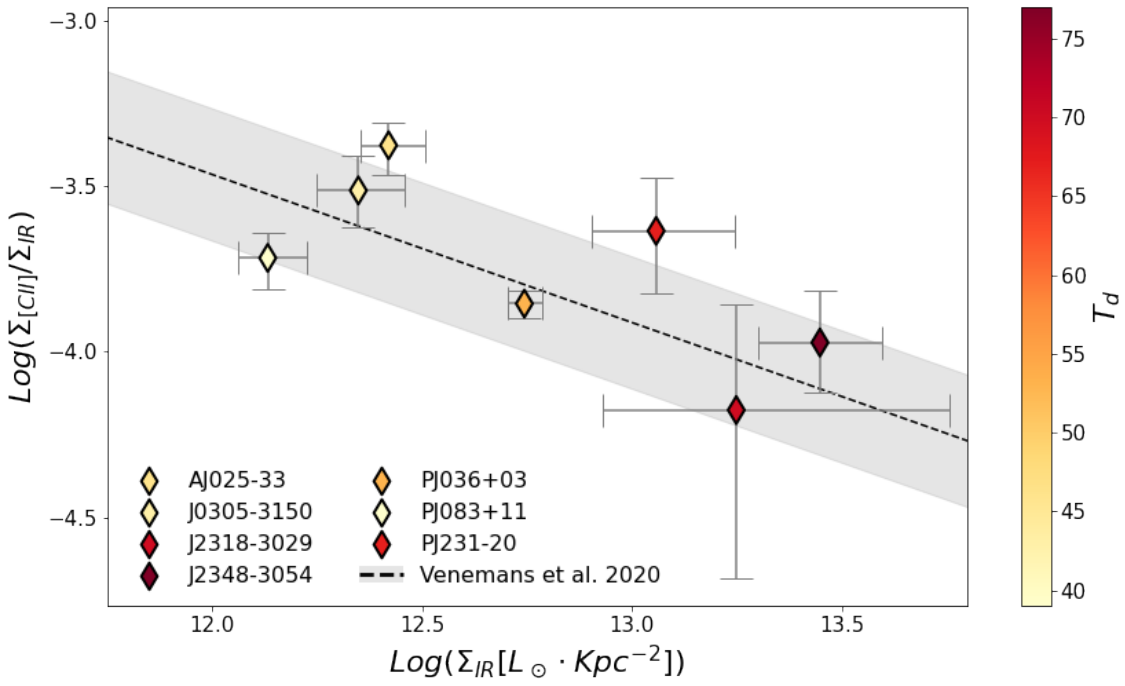

Figure 4.3: *$L_{[CII]}$ to L_{IR} density ratio reported as a function of L_{IR} density, while the color shows the dust temperatures. The [CII] line luminosity and sizes are from* Venemans et al., 2020 [96], *as well as the scaling relation reported as a dashed black line.*

In order to study the evolutionary state of the sources, we compare also the masses of the QSOs' **host galaxies** with those of their respective **supermassive black holes** (SMBH). For this kind of objects, as discussed in the introduction, it is very hard to

disentangle the optical emission coming from stars and the contribution of the bright AGN at their centre, therefore we are lacking of accurate measurements of their stellar mass contents (M_*). Fpr this reason, we exploit literature published measurements of their dynamical mass M_{dyn} obtained from the [CII] rotational curve (see subsection 1.2.4). Being this an estimate of the mass that is setting the observed rotational curve via gravitational interactions, it can be safely assumed as an upper limit for the stellar mass of the host galaxy. As for BH mass estimates, they have been obtained either via observations of the MgII 2800 Å line and the application of single epoch scaling relation, or by assuming a Eddington limited accretion (see subsection 1.2.2).
In figure 4.4 we present the results obtained for the sources in our sample that had literature available data.

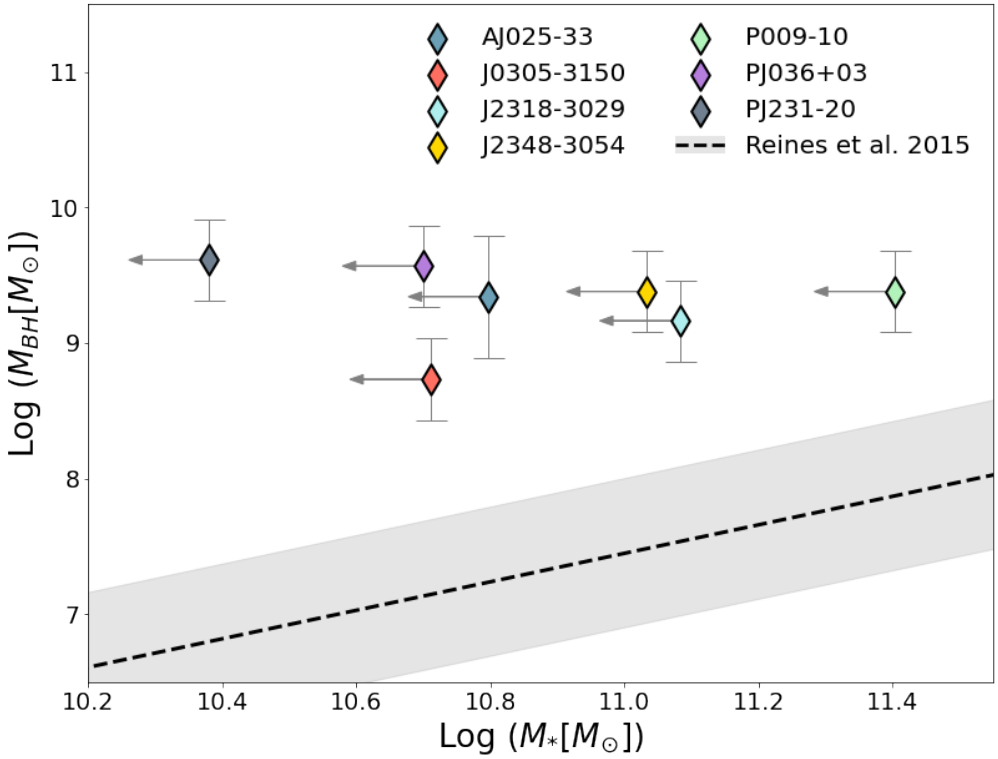

Figure 4.4: *Comparison between the black hole mass and the stellar mass (upper limit) for the QSOs in our sample that had literature available data. The dynamical masses are from* Neelman et al., 2021 [68] *and* Venemans et al., 2016 [97] *while the black hole masses are from* Neelman et al., 2021 [68] *and are displayed with a typical uncertainty of 0.3 dex if derived from MgII 2800 Å line emission (*Shen et al., 2008 [85]*) or 0.45 dex if derived assuming Eddington accretion (*Wang et al., 2013 [100]*). The scaling relation plotted is the one derived in* Reines et al., 2015 [73] *for local galaxies.*

Even under this conservative scenario, where upper limits for the stellar masses are assumed, it is clear that the central SMBH in all the QSOs analyzed is overmassive with respect to its host galaxy, if compared to local scaling relations. Similar results have been obtained in numerous papers, such as *Izumi et al., 2018 [52]* or *Pensabene et al., 2020 [69]*, and for a discussion we refer to subsection 1.3. Here, we limit to recognize that the sources analyzed in this work, despite lying significantly above the M_{BH}-M_* local relation, seem to be in a state of intense activity, both of the host galaxy and of the central SMBH, and that their interplay might shape the observed local trend.

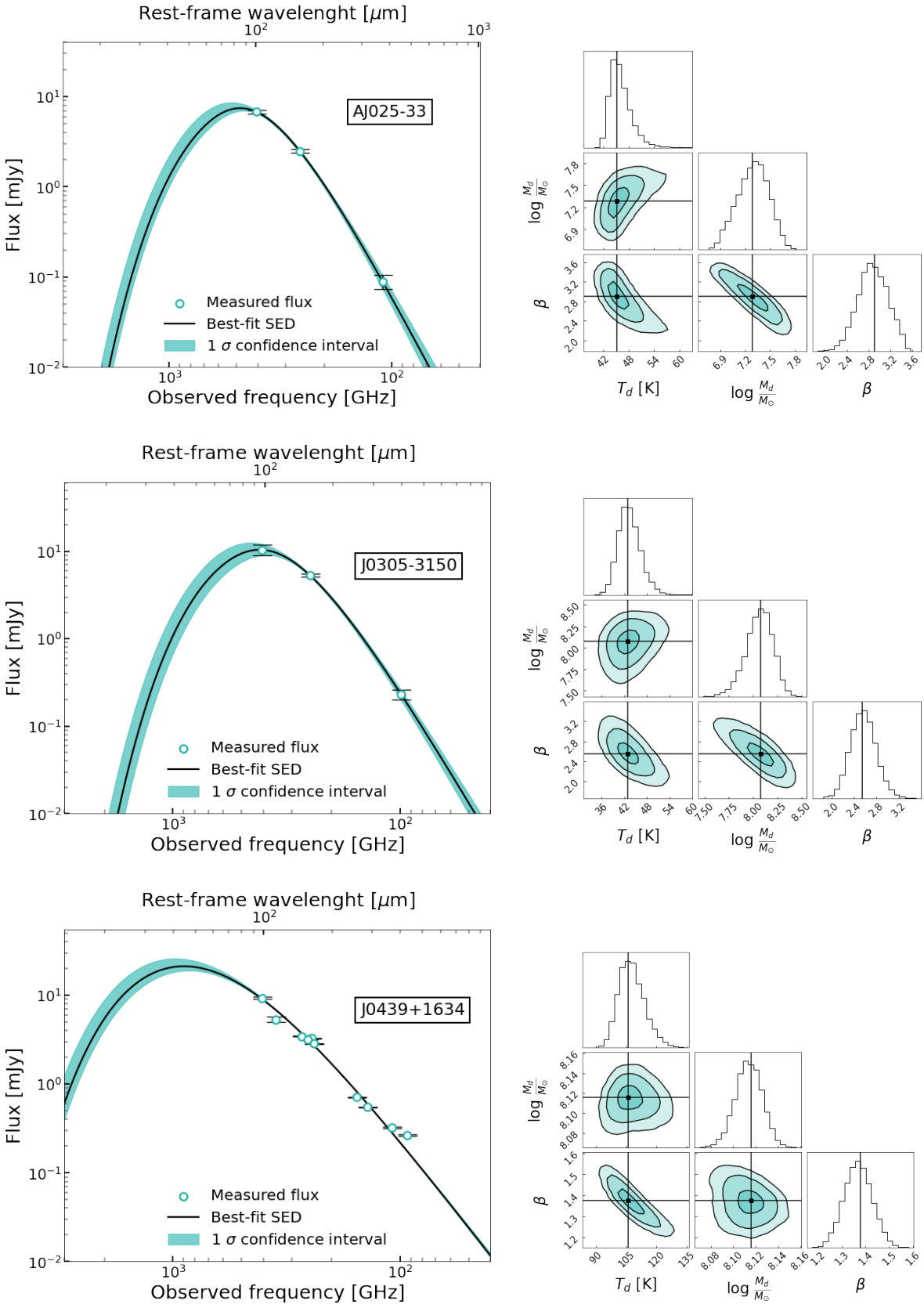

Figure 4.5: *The dust spectral energy distributions fitted in this work with the associated corner plot.* **Left panels:** *best-fit SEDs with the relative confidence intervals.* **Right panels:** *associated posterior probability distributions for T_d, M_d and β. The best fit values are displayed as solid black lines, contours are traced at 1, 2 and 3 σ.*

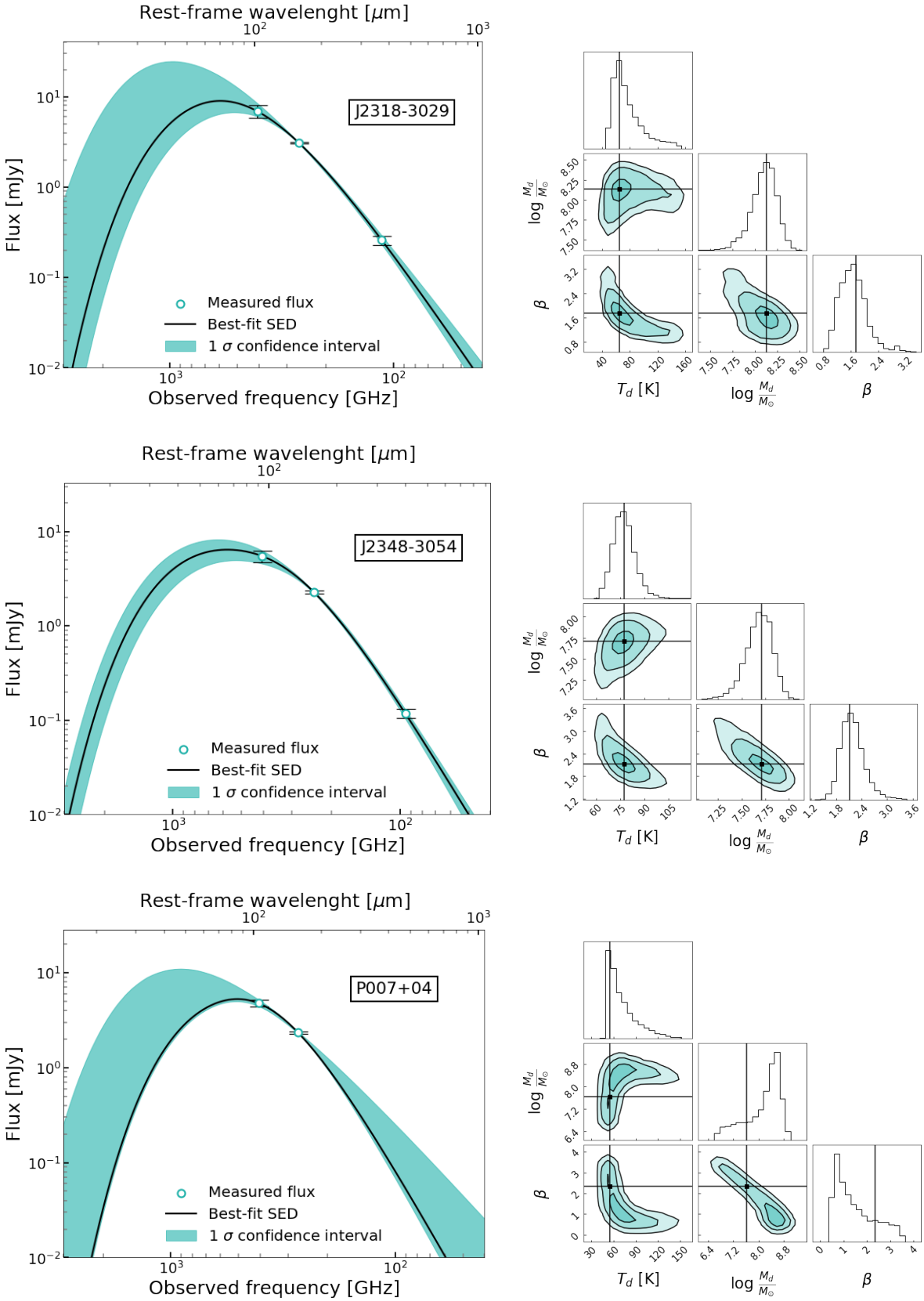

Figure 4.5: *Continued from previous page.*

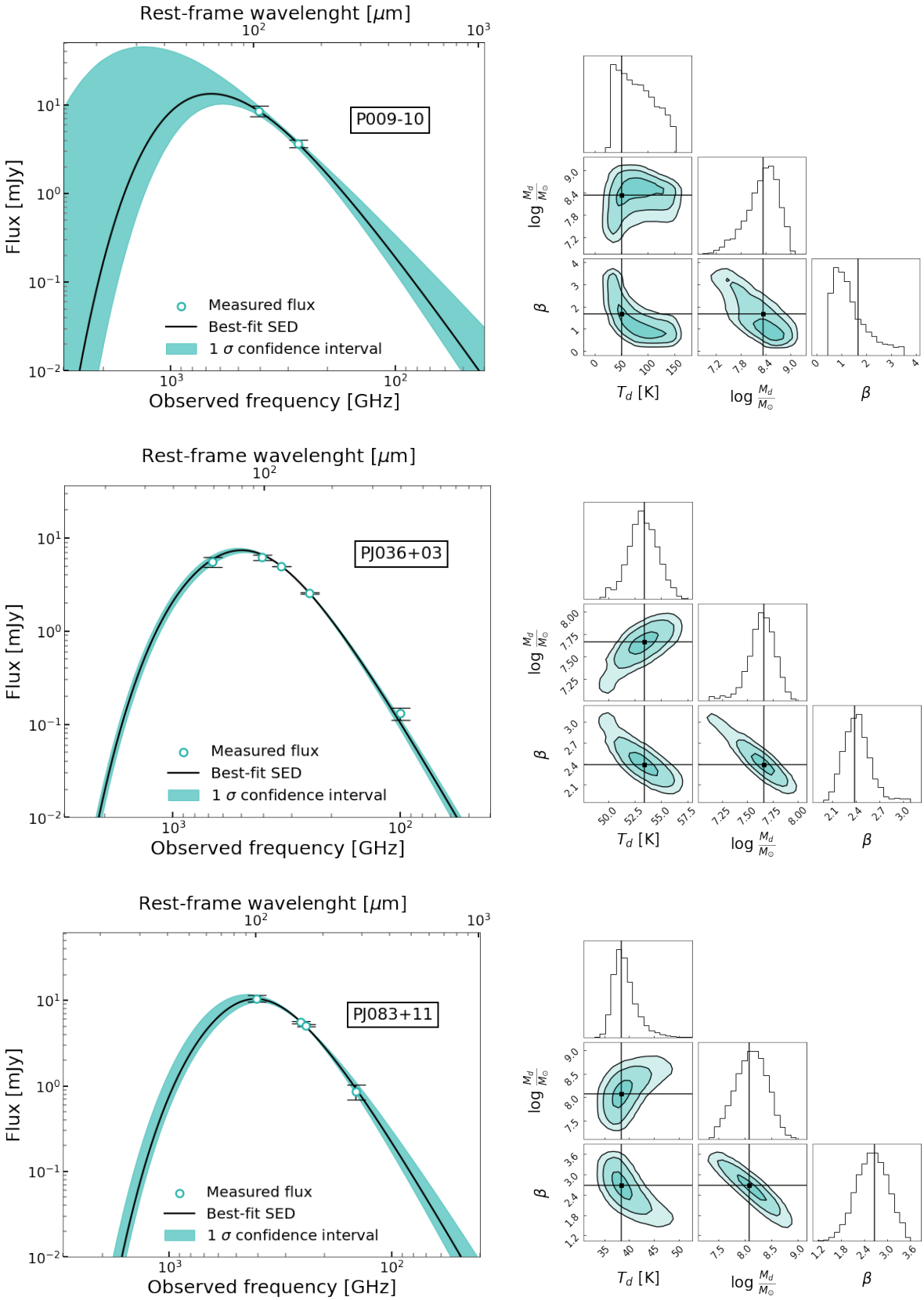

Figure 4.5: *Continued from previous page.*

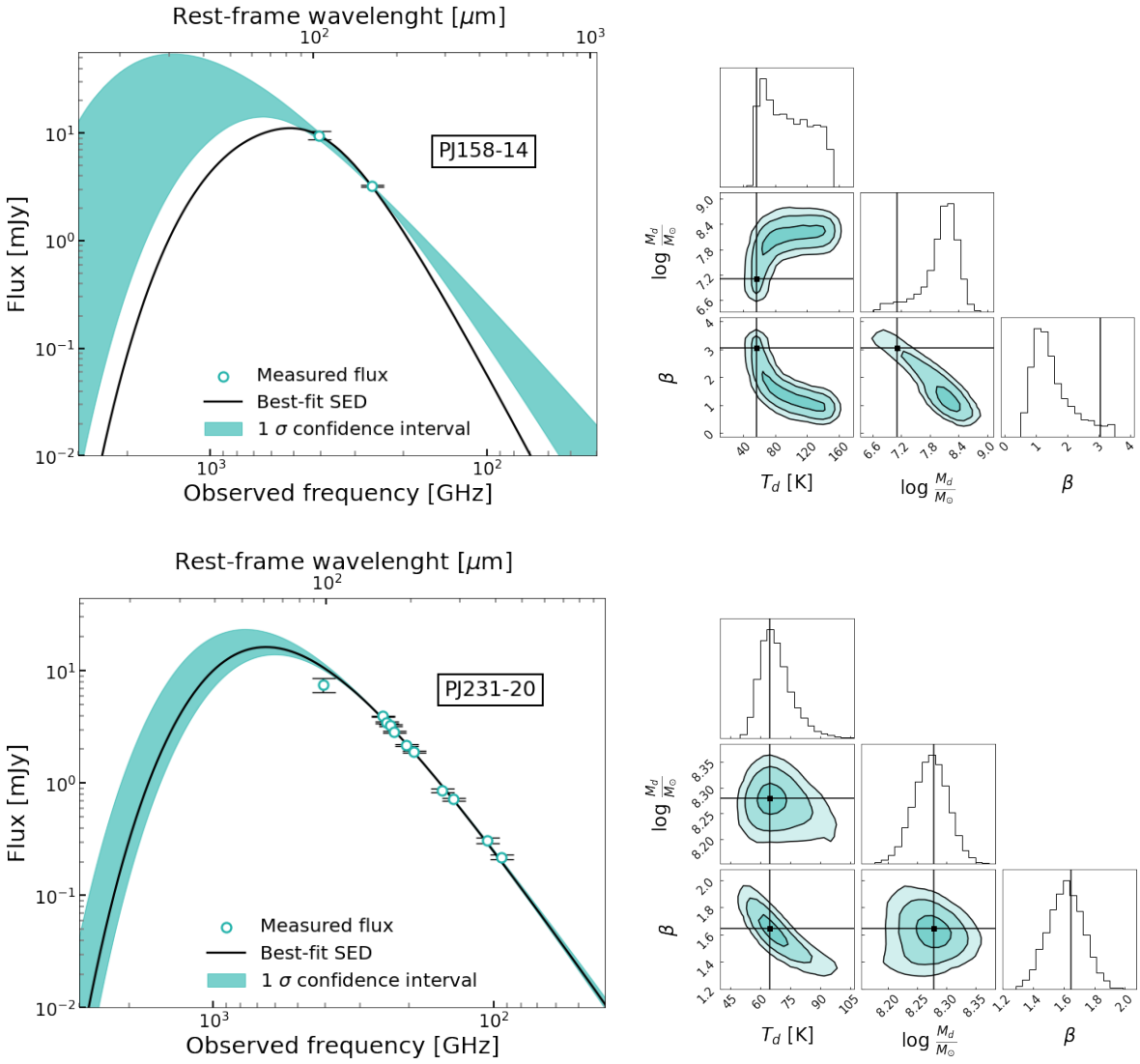

Figure 4.5: *Continued from previous page.*

4.2 The evolution of dust temperature with redshift

In this section, we introduce a model proposed in *Sommovigo et al., 2022a [88]*, which explains the observed trend of increasing dust temperature with redshift as a result of the decreasing gas depletion time (t_d), induced by the higher cosmological accretion rate in the early universe. We then compare our findings with the relevant literature, situating them within a broader scientific context and assessing how well they align with the proposed model.

4.2.1 The theoretical model

As already stated in the previous section, we find that the temperature of the dust in our sample ranges from 39 K to 77 K, values that are higher than the ones derived for local galaxies.
In the last few years several works have suggested an evolution with redshift of this quantity in **star-forming galaxies** (see, e.g., *Schreiber et al., 2018 [81]*, *Bouwens et al., 2020 [10]* or *Faisst et al., 2020 [36]*). These studies however, while agreeing on the existence of the trend, appear to be discordant in describing its behaviour: for example in *Bouwens et al., 2020 [10]* the Authors find that z and T_d can be linked by a linear relation up to $z \simeq 7.5$, while in *Faisst et al., 2020 [36]* they find that the relation seems to flatten at $z > 4$.
Both of the trends, however, have not been fully explained by a complete physical model yet. Theoretical works suggested that the increase of dust temperature with redshift could be related to the dust distribution being more concentrated in star-forming regions in high-z galaxies (*Liang et. al., 2019 [60]*), or to the increase of the specific star formation rate (sSFR) with redshift (*Shen et. al., 2022 [84]*).

Here, we briefly present a **model** proposed in *Sommovigo et al., 2022a [88]*, where the Authors attribute the origin of this relationship to the **higher star formation efficiency** ($SFE = SFR/M_g$) predicted in high-redshift galaxies by cosmological simulations.
Assuming that the UV-absorbing and the IR-emitting regions are cospatial and scattering can be neglected, the infrared luminosity L_{IR} can be written as the extincted fraction of the ultraviolet luminosity L_{UV} as:

$$L_{IR} = (1 - e^{-\tau}) \cdot L_{UV} = (1 - e^{-\tau}) \cdot K_{UV} SFR \tag{4.5}$$

where K_{UV} is the conversion factor from the SFR to the UV luminosity and its value depends mainly on the metallicity Z and the assumed initial mass function (IMF).
At the same time, according to the parametrization they adopt to describe dust physics (*Ferrara et al., 2022 [40]*), it is possible to write:

$$\frac{L_{IR}}{L_\odot} = \left(\frac{M_d}{M_\odot}\right)\left(\frac{T_d}{8.5\ \mathrm{K}}\right)^{4+\beta} \tag{4.6}$$

This expression comes from equation 2.40 and the assumption of a given set of dust refractive properties.
Combining equations 4.5 and 4.6 results in:

$$T_d = 8.5 \cdot \left[\frac{(1 - e^{-\tau})}{(M_d/M_\odot)} \cdot K_{UV} SFR\right]^{1/(4+\beta)} \quad \mathrm{K} \tag{4.7}$$

where K_{UV} is expressed in $L_\odot/(M_\odot \cdot yr^{-1})$ and SFR in $M_\odot \cdot yr^{-1}$.
Now it is possible to link the dust mass to the gas mass (M_g) with the **dust-to-gas mass ratio** D, so that $M_d = D \cdot M_g$. The Authors assume that this parameter scales linearly with metallicity down to $Z \sim 0.1 Z_\odot$ (see, e.g., *James et. al., 2002 [53]*):

$$D = D_0 \left(\frac{Z}{Z_\odot} \right) \tag{4.8}$$

where $D_0 = 1/162$ is the galactic value of the dust-to-gas mass ratio (*Rémy-Ruyer et. al., 2014 [74]*). With this result it is possible to substitute M_d in equation 4.7 to obtain:

$$T_d = 8.5 \cdot \left[\frac{(1 - e^{-\tau})}{D_0 (Z/Z_\odot)(M_g/M_\odot)} \cdot K_{UV} SFR \right]^{1/(4+\beta)} \quad \text{K} \tag{4.9}$$

In this equation we recognize the expression for the **depletion time** $t_d = SFE^{-1} = M_g/SFR$, which we can substitute in the previous equation to get:

$$\begin{aligned} T_d &= 8.5 \cdot \left[\frac{(1 - e^{-\tau})}{D_0 (Z/Z_\odot)} \cdot K_{UV} \cdot t_d^{-1} \right]^{1/(4+\beta)} \quad \text{K} \\ &= 8.5 \cdot \left[\frac{(1 - e^{-\tau})}{D_0 (Z/Z_\odot)} \cdot K_{UV} \right]^{1/(4+\beta)} \cdot t_d^{-1/(4+\beta)} \quad \text{K} \end{aligned} \tag{4.10}$$

where t_d is expressed in yr^{-1} and we isolated the dependence on the depletion time. It is in fact possible to show that is the behaviour of this quantity that rules the evolution of the temperature with redshift.
We start by expressing M_g and SFR of a galaxy as function of its total (baryonic + dark) halo mass M, and average dark matter accretion rate $\langle dM/dt \rangle$:

$$M_g = f_b M - M_* \tag{4.11}$$

and

$$SFR = SFE \cdot f_b \left\langle \frac{dM}{dt} \right\rangle \tag{4.12}$$

where $f_b = \Omega_b/\Omega_m$ is the cosmological baryonic fraction. Integrating this last equation in time with a constant SFE results in:

$$M_* = SFE \cdot f_b M \tag{4.13}$$

which can be substituted in equation 4.11 to finally get:

$$M_g = f_b \cdot M \cdot (1 - SFE) \tag{4.14}$$

Now the Authors exploit the result of various numerical simulation (*Fakhouri et al., 2010 [37]*, *Correa et al., 2015 [16]*) to express the average halo accretion rate as:

$$\left\langle \frac{dM}{dt} \right\rangle = 69.3 \cdot M_{12} \cdot f'(z) \cdot E(z) \quad M_\odot \cdot yr^{-1} \tag{4.15}$$

$$f'(z) = -0.24 + 0.75 \cdot (1 + z) \qquad E(z) = [\Omega_m (1 + z)^3 + \Omega_\Lambda]^{1/2}$$

where $M_{12} = M/(M_\odot \cdot 10^{12})$.
This finally allows, combining equations 4.14, 4.12 and 4.2.1, to express t_d as:

$$t_d = \frac{M_g}{SFR} = t_{d0}[f'(z) \cdot E(z)]^{-1} \tag{4.16}$$

where

$$t_{d0} = \frac{M(1-SFE)}{69.3 \cdot M_{12} \cdot SFE} = 14.4 \cdot 10^9 \cdot \frac{(1-SFE)}{SFE} \quad yr \tag{4.17}$$

is a timescale fixed so that $t_d(z=0) = 2$ Gyr, as measured in nearby galaxies.
Substituting now the depletion time back in equation 4.10 we get the complete expression for the dust temperature as a function of redshift:

$$T_d = 8.5 \cdot \left[t_{d0} \cdot \frac{(1-e^{-\tau})}{D_0(Z/Z_\odot)} \cdot K_{UV}\right]^{1/(4+\beta)} \cdot \left[f'(z) \cdot E(z)\right]^{1/(4+\beta)} \quad \text{K} \tag{4.18}$$

From the expressions of $E(z)$ and $f'(z)$ in equation 4.2.1 we can see that $E(z) \cdot f'(z)$ is proportional to $(z+1)^{5/2}$ (and so $t_d \propto (1+z)^{-5/2}$). This directly translates in:

$$T_d \propto (1+z)^{5/[2(4+\beta)]} \tag{4.19}$$

Despite the complex formulation, equation 4.18 is of quite easy interpretation. At fixed redshift we see that:

- An increase of the optical depth means an increase of temperature
- An increase of the metallicity yields instead a decrease of temperature

Overall, this model describes the evolution of dust temperature as primarily governed by the gas depletion time, which evolves over cosmic time. Variations in individual objects at the same redshift are introduced by differing values of metallicity or optical depth.

4.2.2 The observed trend

In figure 4.6 we compare the dust temperatures derived in this work with the ones obtained in different papers (*Franco et al., 2020 [42]*, *Sommovigo et al., 2020a [88]* and *Sommovigo et al., 2020b [87]*) for low and high-z galaxies . We then proceed with fitting a **power law relation** in the form:

$$T_d = A(1+z)^B \tag{4.20}$$

deriving:

$$A = 21.4^{+0.7}_{-0.6} \text{ K} \qquad B = 0.44^{+0.02}_{-0.02} \tag{4.21}$$

This formulation of T_d is derived from equation 4.18: the parameter A takes into account the normalization introduced by the first factor and depends on a multitude of physical quantities, while B drives the dependence on z that is carried by the second factor, and depends only on β.
According to the theoretical model, $B = 5/[2(4+\beta)]$. Using the emissivity index $\beta = 2.3 \pm 0.3$ (the average value derived for our sources) we expect B to be 0.40 ± 0.02. The fitted value of $B = 0.44 \pm 0.02$ is indeed close to this theoretical prediction. The

slight discrepancy arises because T_d does not depend solely on redshift, meaning that fitting all the data with a single power law can be misleading. Nevertheless, our value for B closely aligns with the model. In contrast, the findings of *Tripodi et al., 2024 [93]*, which report B as 0.7 ± 0.1, would imply a non physical value for β, which they explain with our same motivation.

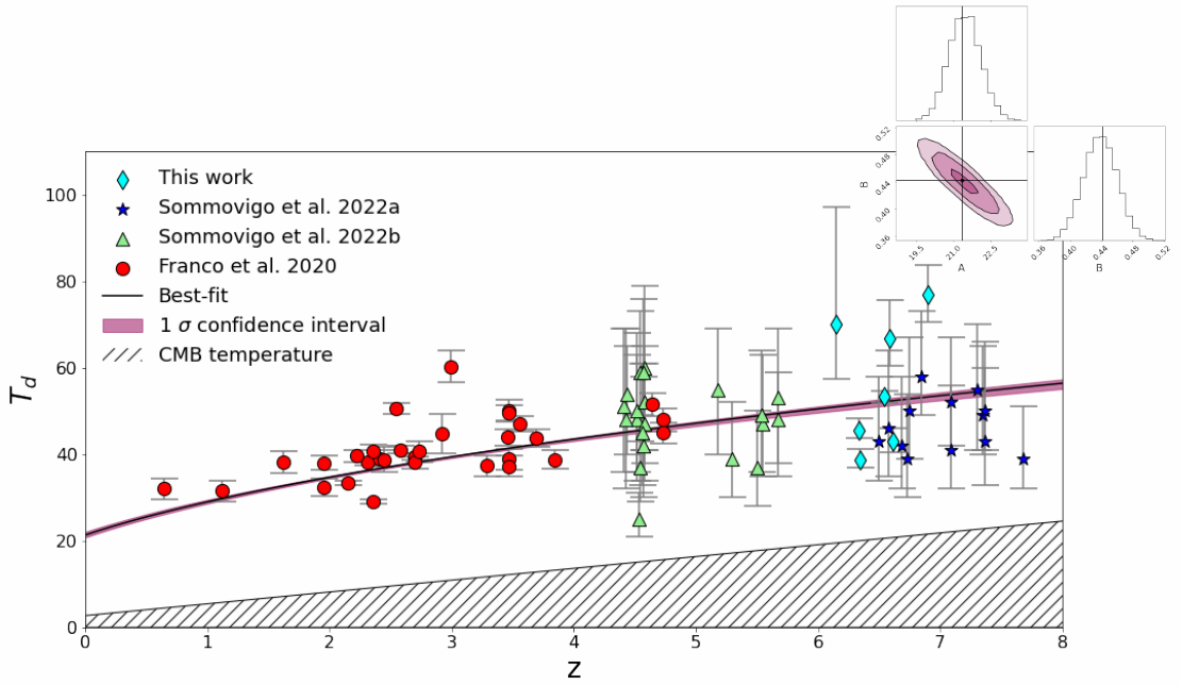

Figure 4.6: *Evolution of the dust temperature across cosmic time, with the best fit for equation 4.20. The fit contour plot is reported with significance levels of 1, 2, and 3 σ.*

One point of note is that the sources in our sample are very bright QSOs, while the others are classified as star-forming galaxies. Therefore, the AGN contribution could in principle be biasing the obtained dust temperature by contaminating the observed infrared emission of the host galaxy. This problematic will be addressed more in depth in the next section.

4.3 Dust heating from AGNs

One of the main topics we want to address in this work is the study of the dust temperature in quasars host galaxies at the end of the epoch of reionization. What we are deriving in our analysis is the so called **effective dust temperature**, which may not correspond to the physical temperature (*Liang et al., 2019 [60]*).
In particular, the presence of a very bright active galactic nucleus may heat the innermost dust, whose emission could contaminate our unresolved band 8 flux measurements. An example of this phenomenon is presented in *Tsukui et al., 2023 [94]*, where the Authors fit a graybody emission to the observed data points by assuming a single dust temperature, and then decompose the emission into a galaxy-scale component and a component originating from the innermost beam of resolution. In the first case they decide to not include in the fit the data point at the highest frequency, as it was impossible to explain with a single graybody curve, and retrieve a dust temperature of $39^{+2.4}_{-2.9}$. In the second case they find a temperature of the cold dust component (associated to the galaxy-scale emission) of $29^{+4.5}_{-3.6}$ K, and of 96^{+37}_{-26} K for the warm one (which is associated to AGN heated dust, with possible contribution from the dusty torus). The single component and the decomposed fits are shown in figure 4.7.

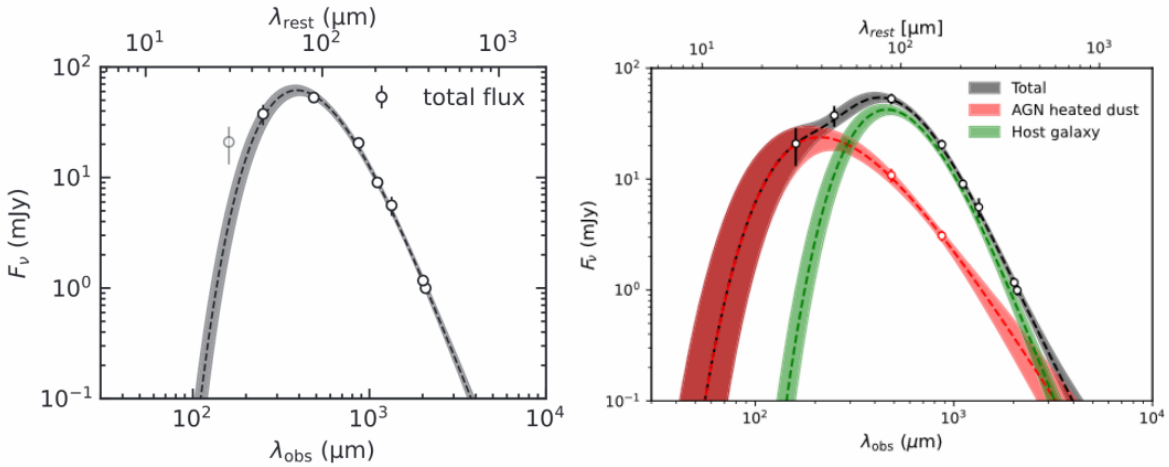

Figure 4.7: Left panel: *the total emission of the z=4.4 QSO BRI1335–0417 fitted with a single graybody curve. The gray data point was not included in the fit.* Right panel: *decomposed emission of the same source fitted with two graybody curves at different temperatures. From* Tsukui et al., 2023 [94].

This raises the concern that the values obtained from the SED fitting for this quantity may not accurately represent the true ones, leaving open the possibility that the temperature estimates in our sources could be biased. In fact, the presence of a temperature gradient peaking in the galaxy center has been suggested by the results obtained for the lensed QSO J0439-1634. However, its contribution to the rest of the sample remains completely unconstrained.
There are, however, some first-order arguments that can be made against this hypothesis. First, since our observations do not probe frequencies higher than the emission peak, the measured contribution of the AGN-heated dust component may be negligible. Second, our sources appear to follow the trend in dust temperature against redshift that is observed in normal galaxies (see figure 4.6), which is not what would be expected in

the case of AGN contamination.

To investigate more on this possibility we gather measurements of the bolometric luminosity of the AGN L_{bol} from the literature (*Andika et al., 2020 [2]*, *Farina et al, 2022 [39]* and *Mazzucchelli et al., 2023 [65]*), and we compare them to the infrared luminosities L_{IR} derived in this work (see figure 4.8). In fact, while we assume that L_{IR} probes star formation processes in the host galaxy, L_{bol} is a proxy of the power emitted by the AGN via accretion and it is derived from rest-frame UV observations. This means that, if a correlation between these two quantities is detected, it may due to two main reasons:

- We are effectively biased by the AGN contribution, and the correlation is set by the different power that a more luminous QSO provides to the surrounding dust.
- The bolometric and the infrared luminosities have the same drivers (see, e.g., *Shao et al., 2010 [83]*). One possible candidate are, for example, mergers, which may fuel both star formation and accretion onto the SMBH.

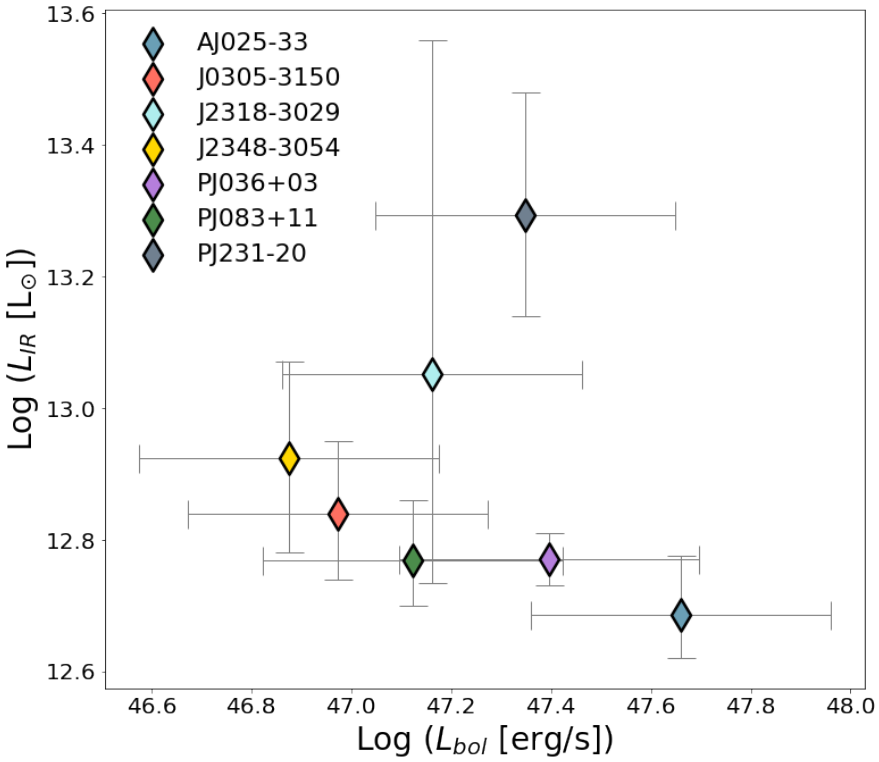

Figure 4.8: *Comparison between bolometric and infrared luminosities of the sources in our sample. The bolometric luminosities are from* Andika et al., 2020 [2], Farina et al, 2022 [39] *and* Mazzucchelli et al., 2023 [65] *and are displayed with typical uncertainties of 0.3 dex (*Shen et al. 2011 [86]*).*

In our sample, however, **no trace of correlation** is found. This result is somewhat limited, as the errors associated with both luminosities may hide any existing relationship. Additionally, the sample is limited to the brightest range of luminosities. In order to derive any statistically significant conclusions, we would need a broader sample that also includes the low-luminosity regime.

What we conclude from this analysis is that, based on the information and data available at this time, we do not find any significant evidence of AGN contributing to the derived physical quantities. However, this possibility still requires further research to be completely ruled out.

Chapter 5

Conclusion and future perspectives

In this study, we addressed the open problem of investigating quasar host galaxies at early cosmic epochs ($z > 6$). We explored the complex physics governing these systems and outlined the main observational techniques used to probe their properties, while also discussing the potential connections between their evolutionary paths and those of the supermassive black holes at their centers.
Utilizing new ALMA Band 8 observations, we analyzed the dust continuum emission from 11 type 1 radio quiet quasars, successfully deriving the far infrared properties of 7 of these sources through spectral energy distribution fitting. These findings were then put in a broader scientific context, in order to assess the evolutionary state of these objects and to provide insights about star formation processes in the high-redshift universe. Below, we report the principal outcomes of this work:

Derived far infrared properties
We have been able to derive dust temperatures, masses, emissivity indexes, infrared luminosities and star formation rates via SED fitting of the dust graybody emission for 7 sources at redshifts larger than 6 (see table 4.1). The obtained results have been used to characterize quasar host galaxies and suggest that for these objects the widespread assumption of optically thin emission has to be handled with care, especially when used to derive analytically the infrared luminosity.

Evolutionary state
Our sample exhibits both intense star formation and rapid black hole accretion. When compared to local scaling relations, the quasar host galaxies reveal overmassive black holes relative to their hosts ($\sim 4\sigma$ above the local relation on average), even when considering upper limits on the stellar mass. The underlying cause of this recurring observation is not straightforward: these quasars may eventually migrate towards the local black hole-host galaxy relation as they evolve, or they might represent a population of outliers that remain above the relation, potentially not being fully representative of the high-redshift quasar population.

Dust temperature evolution
The dust temperatures derived for the quasar host galaxies in our sample align well with the temperature evolution model proposed by *Sommovigo et al., 2022a [88]*. This may serve as an observational evidence of an increased cosmic accretion rate in the early universe. However, disentangling this effect from the one introduced by differences in

metallicity and optical depth across individual galaxies remains difficult, as both can also impact dust temperature.

Influence of the AGN in the derived results
Our analysis shows no clear evidence that AGN activity significantly biases the galaxy-averaged far infrared properties. Nevertheless, to fully address this question, additional observations and further analysis are required.

Future perspectives
Although this work has provided reliable estimates of the star-forming medium properties in high-redshift quasar hosts, research in this field is still in its early stages. In the future, we plan to incorporate continuum flux measurements from the NOEMA project S24CH (which I am the PI of) to extend our sample by adding 3 more objects, increasing the statistical significance of our findings.
Additionally, using ALMA to its full potential could enable us to obtain spatially resolved maps of dust emission (see figure 5.1). Our group has acquired a new set of ALMA multi-band high resolution observations ($\sim$ 0.1 arcsec), which will help dissect the effects of temperature variations across the galaxy. These data will provide crucial insights into the radial distribution of dust properties, probing their variation over a scale of $\sim$ 500 pc. As a consequence, this will allow us to better investigate the influence of the central AGN on the surrounding medium.

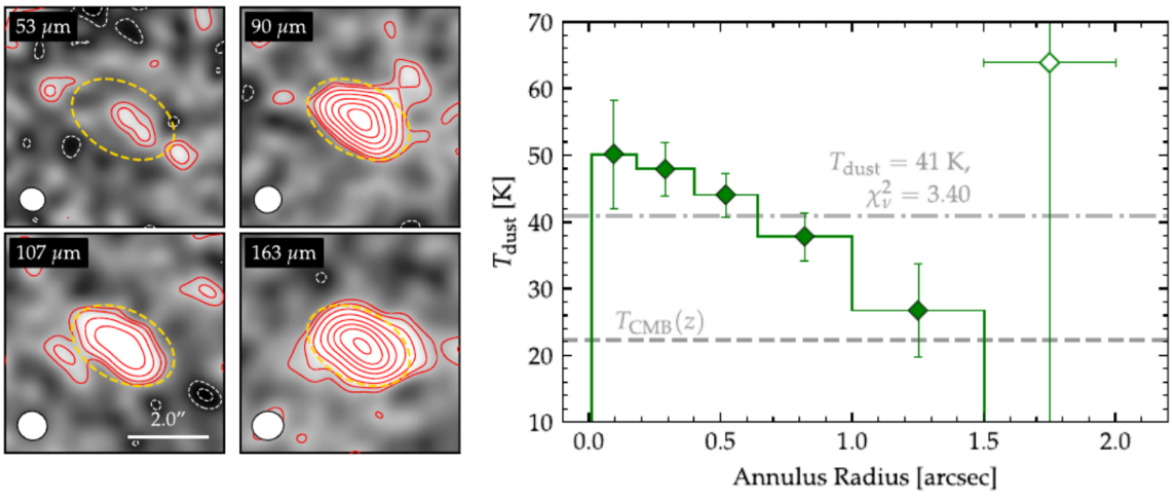

Figure 5.1: Left panel: *ALMA bands 9, 8, 7 and 6 resolved maps of the dust continuum emission of the z=7.13 strongly lensed galaxy A1689-zD1. The yellow dashed ellipsis is the area from which the total flux was extracted to obtain galaxy-averaged properties.* **Right panel:** *dust temperature radial profile derived from spatially resolved SED fitting. The gray dash-dotted line represents the galaxy-averaged result. From* Akins et al., 2022 [1].

Bibliography

[1] Akins, H. B., Fujimoto, S., Finlator, K., Watson, D., Knudsen, K. K., Richard, J., Bakx, T. J. L. C., Hashimoto, T., Inoue, A. K., Matsuo, H., Michałowski, M. J., and Tamura, Y. (2022). ALMA Reveals Extended Cool Gas and Hot Ionized Outflows in a Typical Star-forming Galaxy at Z = 7.13. *ApJ*, 934(1):64.

[2] Andika, I. T., Jahnke, K., Onoue, M., Bañados, E., Mazzucchelli, C., Novak, M., Eilers, A.-C., Venemans, B. P., Schindler, J.-T., Walter, F., Neeleman, M., Simcoe, R. A., Decarli, R., Farina, E. P., Marian, V., Pensabene, A., Cooper, T. M., and Rojas, A. F. (2020). Probing the Nature of High-redshift Weak Emission Line Quasars: A Young Quasar with a Starburst Host Galaxy. *ApJ*, 903(1):34.

[3] Ansarinejad, B., Shanks, T., Bielby, R. M., Metcalfe, N., Infante, L., Murphy, D. N. A., Rosario, D. J., and Stach, S. M. (2022). The nature of sub-millimetre galaxies II: an ALMA comparison of SMG dust heating mechanisms. *MNRAS*, 510(4):4976–4991.

[4] Barkana, R. and Loeb, A. (2001). In the beginning: the first sources of light and the reionization of the universe. *Physics Reports*, 349(2):125–238.

[5] Begum, A., Stanimirović, S., Goss, W. M., Heiles, C., Pavkovich, A. S., and Hennebelle, P. (2010). The Thermally Unstable Warm Neutral Medium: Key for Modeling the Interstellar Medium. *ApJ*, 725(2):1779–1785.

[6] Bendo, G. J., Urquhart, S. A., Serjeant, S., Bakx, T., Hagimoto, M., Cox, P., Neri, R., Lehnert, M. D., Dannerbauer, H., Amvrosiadis, A., Andreani, P., Baker, A. J., Beelen, A., Berta, S., Borsato, E., Buat, V., Butler, K. M., Cooray, A., De Zotti, G., Dunne, L., Dye, S., Eales, S., Enia, A., Fan, L., Gavazzi, R., González-Nuevo, J., Harris, A. I., Herrera, C. N., Hughes, D. H., Ismail, D., Jones, B. M., Kohno, K., Krips, M., Lagache, G., Marchetti, L., Massardi, M., Messias, H., Negrello, M., Omont, A., Pérez-Fournon, I., Riechers, D. A., Scott, D., Smith, M. W. L., Stanley, F., Tamura, Y., Temi, P., van der Werf, P., Verma, A., Vlahakis, C., Weiß, A., Yang, C., and Young, A. J. (2023). The bright extragalactic ALMA redshift survey (BEARS) - II. Millimetre photometry of gravitational lens candidates. *MNRAS*, 522(2):2995–3017.

[7] Blandford, R. D. and McKee, C. F. (1982). Reverberation mapping of the emission line regions of Seyfert galaxies and quasars. *ApJ*, 255:419–439.

[8] Bogdán, Á., Goulding, A. D., Natarajan, P., Kovács, O. E., Tremblay, G. R., Chadayammuri, U., Volonteri, M., Kraft, R. P., Forman, W. R., Jones, C., Churazov, E., and Zhuravleva, I. (2024). Evidence for heavy-seed origin of early supermassive black holes from a z $\approx$ 10 X-ray quasar. *Nature Astronomy*, 8:126–133.

[9] Bolatto, A. D., Wolfire, M., and Leroy, A. K. (2013). The CO-to-H_2 Conversion Factor. *ARA&A*, 51(1):207–268.

[10] Bouwens, R., González-López, J., Aravena, M., Decarli, R., Novak, M., Stefanon, M., Walter, F., Boogaard, L., Carilli, C., Dudzevičiūtė, U., Smail, I., Daddi, E., da Cunha, E., Ivison, R., Nanayakkara, T., Cortes, P., Cox, P., Inami, H., Oesch, P., Popping, G., Riechers, D., van der Werf, P., Weiss, A., Fudamoto, Y., and Wagg, J. (2020). The ALMA Spectroscopic Survey Large Program: The Infrared Excess of z = 1.5-10 UV-selected Galaxies and the Implied High-redshift Star Formation History. *ApJ*, 902(2):112.

[11] Bromm, V. and Yoshida, N. (2011). The First Galaxies. *ARA&A*, 49(1):373–407.

[12] Butler, K. M., van der Werf, P. P., Topkaras, T., Rybak, M., Venemans, B. P., Walter, F., and Decarli, R. (2023). Molecular Outflows in z > 6 Unobscured QSO Hosts Driven by Star Formation. *ApJ*, 944(2):134.

[13] Carniani, S., Gallerani, S., Vallini, L., Pallottini, A., Tazzari, M., Ferrara, A., Maiolino, R., Cicone, C., Feruglio, C., Neri, R., D'Odorico, V., Wang, R., and Li, J. (2019). Constraints on high-J CO emission lines in z ∼ 6 quasars. *MNRAS*, 489(3):3939–3952.

[14] Carniani, S., Hainline, K., D'Eugenio, F., Eisenstein, D. J., Jakobsen, P., Witstok, J., Johnson, B. D., Chevallard, J., Maiolino, R., Helton, J. M., Willott, C., Robertson, B., Alberts, S., Arribas, S., Baker, W. M., Bhatawdekar, R., Boyett, K., Bunker, A. J., Cameron, A. J., Cargile, P. A., Charlot, S., Curti, M., Curtis-Lake, E., Egami, E., Giardino, G., Isaak, K., Ji, Z., Jones, G. C., Kumari, N., Maseda, M. V., Parlanti, E., Pérez-González, P. G., Rawle, T., Rieke, G., Rieke, M., Del Pino, B. R., Saxena, A., Scholtz, J., Smit, R., Sun, F., Tacchella, S., Übler, H., Venturi, G., Williams, C. C., and Willmer, C. N. A. (2024). Spectroscopic confirmation of two luminous galaxies at a redshift of 14. *Nature*, 633(8029):318–322.

[15] Cimatti, A., Daddi, E., and Renzini, A. (2006). Mass downsizing and "top-down" assembly of early-type galaxies. *A&A*, 453(2):L29–L33.

[16] Correa, C. A., Wyithe, J. S. B., Schaye, J., and Duffy, A. R. (2015). The accretion history of dark matter haloes - II. The connections with the mass power spectrum and the density profile. *MNRAS*, 450(2):1521–1537.

[17] Coulman, C. E. (1985). Fundamental and applied aspects of astronomical seeing. *ARA&A*, 23.

[18] da Cunha, E., Groves, B., Walter, F., Decarli, R., Weiss, A., Carilli, C., Daddi, E., Riechers, D., Bertoldi, F., Cortes, P., Cox, P., Elbaz, D., Ivison, R. J., Karim, A., Rix, H.-W., Schinnerer, E., and Smail, I. (2013). On the effect of the cosmic microwave background in high-redshift (sub-)millimeter observations. *ApJ*, 766(1):13.

[19] De Looze, I., Cormier, D., Lebouteiller, V., Madden, S., Baes, M., Bendo, G. J., Boquien, M., Boselli, A., Clements, D. L., Cortese, L., Cooray, A., Galametz, M., Galliano, F., Graciá-Carpio, J., Isaak, K., Karczewski, O. Ł., Parkin, T. J., Pellegrini, E. W., Rémy-Ruyer, A., Spinoglio, L., Smith, M. W. L., and Sturm, E. (2014). The

applicability of far-infrared fine-structure lines as star formation rate tracers over wide ranges of metallicities and galaxy types. *A&A*, 568:A62.

[20] De Rosa, G., Venemans, B. P., Decarli, R., Gennaro, M., Simcoe, R. A., Dietrich, M., Peterson, B. M., Walter, F., Frank, S., McMahon, R. G., Hewett, P. C., Mortlock, D. J., and Simpson, C. (2014). Black Hole Mass Estimates and Emission-line Properties of a Sample of Redshift z > 6.5 Quasars. *ApJ*, 790(2):145.

[21] Decarli, R., Falomo, R., Treves, A., Labita, M., Kotilainen, J. K., and Scarpa, R. (2010). The quasar MBH-Mhost relation through cosmic time - II. Evidence for evolution from z = 3 to the present age. *MNRAS*, 402(4):2453–2461.

[22] Decarli, R., Pensabene, A., Diaz-Santos, T., Ferkinhoff, C., Strauss, M. A., Venemans, B. P., Walter, F., Bañados, E., Bertoldi, F., Fan, X., Farina, E. P., Riechers, D. A., Rix, H.-W., and Wang, R. (2023). A comprehensive view of the interstellar medium in a quasar host galaxy at z ≈ 6.4. *A&A*, 673:A157.

[23] Decarli, R., Pensabene, A., Venemans, B., Walter, F., Bañados, E., Bertoldi, F., Carilli, C. L., Cox, P., Fan, X., Farina, E. P., Ferkinhoff, C., Groves, B. A., Li, J., Mazzucchelli, C., Neri, R., Riechers, D. A., Uzgil, B., Wang, F., Wang, R., Weiss, A., Winters, J. M., and Yang, J. (2022). Molecular gas in z ∼ 6 quasar host galaxies. *A&A*, 662:A60.

[24] Decarli, R., Walter, F., Venemans, B. P., Bañados, E., Bertoldi, F., Carilli, C., Fan, X., Farina, E. P., Mazzucchelli, C., Riechers, D., Rix, H. W., Strauss, M. A., Wang, R., and Yang, Y. (2017). Rapidly star-forming galaxies adjacent to quasars at redshifts exceeding 6. *Nature*, 545(7655):457–461.

[25] Decarli, R., Walter, F., Venemans, B. P., Bañados, E., Bertoldi, F., Carilli, C., Fan, X., Farina, E. P., Mazzucchelli, C., Riechers, D., Rix, H.-W., Strauss, M. A., Wang, R., and Yang, Y. (2018). An ALMA [C II] Survey of 27 Quasars at z > 5.94. *ApJ*, 854(2):97.

[26] Díaz-Santos, T., Armus, L., Charmandaris, V., Lu, N., Stierwalt, S., Stacey, G., Malhotra, S., van der Werf, P. P., Howell, J. H., Privon, G. C., Mazzarella, J. M., Goldsmith, P. F., Murphy, E. J., Barcos-Muñoz, L., Linden, S. T., Inami, H., Larson, K. L., Evans, A. S., Appleton, P., Iwasawa, K., Lord, S., Sanders, D. B., and Surace, J. A. (2017). A Herschel/PACS Far-infrared Line Emission Survey of Local Luminous Infrared Galaxies. *ApJ*, 846(1):32.

[27] Díaz-Santos, T., Armus, L., Charmandaris, V., Stierwalt, S., Murphy, E. J., Haan, S., Inami, H., Malhotra, S., Meijerink, R., Stacey, G., Petric, A. O., Evans, A. S., Veilleux, S., van der Werf, P. P., Lord, S., Lu, N., Howell, J. H., Appleton, P., Mazzarella, J. M., Surace, J. A., Xu, C. K., Schulz, B., Sanders, D. B., Bridge, C., Chan, B. H. P., Frayer, D. T., Iwasawa, K., Melbourne, J., and Sturm, E. (2013). Explaining the [C II]157.7 μm Deficit in Luminous Infrared Galaxies—First Results from a Herschel/PACS Study of the GOALS Sample. *ApJ*, 774(1):68.

[28] Dibai, E. A. (1977). Mass of the central bodies of active galaxy nuclei. *Soviet Astronomy Letters*, 3:1–3.

[29] Ding, X., Silverman, J. D., and Onoue, M. (2022). Opening the Era of Quasar-host Studies at High Redshift with JWST. *ApJL*, 939(2):L28.

[30] Draine, B. T. (1990). Evolution of interstellar dust. In Blitz, L., editor, *The Evolution of the Interstellar Medium*, volume 12 of *Astronomical Society of the Pacific Conference Series*, pages 193–205.

[31] Draine, B. T. (2003). Interstellar Dust Grains. *ARA&A*, 41:241–289.

[32] Draine, B. T. (2010). *Physics of the Interstellar and Intergalactic Medium*. Princeton University Press.

[33] Draine, B. T. (2024). Sensitivity of Polarization to Grain Shape. I. Convex Shapes. *ApJ*, 961(1):103.

[34] Eckart, A. and Genzel, R. (1996). Observations of stellar proper motions near the Galactic Centre. *Nature*, 383(6599):415–417.

[35] Eilers, A.-C., Hennawi, J. F., Decarli, R., Davies, F. B., Venemans, B., Walter, F., Bañados, E., Fan, X., Farina, E. P., Mazzucchelli, C., Novak, M., Schindler, J.-T., Simcoe, R. A., Wang, F., and Yang, J. (2020). Detecting and Characterizing Young Quasars. I. Systemic Redshifts and Proximity Zone Measurements. *ApJ*, 900(1):37.

[36] Faisst, A. L., Fudamoto, Y., Oesch, P. A., Scoville, N., Riechers, D. A., Pavesi, R., and Capak, P. (2020). ALMA characterizes the dust temperature of z $\sim$ 5.5 star-forming galaxies. *MNRAS*, 498(3):4192–4204.

[37] Fakhouri, O., Ma, C.-P., and Boylan-Kolchin, M. (2010). The merger rates and mass assembly histories of dark matter haloes in the two Millennium simulations. *MNRAS*, 406(4):2267–2278.

[38] Fan, X., Wang, F., Yang, J., Keeton, C. R., Yue, M., Zabludoff, A., Bian, F., Bonaglia, M., Georgiev, I. Y., Hennawi, J. F., Li, J., McGreer, I. D., Naidu, R., Pacucci, F., Rabien, S., Thompson, D., Venemans, B., Walter, F., Wang, R., and Wu, X.-B. (2019). The Discovery of a Gravitationally Lensed Quasar at z = 6.51. *ApJL*, 870(2):L11.

[39] Farina, E. P., Schindler, J.-T., Walter, F., Bañados, E., Davies, F. B., Decarli, R., Eilers, A.-C., Fan, X., Hennawi, J. F., Mazzucchelli, C., Meyer, R. A., Trakhtenbrot, B., Volonteri, M., Wang, F., Worseck, G., Yang, J., Gutcke, T. A., Venemans, B. P., Bosman, S. E. I., Costa, T., De Rosa, G., Drake, A. B., and Onoue, M. (2022). The X-shooter/ALMA Sample of Quasars in the Epoch of Reionization. II. Black Hole Masses, Eddington Ratios, and the Formation of the First Quasars. *ApJ*, 941(2):106.

[40] Ferrara, A., Sommovigo, L., Dayal, P., Pallottini, A., Bouwens, R. J., Gonzalez, V., Inami, H., Smit, R., Bowler, R. A. A., Endsley, R., Oesch, P., Schouws, S., Stark, D., Stefanon, M., Aravena, M., da Cunha, E., De Looze, I., Fudamoto, Y., Graziani, L., Hodge, J., Riechers, D., Schneider, R., Algera, H. S. B., Barrufet, L., Hygate, A. P. S., Labbé, I., Li, C., Nanayakkara, T., Topping, M., and van der Werf, P. (2022). The ALMA REBELS Survey. Epoch of Reionization giants: Properties of dusty galaxies at z $\approx$ 7. *MNRAS*, 512(1):58–72.

[41] Foreman-Mackey, D., Hogg, D. W., Lang, D., and Goodman, J. (2013). emcee: The MCMC Hammer. *PASP*, 125(925):306.

[42] Franco, M., Elbaz, D., Zhou, L., Magnelli, B., Schreiber, C., Ciesla, L., Dickinson, M., Nagar, N., Magdis, G., Alexander, D. M., Béthermin, M., Demarco, R., Daddi, E., Wang, T., Mullaney, J., Sargent, M., Inami, H., Shu, X., Bournaud, F., Chary, R., Coogan, R. T., Ferguson, H., Finkelstein, S. L., Giavalisco, M., Gómez-Guijarro, C., Iono, D., Juneau, S., Lagache, G., Lin, L., Motohara, K., Okumura, K., Pannella, M., Papovich, C., Pope, A., Rujopakarn, W., Silverman, J., and Xiao, M. (2020). GOODS-ALMA: The slow downfall of star formation in z = 2-3 massive galaxies. *A&A*, 643:A30.

[43] Galametz, M., Kennicutt, R. C., Albrecht, M., Aniano, G., Armus, L., Bertoldi, F., Calzetti, D., Crocker, A. F., Croxall, K. V., Dale, D. A., Donovan Meyer, J., Draine, B. T., Engelbracht, C. W., Hinz, J. L., Roussel, H., Skibba, R. A., Tabatabaei, F. S., Walter, F., Weiss, A., Wilson, C. D., and Wolfire, M. G. (2012). Mapping the cold dust temperatures and masses of nearby KINGFISH galaxies with Herschel. *MNRAS*, 425(1):763–787.

[44] Gao, L., Yoshida, N., Abel, T., Frenk, C. S., Jenkins, A., and Springel, V. (2007). The first generation of stars in the Λ cold dark matter cosmology. *MNRAS*, 378(2):449–468.

[45] Grier, C. J., Peterson, B. M., Pogge, R. W., Denney, K. D., Bentz, M. C., Martini, P., Sergeev, S. G., Kaspi, S., Minezaki, T., Zu, Y., Kochanek, C. S., Siverd, R., Shappee, B., Stanek, K. Z., Araya Salvo, C., Beatty, T. G., Bird, J. C., Bord, D. J., Borman, G. A., Che, X., Chen, C., Cohen, S. A., Dietrich, M., Doroshenko, V. T., Drake, T., Efimov, Y. S., Free, N., Ginsburg, I., Henderson, C. B., King, A. L., Koshida, S., Mogren, K., Molina, M., Mosquera, A. M., Nazarov, S. V., Okhmat, D. N., Pejcha, O., Rafter, S., Shields, J. C., Skowron, J., Szczygiel, D. M., Valluri, M., and van Saders, J. L. (2012). Reverberation Mapping Results for Five Seyfert 1 Galaxies. *ApJ*, 755(1):60.

[46] Grün, E., Fechtig, H., Leinert, C., Berg, O. E., Gustafson, B. A. S., and Dermott, S. (2001). *Interplanetary Dust*. Springer-Verlag Berlin Heidelberg.

[47] Heckman, T. M. and Best, P. N. (2014). The Coevolution of Galaxies and Supermassive Black Holes: Insights from Surveys of the Contemporary Universe. *ARA&A*, 52:589–660.

[48] Hickox, R. C. and Alexander, D. M. (2018). Obscured Active Galactic Nuclei. *ARA&A*, 56:625–671.

[49] Högbom, J. A. (1974). Aperture Synthesis with a Non-Regular Distribution of Interferometer Baselines. *A&A supp.*, 15:417.

[50] Hopkins, P. F., Hernquist, L., Cox, T. J., and Kereš, D. (2008). A Cosmological Framework for the Co-Evolution of Quasars, Supermassive Black Holes, and Elliptical Galaxies. I. Galaxy Mergers and Quasar Activity. *ApJS*, 175(2):356–389.

[51] Hu, E. M. and McMahon, R. G. (1996). Detection of Lyman-α-emitting galaxies at redshift 4.55. *Nature*, 382(6588):231–233.

[52] Izumi, T., Onoue, M., Shirakata, H., Nagao, T., Kohno, K., Matsuoka, Y., Imanishi, M., Strauss, M. A., Kashikawa, N., Schulze, A., Silverman, J. D., Fujimoto, S., Harikane, Y., Toba, Y., Umehata, H., Nakanishi, K., Greene, J. E., Tamura, Y., Taniguchi, A., Yamaguchi, Y., Goto, T., Hashimoto, Y., Ikarashi, S., Iono, D., Iwasawa, K., Lee, C.-H., Makiya, R., Minezaki, T., and Tang, J.-J. (2018). Subaru High-z Exploration of Low-Luminosity Quasars (SHELLQs). III. Star formation properties of the host galaxies at z $\gtrsim$ 6 studied with ALMA. *PASJ*, 70(3):36.

[53] James, A., Dunne, L., Eales, S., and Edmunds, M. G. (2002). SCUBA observations of galaxies with metallicity measurements: a new method for determining the relation between submillimetre luminosity and dust mass. *MNRAS*, 335(3):753–761.

[54] James J. Condon, Scott M. Ransom (2016). *Essential Radio Astronomy*. Princeton University Press.

[55] Jones, A. P. (2004). Dust Destruction Processes. In Witt, A. N., Clayton, G. C., and Draine, B. T., editors, *Astrophysics of Dust*, volume 309 of *Astronomical Society of the Pacific Conference Series*, page 347.

[56] Kaasinen, M., Venemans, B., Harrington, K. C., Boogaard, L. A., Meyer, R. A., Bañados, E., Decarli, R., Walter, F., Neeleman, M., Calistro Rivera, G., and da Cunha, E. (2024). The cold molecular gas in z $\gtrsim$ 6 quasar host galaxies. *A&A*, 684:A33.

[57] Kaspi, S., Smith, P. S., Netzer, H., Maoz, D., Jannuzi, B. T., and Giveon, U. (2000). Reverberation Measurements for 17 Quasars and the Size-Mass-Luminosity Relations in Active Galactic Nuclei. *ApJ*, 533(2):631–649.

[58] Kormendy, J. and Ho, L. C. (2013). Coevolution (Or Not) of Supermassive Black Holes and Host Galaxies. *ARA&A*, 51(1):511–653.

[59] Kroupa, P. and Weidner, C. (2003). Galactic-Field Initial Mass Functions of Massive Stars. *ApJ*, 598(2):1076–1078.

[60] Liang, L., Feldmann, R., Kereš, D., Scoville, N. Z., Hayward, C. C., Faucher-Giguère, C.-A., Schreiber, C., Ma, X., Hopkins, P. F., and Quataert, E. (2019). On the dust temperatures of high-redshift galaxies. *MNRAS*, 489(1):1397–1422.

[61] Liao, C.-L., Chen, C.-C., Wang, W.-H., Smail, I., Ao, Y., Chapman, S., Dudzevičiūtė, U., Castillo, M., Lee, M., Serjeant, S., Swinbank, M., Taylor, D., Umehata, H., and Zhao, Y. (2024). An alma spectroscopic survey of the brightest submillimeter galaxies in the scuba-2-cosmos field (as2cospec): Physical properties of z = 2–5 ultra- and hyperluminous infrared galaxies. *ApJ*, 961:226.

[62] Lupi, A., Haardt, F., Dotti, M., Fiacconi, D., Mayer, L., and Madau, P. (2016). Growing massive black holes through supercritical accretion of stellar-mass seeds. *MNRAS*, 456(3):2993–3003.

[63] Mathis, J. S., Rumpl, W., and Nordsieck, K. H. (1977). The size distribution of interstellar grains. *ApJ*, 217:425–433.

[64] Mazzucchelli, C., Bañados, E., Venemans, B. P., Decarli, R., Farina, E. P., Walter, F., Eilers, A. C., Rix, H. W., Simcoe, R., Stern, D., Fan, X., Schlafly, E., De Rosa, G., Hennawi, J., Chambers, K. C., Greiner, J., Burgett, W., Draper, P. W., Kaiser, N., Kudritzki, R. P., Magnier, E., Metcalfe, N., Waters, C., and Wainscoat, R. J. (2017). Physical Properties of 15 Quasars at z $\gtrsim$ 6.5. *ApJ*, 849(2):91.

[65] Mazzucchelli, C., Bischetti, M., D'Odorico, V., Feruglio, C., Schindler, J. T., Onoue, M., Bañados, E., Becker, G. D., Bian, F., Carniani, S., Decarli, R., Eilers, A. C., Farina, E. P., Gallerani, S., Lai, S., Meyer, R. A., Rojas-Ruiz, S., Satyavolu, S., Venemans, B. P., Wang, F., Yang, J., and Zhu, Y. (2023). XQR-30: Black hole masses and accretion rates of 42 z $\gtrsim$ 6 quasars. *A&A*, 676:A71.

[66] Mie, G. (1908). Beiträge zur Optik trüber Medien, speziell kolloidaler Metallösungen. *Annalen der Physik*, 330(3):377–445.

[67] Narayan, R. and Yi, I. (1994). Advection-dominated Accretion: A Self-similar Solution. *ApJL*, 428:L13.

[68] Neeleman, M., Novak, M., Venemans, B. P., Walter, F., Decarli, R., Kaasinen, M., Schindler, J.-T., Bañados, E., Carilli, C. L., Drake, A. B., Fan, X., and Rix, H.-W. (2021). The Kinematics of z $\gtrsim$ 6 Quasar Host Galaxies. *ApJ*, 911(2):141.

[69] Pensabene, A., Carniani, S., Perna, M., Cresci, G., Decarli, R., Maiolino, R., and Marconi, A. (2020). The ALMA view of the high-redshift relation between supermassive black holes and their host galaxies. *A&A*, 637:A84.

[70] Pensabene, A., Decarli, R., Bañados, E., Venemans, B., Walter, F., Bertoldi, F., Fan, X., Farina, E. P., Li, J., Mazzucchelli, C., Novak, M., Riechers, D., Rix, H. W., Strauss, M. A., Wang, R., Weiß, A., Yang, J., and Yang, Y. (2021). ALMA multiline survey of the ISM in two quasar host-companion galaxy pairs at z $>$ 6. *A&A*, 652:A66.

[71] Planck Collaboration (2020). Planck 2018 results. VI. Cosmological parameters. *A&A*, 641:A6.

[72] Read, J. I. and Trentham, N. (2005). The baryonic mass function of galaxies. *Philosophical Transactions of the Royal Society of London Series A*, 363(1837):2693.

[73] Reines, A. E. and Volonteri, M. (2015). Relations between Central Black Hole Mass and Total Galaxy Stellar Mass in the Local Universe. *ApJ*, 813(2):82.

[74] Rémy-Ruyer, A., Madden, S. C., Galliano, F., Galametz, M., Takeuchi, T. T., Asano, R. S., Zhukovska, S., Lebouteiller, V., Cormier, D., Jones, A., Bocchio, M., Baes, M., Bendo, G. J., Boquien, M., Boselli, A., DeLooze, I., Doublier-Pritchard, V., Hughes, T., Karczewski, O. Ł., and Spinoglio, L. (2014). Gas-to-dust mass ratios in local galaxies over a 2 dex metallicity range. *A&A*, 563:A31.

[75] Rivera, G. C., Hodge, J. A., Smail, I., Swinbank, A. M., Weiss, A., Wardlow, J. L., Walter, F., Rybak, M., Chen, C.-C., Brandt, W. N., Coppin, K., Cunha, E. d., Dannerbauer, H., Greve, T. R., Karim, A., Knudsen, K. K., Schinnerer, E., Simpson, J. M., Venemans, B., and Van Der Werf, P. P. (2018). Resolving the ism at the peak of cosmic star formation with alma: The distribution of co and dust continuum in z$\sim$2.5 submillimeter galaxies. *ApJ*, 863(1):56.

[76] Rowlands, K., Gomez, H. L., Dunne, L., Aragón-Salamanca, A., Dye, S., Maddox, S., da Cunha, E., and Werf, P. v. d. (2014). The dust budget crisis in high-redshift submillimetre galaxies. *MNRAS*, 441(2):1040–1058.

[77] Runnoe, J. C., Brotherton, M. S., and Shang, Z. (2012). Updating quasar bolometric luminosity corrections. *MNRAS*, 422(1):478–493.

[78] Santini, P., Maiolino, R., Magnelli, B., Lutz, D., Lamastra, A., Li Causi, G., Eales, S., Andreani, P., Berta, S., Buat, V., Cooray, A., Cresci, G., Daddi, E., Farrah, D., Fontana, A., Franceschini, A., Genzel, R., Granato, G., Grazian, A., Le Floc'h, E., Magdis, G., Magliocchetti, M., Mannucci, F., Menci, N., Nordon, R., Oliver, S., Popesso, P., Pozzi, F., Riguccini, L., Rodighiero, G., Rosario, D. J., Salvato, M., Scott, D., Silva, L., Tacconi, L., Viero, M., Wang, L., Wuyts, S., and Xu, K. (2014). The evolution of the dust and gas content in galaxies. *A&A*, 562:A30.

[79] Schmidt, M. (1963). 3C 273 : A Star-Like Object with Large Red-Shift. *Nature*, 197(4872):1040.

[80] Schmidt, M. and Green, R. F. (1983). Quasar evolution derived from the Palomar bright quasar survey and other complete quasar surveys. *ApJ*, 269:352–374.

[81] Schreiber, C., Elbaz, D., Pannella, M., Ciesla, L., Wang, T., and Franco, M. (2018). Dust temperature and mid-to-total infrared color distributions for star-forming galaxies at $0 < z < 4$. *A&A*, 609:A30.

[82] Shakura, N. I. and Sunyaev, R. A. (1973). Black holes in binary systems. Observational appearance. *A&A*, 24:337–355.

[83] Shao, L., Lutz, D., Nordon, R., Maiolino, R., Alexander, D. M., Altieri, B., Andreani, P., Aussel, H., Bauer, F. E., Berta, S., Bongiovanni, A., Brandt, W. N., Brusa, M., Cava, A., Cepa, J., Cimatti, A., Daddi, E., Dominguez-Sanchez, H., Elbaz, D., Förster Schreiber, N. M., Geis, N., Genzel, R., Grazian, A., Gruppioni, C., Magdis, G., Magnelli, B., Mainieri, V., Pérez García, A. M., Poglitsch, A., Popesso, P., Pozzi, F., Riguccini, L., Rodighiero, G., Rovilos, E., Saintonge, A., Salvato, M., Sanchez Portal, M., Santini, P., Sturm, E., Tacconi, L. J., Valtchanov, I., Wetzstein, M., and Wieprecht, E. (2010). Star formation in AGN hosts in GOODS-N. *A&A*, 518:L26.

[84] Shen, X., Vogelsberger, M., Nelson, D., Tacchella, S., Hernquist, L., Springel, V., Marinacci, F., and Torrey, P. (2022). High-redshift predictions from IllustrisTNG - III. Infrared luminosity functions, obscured star formation, and dust temperature of high-redshift galaxies. *MNRAS*, 510(4):5560–5578.

[85] Shen, Y., Greene, J. E., Strauss, M. A., Richards, G. T., and Schneider, D. P. (2008). Biases in Virial Black Hole Masses: An SDSS Perspective. *ApJ*, 680(1):169–190.

[86] Shen, Y., Richards, G. T., Strauss, M. A., Hall, P. B., Schneider, D. P., Snedden, S., Bizyaev, D., Brewington, H., Malanushenko, V., Malanushenko, E., Oravetz, D., Pan, K., and Simmons, A. (2011). A Catalog of Quasar Properties from Sloan Digital Sky Survey Data Release 7. *ApJS*, 194(2):45.

[87] Sommovigo, L., Ferrara, A., Carniani, S., Pallottini, A., Dayal, P., Pizzati, E., Ginolfi, M., Markov, V., and Faisst, A. (2022a). A new look at the infrared properties of z 5 galaxies. *MNRAS*, 517(4):5930–5941.

[88] Sommovigo, L., Ferrara, A., Pallottini, A., Dayal, P., Bouwens, R. J., Smit, R., da Cunha, E., De Looze, I., Bowler, R. A. A., Hodge, J., Inami, H., Oesch, P., Endsley, R., Gonzalez, V., Schouws, S., Stark, D., Stefanon, M., Aravena, M., Graziani, L., Riechers, D., Schneider, R., van der Werf, P., Algera, H., Barrufet, L., Fudamoto, Y., Hygate, A. P. S., Labbé, I., Li, Y., Nanayakkara, T., and Topping, M. (2022b). The ALMA REBELS Survey: cosmic dust temperature evolution out to z 7. *MNRAS*, 513(3):3122–3135.

[89] Springel, V., Di Matteo, T., and Hernquist, L. (2005). Modelling feedback from stars and black holes in galaxy mergers. *MNRAS*, 361(3):776–794.

[90] Team, A. P. (2021). *ALMA Science Pipeline User's Guide*. ALMA Doc 2021.2v1.0.

[91] Thomas, D., Maraston, C., Schawinski, K., Sarzi, M., and Silk, J. (2010). Environment and self-regulation in galaxy formation. *MNRAS*, 404(4):1775–1789.

[92] Thomas, M. O., Shemmer, O., Trakhtenbrot, B., Lira, P., Netzer, H., Simmons, B. D., and Ilan, N. (2023). Searching for the Role of Mergers in Fast and Early SMBH Growth: Morphological Decomposition of Quasars and Their Hosts at z $\sim$ 4.8. *ApJ*, 955(1):15.

[93] Tripodi, R., Feruglio, C., Fiore, F., Zappacosta, L., Piconcelli, E., Bischetti, M., Bongiorno, A., Carniani, S., Civano, F., Chen, C. C., Cristiani, S., Cupani, G., Di Mascia, F., D'Odorico, V., Fan, X., Ferrara, A., Gallerani, S., Ginolfi, M., Maiolino, R., Mainieri, V., Marconi, A., Saccheo, I., Salvestrini, F., Tortosa, A., and Valiante, R. (2024). HYPERION. Coevolution of supermassive black holes and galaxies at $z > 6$ and the build-up of massive galaxies. *arXiv e-prints*, page arXiv:2401.04211.

[94] Tsukui, T., Wisnioski, E., Krumholz, M. R., and Battisti, A. (2023). Spatially resolved dust properties and quasar-galaxy decomposition of a hyper-luminous infrared galaxy at z $\sim$ 4.4. *MNRAS*, 523(3):4654–4679.

[95] Venemans, B. P., Walter, F., Decarli, R., Ferkinhoff, C., Weiß, A., Findlay, J. R., McMahon, R. G., Sutherland, W. J., and Meijerink, R. (2017). Molecular Gas in Three z $\sim$ 7 Quasar Host Galaxies. *ApJ*, 845(2):154.

[96] Venemans, B. P., Walter, F., Neeleman, M., Novak, M., Otter, J., Decarli, R., Bañados, E., Drake, A., Farina, E. P., Kaasinen, M., Mazzucchelli, C., Carilli, C., Fan, X., Rix, H.-W., and Wang, R. (2020). Kiloparsec-scale ALMA Imaging of [C II] and Dust Continuum Emission of 27 Quasar Host Galaxies at z $\sim$ 6. *ApJ*, 904(2):130.

[97] Venemans, B. P., Walter, F., Zschaechner, L., Decarli, R., De Rosa, G., Findlay, J. R., McMahon, R. G., and Sutherland, W. J. (2016). Bright [C II] and Dust Emission in Three z $>$ 6.6 Quasar Host Galaxies Observed by ALMA. *ApJ*, 816(1):37.

[98] Walter, F., Neeleman, M., Decarli, R., Venemans, B., Meyer, R., Weiss, A., Bañados, E., Bosman, S. E. I., Carilli, C., Fan, X., Riechers, D., Rix, H., and Thompson, T. A. (2022). Alma 200 pc imaging of a z $\sim$ 7 quasar reveals a compact, disk-like host galaxy. *ApJ*, 927(1):21.

[99] Wang, F., Yang, J., Fan, X., Hennawi, J. F., Barth, A. J., Banados, E., Bian, F., Boutsia, K., Connor, T., Davies, F. B., Decarli, R., Eilers, A.-C., Farina, E. P., Green, R., Jiang, L., Li, J.-T., Mazzucchelli, C., Nanni, R., Schindler, J.-T., Venemans, B., Walter, F., Wu, X.-B., and Yue, M. (2021). A Luminous Quasar at Redshift 7.642. *ApJL*, 907(1):L1.

[100] Wang, R., Wagg, J., Carilli, C. L., Walter, F., Lentati, L., Fan, X., Riechers, D. A., Bertoldi, F., Narayanan, D., Strauss, M. A., Cox, P., Omont, A., Menten, K. M., Knudsen, K. K., Neri, R., and Jiang, L. (2013). Star Formation and Gas Kinematics of Quasar Host Galaxies at z ~6: New Insights from ALMA. *ApJ*, 773(1):44.

[101] Warmels R., Biggs A., Cortes P. A., Dent B., Di Francesco J., Fomalont E., Hales A., Kameno S., Mason B., Philips N., Remijan A., Saini K., Stoehr F., Vila Vilaro B., Villard E. (2018). *ALMA Technical Handbook*. ALMA Doc. 6.3, ver. 1.0.

[102] Witstok, J., Jones, G. C., Maiolino, R., Smit, R., and Schneider, R. (2023). An empirical study of dust properties at the earliest epochs. *MNRAS*, 523(2):3119–3132.

[103] Wu, P.-F. (2024). AGN-driven outflow shuts down star formation in a $z = 4$ recently quenched galaxy. *arXiv e-prints*, page arXiv:2409.00471.

[104] Yang, J., Venemans, B., Wang, F., Fan, X., Novak, M., Decarli, R., Walter, F., Yue, M., Momjian, E., Keeton, C. R., Wang, R., Zabludoff, A., Wu, X.-B., and Bian, F. (2019). Far-infrared Properties of the Bright, Gravitationally Lensed Quasar J0439+1634 at z = 6.5. *ApJ*, 880(2):153.

[105] Yue, M., Yang, J., Fan, X., Wang, F., Spilker, J., Georgiev, I. Y., Keeton, C. R., Litke, K. C., Marrone, D. P., Walter, F., Wang, R., Wu, X.-B., Venemans, B. P., and Zabludoff, A. (2021). ALMA Observations of the Sub-kpc Structure of the Host Galaxy of a z = 6.5 Lensed Quasar: A Rotationally Supported Hyper-Starburst System at the Epoch of Reionization. *ApJ*, 917(2):99.